FEASIBILITY STUDY OF

PIEZOTRANSISTOR ACCELEROMETERS

Prepared for

Headquarters
National Aeronautics and Space Administration
Washington, D. C.

Annual Report

September 1965

(Prepared under Contract NASr-222 by the Solid State Laboratory
of the Research Triangle Institute, Durham, North Carolina)

RESEARCH TRIANGLE INSTITUTE · DURHAM, NORTH CAROLINA

FOREWORD


This report was prepared by the Research Triangle Institute, Durham, North Carolina, on NASA Contract NASr-222, "Feasibility Study of Piezotransistor Accelerometer". This work was administered under the directions of the Instrument Research Division at Langley Research Center by Mr. John Olivero and of the Office of Advanced Research and Technology Division at NASA Headquarters by Dr. Wolfgang Menzel.

This study began in June 1964 and was concluded in September 1965. It was performed by the Solid State Laboratory of the Research Triangle Institute under the general direction of Dr. R. M. Burger. While Dr. J. J. Wortman was the project engineer, the entire technical staff has participated to some degree in this effort. Specific credits are due Dr. J. R. Hauser, R. R. Stockard, H. L. Honbarrier and A. D. Brooks for their invaluable contribution in this investigation.

Part of the results of this work has been submitted to Duke University as a Ph.D. dissertation by J. J. Wortman under the title "Effect of Mechanical Strain on P-N Junctions" and published by NASA as a contractor Report NASA CR-275.

# CONTENTS

CONTENTS (Con'd.)

LIST OF FIGURES

LIST OF FIGURES (Con'd.)

LIST OF FIGURES (Con'd.)

LIST OF FIGURES (Con'd.)

# LIST OF FIGURES (Con'd.)

LIST OF TABLES

## LIST OF SYMBOLS

| | |
|---|---|
| a | lattice spacing (cm) |
| $\alpha$ | dimensionless band parameter |
| $\alpha$ | grounded base current gain |
| $A_b$ | total area minus stressed area on base side of e-b junction $(cm^2)$ |
| $A_e$ | total area minus stressed area on emitter side of e-b junction $(cm^2)$ |
| $A_{sn}$ | stressed areas at the edge of the depletion region on the n side of the junction $(cm^2)$ |
| $A_{sp}$ | stressed area at the edge of the depletion region on the p side of the junction $(cm^2)$ |
| $A_T$ | total junction area $(cm^2)$ |
| $B_b$ | stressed area on base side divided by total e-b junction area |
| $B_e$ | stressed area on emitter side divided by total e-b junction area |
| $c_{ij}, s_{ij}$ | stiffness, compliance coefficient $(cm^2/dyne)$, $(dyne/cm^2)$ |
| c.p. | cyclic permutation |
| $\delta$ | energy separation of the "heavy" and "light" hole bands from the split-off band |
| $\delta_{ij}$ | Kronecker delta |
| $\Delta_1$ | energy band in k-space |
| $\Delta_2'$ | energy band in k-space |
| $\Delta E$ | constant (0.5 ev) |
| $\Delta E_g$ | change in the energy gap (ev) |
| $D_p, D_n$ | hole, electron diffusion coefficient $(cm^2/sec)$ |

(x)

| | |
|---|---|
| $D_u$ | deformation potential coefficient (ev) |
| $D_d$ | deformation potential coefficient (ev) |
| $D'_u$ | deformation potential coefficient (ev) |
| $E$ | energy (ev) |
| $E_{ci}$ | energy of conduction band edge (ev) |
| $E_F$ | energy of the Fermi level (ev) |
| $E_g$ | energy gap (ev) |
| $E_i$ | intrinsic Fermi level (ev) |
| $E(\bar{k})$ | energy as a function of $\bar{k}$ (ev) |
| $E_o$ | energy under zero strain conditions (ev) |
| $E_t$ | energy of trap (ev) |
| $E_{V1}$ | energy of the heavy hole band (ev) |
| $E_{V2}$ | energy of the light hole band (ev) |
| $E_{V3}$ | energy of the split-off hole band (ev) |
| $e$ | hydrostatic strain |
| $e_b$ | strain on base side of e-b junction |
| $e_e$ | strain on emitter side of e-b junction |
| $e_n, e_p$ | position dependent strains at the edge of the depletion region on the n and p sides of the junction |
| $e_s$ | strain components referred to the crystal axes |
| $\Gamma'_{25}(j{=}3/2)$ | valence band edge point; "heavy" and "light" holes |
| $\Gamma'_{25}(j{=}1/2)$ | valence band edge point; split-off band |
| $\gamma_v(e)$ | ratio of minority carrier density with strain to that without strain |
| $\hbar$ | Planck's constant ($[6.624/2\pi] \times 10^{-27}$ erg·sec) |

| | |
|---|---|
| $H$ | Hamiltonian (ev) |
| $H_o$ | Hamiltonian under zero strain (ev) |
| $I$ | total current (amp) |
| $I_b$ | base current (amp) |
| $I_{bs}$ | base current in the stressed region (amp) |
| $I_c$ | collector current (amp) |
| $I_n$ | electron current (amp) |
| $I_{no}$ | electron current under zero strain (amp) |
| $I_p$ | hole current (amp) |
| $I_{po}$ | hole current under zero strain (amp) |
| $I_{ne}$ | electron component of emitter current (amp) |
| $I_{pe}$ | hole component of emitter current (amp) |
| $I_s$ | reverse saturation current (amp) |
| $I_U(e)$ | generation-recombination current (amp) |
| $I_U(o)$ | generation-recombination current with zero applied strain (amps) |
| $J_I$ | "ideal" current density (amp/cm$^2$) |
| $J_U$ | generation-recombination current density (amp/cm$^2$) |
| $J_U(o)$ | generation-recombination current density (amp/cm$^2$) |
| $J_x, J_y, J_z, J$ | angular momentum matrices |
| $k$ | Boltzmann's constant ($8.62 \times 10^{-5}$ ev/°K) |
| $\bar{k}$ | wave vector (cm$^{-1}$) |
| $\kappa_x$ | distance of band edge point in k-space as measured from $X_1$ point, $\kappa_x = -[2\pi a^{-1} - \kappa_x]$, (cm$^{-1}$) |

## LIST OF SYMBOLS (Con'd.)

| | |
|---|---|
| R | spreading resistance (ohm) |
| $\rho$ | resistivity (ohm-cm) |
| $\sigma$ | stress (dyne/cm$^2$) |
| $\sigma$ | conductivity (ohm$^{-1}\cdot$cm$^{-1}$) |
| T | absolute temperature (°K) |
| $\theta$ | constant depending on the device (dimensionless) |
| $\tau$ | lifetime (sec) |
| $\tau_{no}$ | lifetime of electrons injected into highly p-type material (sec) |
| $\tau_{po}$ | lifetime of holes injected into highly n-type material (sec) |
| U | steady state recombination rate (sec$^{-1}$) |
| V | band parameter |
| $\nu$ | number of conduction minima |
| $V_a$ | applied voltage (volt) |
| $V_{cb}$ | collector-base voltage (volt) |
| $V_{eb}$ | emitter-base voltage (volt) |
| $V_o$ | built-in junction potential (volt) |
| W | width of space charge region (cm) |
| $W_n, W_p, W_d$ | widths of the n, p and depletion region (cm) |
| $[\ ]_d$ | deformation potential coefficient (ev) |
| $[\ ]_s$ | deformation potential coefficient (ev) |
| $[\ ]_u$ | deformation potential coefficient (ev) |
| $[\ ]_u'$ | deformation potential coefficient (ev) |

| | |
|---|---|
| $K_1, K_2, K_3$ | constants |
| $\ell, m, n$ | direction cosines |
| $L_p, L_n$ | hole, electron diffusion length (cm) |
| $m_c$ | effective mass (gm) |
| $m_{ij}^*$ | components of effective mass tensor (gm) |
| $m_\parallel$ | electron effective mass in parallel direction (gm) |
| $m_\perp$ | electron effective mass in transverse direction (gm) |
| $m_o$ | electron rest mass ($9.109 \times 10^{-28}$ gm) |
| $\mu_n$ | electron mobility ($cm^2$/volt·sec) |
| $\mu_p$ | hole mobility ($cm^2$/volt·sec) |
| $m_{V1}$ | effective mass of heavy holes (gm) |
| $m_{V2}$ | effective mass of light holes (gm) |
| $m_{V3}$ | effective mass of split-off band holes (gm) |
| $m_V^*$ | density of states effective mass of holes (gm) |
| $n$ | electron density or concentration ($cm^{-3}$) |
| $n_i$ | intrinsic carrier density ($cm^{-3}$) |
| $n_{io}$ | zero strain intrinsic carrier density ($cm^{-3}$) |
| $n_p$ | density of electrons in p-type material ($cm^{-3}$) |
| $n_{po}$ | zero strain density of electrons in p-type material ($cm^{-3}$) |
| $N$ | band parameter |
| $p$ | hole density or concentration ($cm^{-3}$) |
| $p_1, n_1$ | hole, electron density ($cm^{-3}$) |
| $p_n$ | density of holes in n-type material ($cm^{-3}$) |
| $p_{no}$ | zero strain density of holes in n-type material ($cm^{-3}$) |
| $q$ | electronic charge on an electron ($1.602 \times 10^{-19}$ coul) |

Chapter I

INTRODUCTION AND SUMMARY

The object of this research has been to determine the feasibility of
utilizing p-n junction devices as a transducer for accelerometers.  This study
has consisted of a theoretical study of the effects of mechanical strain on
semiconductor (Ge and Si) parameters and in particular those parameters associ-
ated with p-n junctions.  An experimental investigation has been performed in
which silicon diodes, transistors, and 4-region devices have been tested by
observing their electrical characteristics under mechanical stress.  Laboratory
accelerometers utilizing diodes as the transducer have been fabricated and
tested.

It has been known for sometime that large mechanical stresses
($\sim 10^8 - 10^{11}$ dynes/cm$^2$) have significant effects upon the electrical charac-
teristics of p-n junctions.  Early work treated the effect of hydrostatic
pressure opon diodes [1].  Recent experimental investigations [2,3,4,5,6,7,8,
9,10] have shown that anisotropic stress has a larger effect upon p-n junction
characteristics than does hydrostatic stress.  A theoretical model for the
phenomenon has been developed which is based on the distortion of the energy
band structure of the semiconductor under a general stress condition.  Analyti-
cal expressions have been developed which describe the characteristics by
p-n junction devices under stress.  The theory has been found to be in good
qualitative agreement with experimental results.

A series of experiments have been designed and performed on a variety
of semiconductor devices the aim of which has been to delineate the under-
lying physical mechanisms responsible for the phenomenon.  Both mesa and
planar diodes have been studied to determine the effects of mechanical strain
on the electrical characteristics of single p-n junctions.  Mesa diodes have
been used as a test structure to determine the effects of crystal orientation
and junction depth on the phenomenon.  The major effect of stress on single
junction devices is to lower the electrical resistance.  Tests have also
been made to determine the effects of temperature and long term static loading
on the phenomenon.

Both commercial and laboratory transistors and 3-junction devices
(4-layer diodes) have been studied experimentally.  The major effect of stress
on transistors is to lower the gain of the device.  The amount of stress
induced change in transistor parameters has been found to depend on the mode
of operation and location of the stress field.  Experiment has shown that the
major effect of stress on the electrical characteristics of 4-layer diodes is
to lower the breakdown voltage.  Four-layer diodes have been incorporated
in an oscillator circuit and stress applied to the diode with the result that
the oscillator frequency increases with increasing stress.

The experimental study has shown that practically any semiconductor
junction device is a potential transducer of mechanical stress.  As a result
of these experiments a much better understanding of the piezojunction pheno-
menon has been gained and in addition, a great deal of technology has been
developed concerning p-n junction transducers in general.

A new method for applying high stress levels to semiconductor junctions
has been developed for use in transducer applications--a silicon needle with
a p-n junction or junctions on the apex of the needle.  Laboratory accelerometers

have been fabricated and tested using the silicon needle approach to p-n junction transducers. These tests have shown that it is feasible to use the piezojunction effect in semiconductors as the transducer in accelerometers. Accelerometers using this effect can offer such advantages as ac and dc response, reduced weight and power, direct frequency modulated output, and high frequency response. The major disadvantage is temperature sensitivity.

It can be concluded from this work that p-n junction devices can be used in a variety of transducer applications. Any physical phenomenon which results in mechanical force and displacement can theoretically be detected by p-n junction devices if the force is on the order of $10^3$ dynes or larger. Several potential applications other than accelerometer transducers are pressure, force, stress and strain, and displacement.

Chapter II

ENERGY BAND STRUCTURE AND DEFORMATION POTENTIAL
THEORY OF Ge AND Si

2.1  Energy Band Structure

Germanium and silicon form single crystals with the diamond cubic

structure.  The periodicity and the binding energy of the atoms in the

crystal lattice impose certain quantum mechanical restrictions on the

energy that electrons in the crystal can have [11].  As is the case for

all semiconductors, germanium and silicon each have a forbidden energy

range (energy gap) separating the valence levels and the conduction levels.

It is this energy gap that gives semiconductors the desirable electrical

properties which they possess.  As will be discussed later, a mechanical

deformation of the crystal lattice changes the forbidden gap and thereby

changes the electrical properties of the semiconductor.

It is convenient, from quantum mechanical considerations, to describe

the energy bands in terms of momentum space (k-space).  The energy bands of

germanium and silicon are functions of position in k-space.  The maximum

valence levels and the minimum conduction levels are of interest here

since it is these levels that determine the energy gap.  The following is

a discussion of the unstrained energy structure of Ge and Si.  The maximum

valence levels occur at k = (000) and the minimum conduction levels occur

in the <111> and <100> directions for germanium and silicon respectively.

(4)

Figures 1 and 2 are sketches of the band structure of germanium and silicon as a function of $\bar{k}$ for the $\langle 111 \rangle$ and $\langle 100 \rangle$ directions [12]. The notation used to indicate energy surfaces and k-space points are those adapted from group theory [13].

Germanium has eight conduction minima which lie in the $\langle 111 \rangle$ directions and are located at the $L_1$ point, $k = \Pi a^{-1}(111)$, where a is the lattice spacing. Silicon has six conduction minima which occur in the $\langle 100 \rangle$ directions and are located at $k \approx 1.7\Pi a^{-1}(100)$ which is approximately 85% of the distance from $k = (000)$ to $k = 2\Pi a^{-1}(100)$ or the $X_1$ point. The conduction electrons are located at these conduction minima. The name "many valley" semiconductor is sometimes given to germanium and silicon and is derived from the fact that they have conduction minima in more than one k-space direction. Using this model, n-type Ge is a $\langle 111 \rangle$ valley material and n-type silicon is a $\langle 100 \rangle$ valley material.

The maximum valence levels, $\Gamma'_{25}$, for both germanium and silicon are located at $k = (000)$ and are assigned an energy value of zero for convenience. The $\Gamma'_{25}$ level is degenerate in energy. Figure 3 shows an expanded view of the levels in Si [14]. As can be seen, there is a slight separation in energy of these bands at $k = (000)$ which results from the two angular momentum quantum numbers $j = 3/2$ and $j = 1/2$. The $\Gamma'_{25}(j = 3/2)$ level is itself degenerate at $k = (000)$ and is slightly split for $k \neq (000)$ due to spin orbit coupling. Electron spin resonance experiments have shown that for the $\Gamma'_{25}(j = 3/2)$ level the upper of the bands is slightly different in shape from that of the lower band and as a result the effective masses are different for the two. The upper band gives rise to the so-called "heavy" holes and the lower band the "light" holes. In non-degenerate material the $\Gamma'_{25}(j = 1/2)$ level is usually neglected when performing hole population
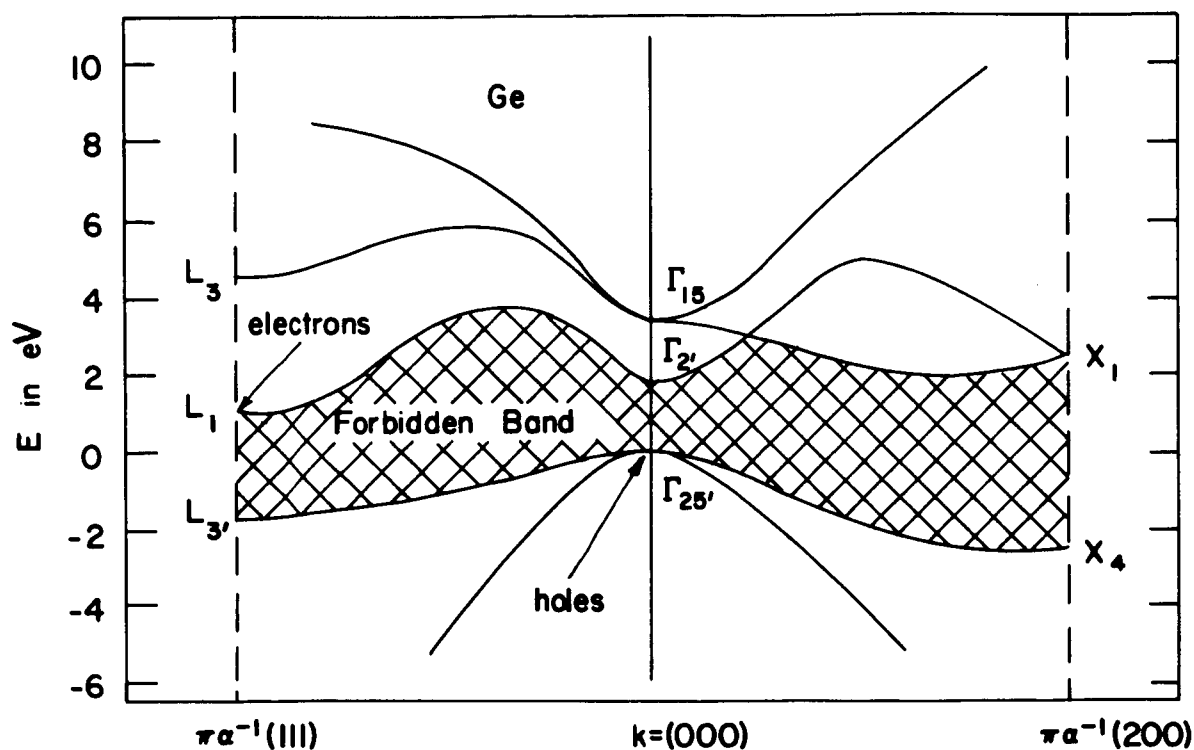
Fig. 1. Energy Band Structure of Germanium for the <111> and <100> Directions in k-space.
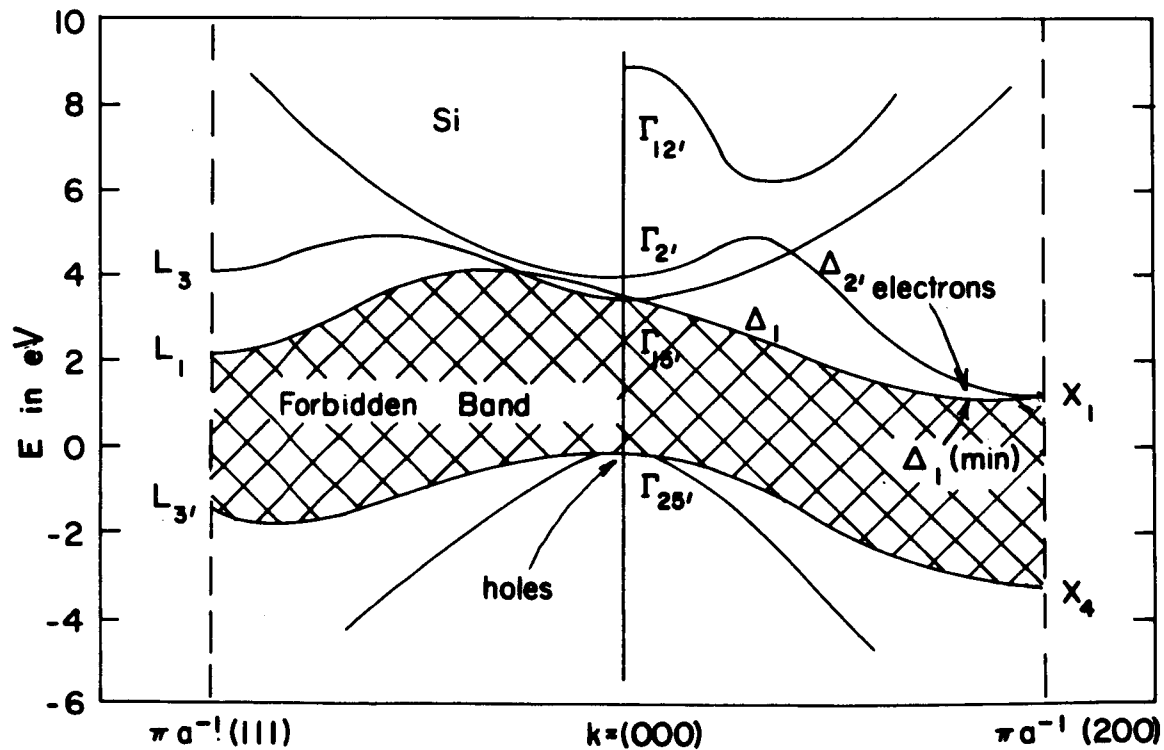


Fig. 2. Energy Band Structure of Silicon for the <111> and <100> Directions in k-space.

E(k)

j = 3/2

Heavy Hole
Band

Light Holes
Band

δ = 0.044 ev

j = 1/2

Split-off
Band

k
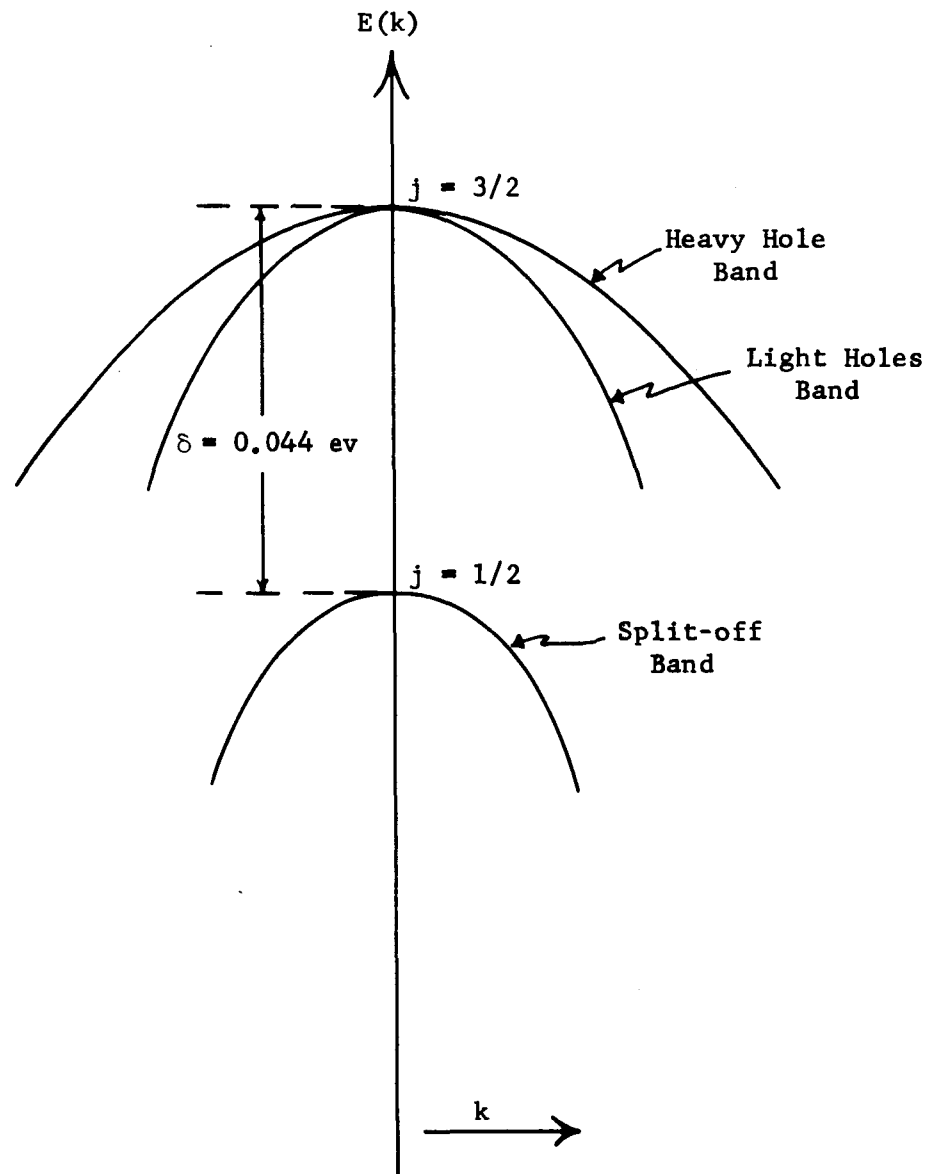
Fig. 3. The Valence Bands of Silicon near k̄ = 0.

calculations since it is separated in energy from the j = 3/2 bands. This

assumption is quite good for germanium while in some cases it may not be a

good assumption for silicon.

The points in k-space where the conduction band minima and valence

band maxima occur are called band edge points. In the case of the conduc-

tion bands for germanium and silicon, if one translates the origin in k-space

to the band edge points, constant energy surfaces are found to be ellipsoids

of revolution about the band edge points. Figure 4 is a sketch of the multi-valley energy surfaces for n-type silicon.
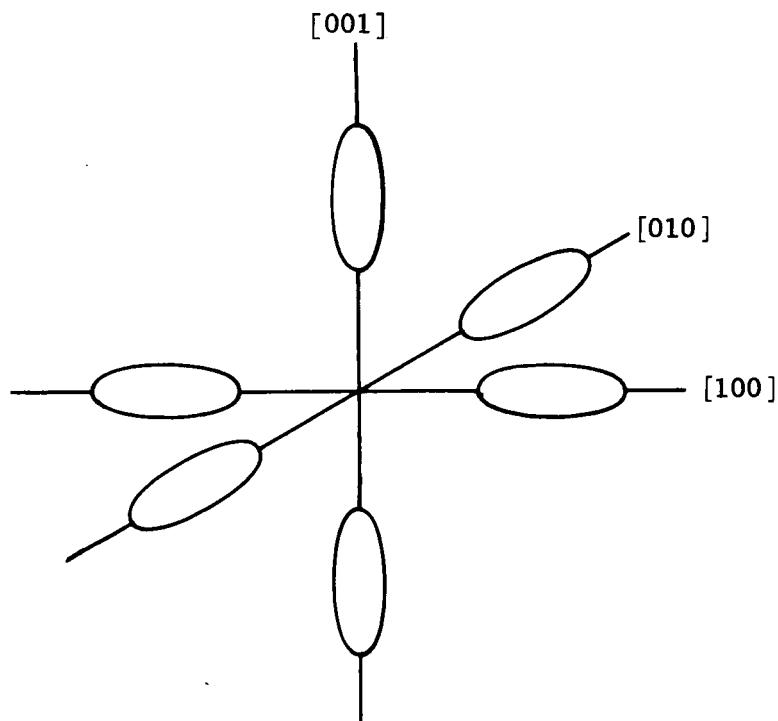


Fig. 4.  Multi-valley Energy Surfaces for the Conduction Band of n-type Silicon.

Constant energy surfaces in the valence band are much more complicated due to the degeneracy. Early workers in the field assumed that the surfaces were spherical. Of late, experiment and theory have shown that the surfaces are warped spheres. Figure 5 is a sketch of the cross-section of energy surfaces a constant distance below the origin for silicon. As shown, the heavy and light hole surfaces are quite different.

[$\bar{1}\bar{1}0$]

Heavy Holes

[$\bar{1}\bar{1}\bar{1}$]

[$\bar{1}\bar{1}1$]

Light Holes

[$00\bar{1}$]

$\bar{k} = 0$

[001]

[$11\bar{1}$]

[111]

[110]
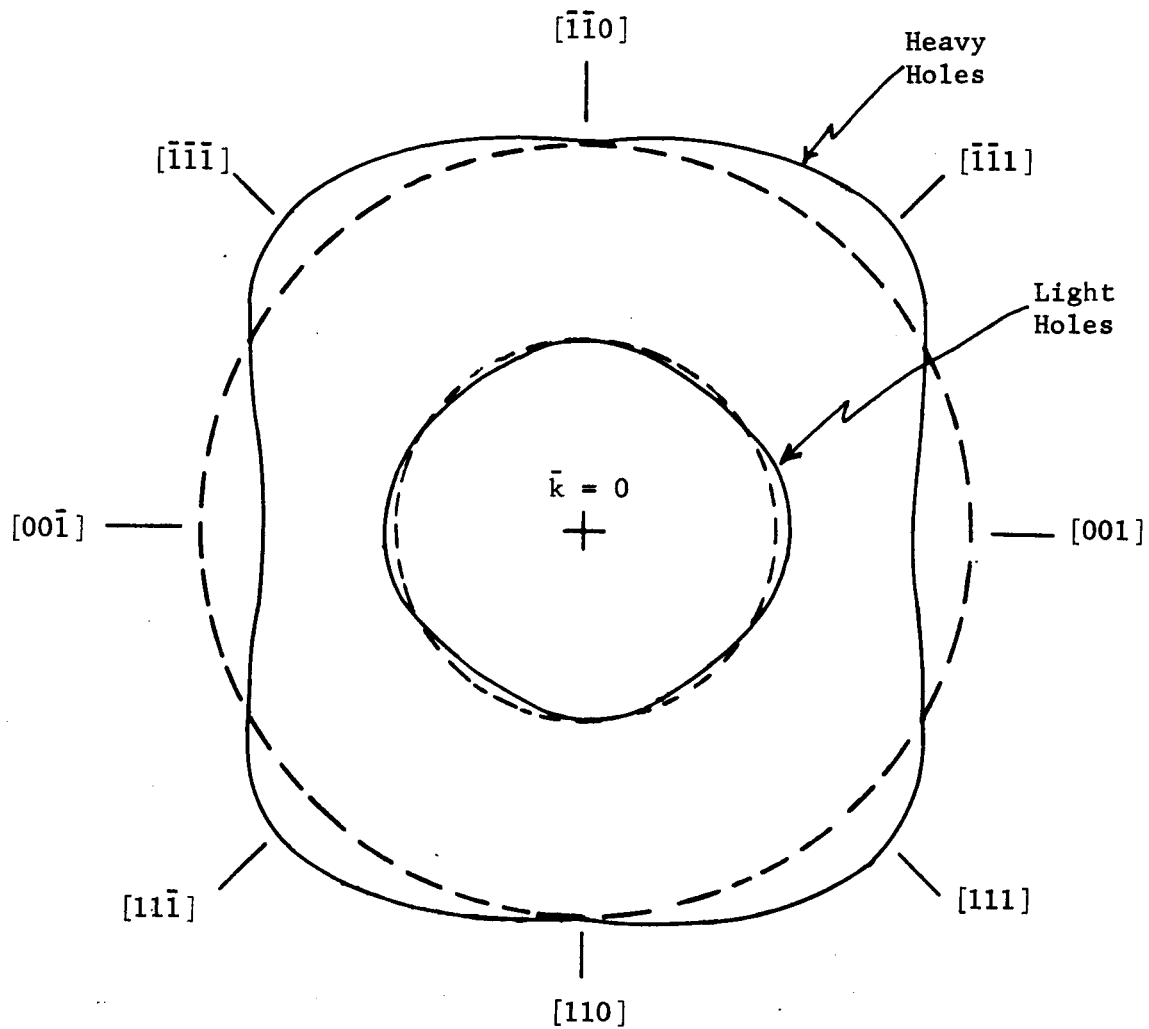
Fig. 5.  Cross-section of the Valence Band Energy Surfaces a Constant
Distance Below the Origin.

## 2.2 Deformation Potential Theory

As one might expect, if the crystal is mechanically deformed the
periodicity of the lattice will be altered and hence the energy bands will
change.  Bardeen and Shockley first introduced deformation potential theory
in 1950 to explain mobility [15].  In 1955, Herring and Vogt [16] expanded
the Bardeen-Shockley theory in formulating their transport theory of

many-valley semiconductors. The deformation potential coefficients, []'s as introduced by Herring and Vogt are defined by

$$E = E_o + \sum_{s=1}^{6} []_s \, e_s \qquad (2.1)$$

where E is the energy at the band edge point, $E_o$ is the unstrained energy, and $e_s$ are the strain components indexed in the usual manner (see Appendix A) and referred to the crystallographic axes. Equation 2.1 has since been found to apply in general only for the conduction band of germanium. The discussion to follow considers in some detail the effect of a general strain on the conduction and valence bands of germanium and silicon.

### 2.2.1 Valence Bands of Ge and Si

Kleiner and Roth [17] have derived the Hamiltonian, H, from symmetry considerations which includes the effect of a homogeneous strain $e_s$ (s = 1,2,...6), on the valence band edge:

$$H = H_o + D_d(e_1 + e_2 + e_3) + \frac{2}{3} D_u [(J_x^2 - \frac{1}{3} J^2) \, e_1 + c.p.]$$

$$+ \frac{2}{3} D_u' [\frac{1}{2}(J_y J_z + J_z J_y) \, e_4 + c.p.] \qquad (2.2)$$

where the D's are the deformation potential coefficients, the J's are the 4 × 4 angular momentum matrices of the hole for j = 3/2, and $H_o$ is the zero strain Hamiltonian; $D_d$ is the shift per unit dilatation of the band edge, while $\frac{4}{3} D_u$ is the splitting of the band edge induced by uniaxial shear strain along the [001] axis, $\frac{4}{3} D_u'$ gives the splitting similarly for the [111] axis. Finally, "c.p." means cyclic permutations of x, y, and z referring to the crystallographic axes.

For a Cartesian coordinate system, the conventional representation for the angular momenta for $j = 3/2$ are [18]

$$J_x = \frac{1}{2}\begin{pmatrix} 0 & \sqrt{3} & 0 & 0 \\ \sqrt{3} & 0 & 2 & 0 \\ 0 & 2 & 0 & \sqrt{3} \\ 0 & 0 & \sqrt{3} & 0 \end{pmatrix}, \quad J_y = \frac{1}{2}\begin{pmatrix} 0 & \sqrt{3}i & 0 & 0 \\ \sqrt{3}i & 0 & -2i & 0 \\ 0 & 2i & 0 & -\sqrt{3}i \\ 0 & 0 & \sqrt{3}i & 0 \end{pmatrix},$$

$$J_z = \frac{1}{2}\begin{pmatrix} 3 & 0 & 0 & 0 \\ 0 & 1 & 0 & 0 \\ 0 & 0 & -1 & 0 \\ 0 & 0 & 0 & -3 \end{pmatrix}, \quad J^2 = \frac{15}{4}\begin{pmatrix} 1 & 0 & 0 & 0 \\ 0 & 1 & 0 & 0 \\ 0 & 0 & 1 & 0 \\ 0 & 0 & 0 & 1 \end{pmatrix}. \qquad (2.3)$$

Substituting Eq. (2.3) into (2.2) gives

$$H - H_o = \begin{pmatrix} R_1 + R_2 & R_5 - iR_4 & R_3 - iR_6 & 0 \\ R_5 + iR_4 & R_1 - R_2 & 0 & R_3 - iR_6 \\ R_3 + iR_6 & 0 & R_1 - R_2 & -R_5 + iR_4 \\ 0 & R_3 - iR_6 & -R_5 - iR_4 & R_1 + R_2 \end{pmatrix}, \quad (2.4)$$

where

$$R_1 = D_d(e_1 + e_2 + e_3);$$
$$R_2 = \frac{2}{3} D_u(e_3 - \frac{1}{2}[e_1 + e_2]);$$
$$R_3 = \frac{2}{3} D_u(\frac{1}{2}\sqrt{3})(e_1 - e_2);$$
$$R_6 = \frac{2}{3} D_u'(\frac{1}{2}\sqrt{3}) e_6;$$
$$R_5 = \frac{2}{3} D_u'(\frac{1}{2}\sqrt{3}) e_5;$$
$$R_4 = \frac{2}{3} D_u'(\frac{1}{2}\sqrt{3}) e_4.$$

The allowed energy levels are found by determining the eigenvalues of the Hamiltonian (diagonalizing the Hamiltonian). Mathematically this is done by subtracting the energy, E, from each of the diagonal elements of the Hamiltonian and equating the determinate of the new matrix to zero, i.e. $H - \delta_{ij} E = 0$. Diagonalizing the Hamiltonian for the energy gives

$$E = E_o + R_1 \pm (R_2^2 + R_3^2 + R_4^2 + R_5^2 + R_6^2)^{1/2}$$

or                                                                                                  (2.5)

$$\Delta E = E - E_o = D_d(e_1 + e_2 + e_3) \pm \{(\tfrac{2}{3} D_u)^2 (e_1^2 + e_2^2 + e_3^2 - e_1 e_2 $$
$$- e_1 e_3 - e_2 e_3) + \tfrac{1}{3}(D_u')^2 (e_4^2 + e_5^2 + e_6^2)\}^{1/2} \quad .$$

From Eq. (2.5) it is seen that there is not only a shift of the level due to $D_d$ but also a splitting of the level, due to $D_u$ and $D_u'$, which removes the degeneracy. The separation in energy is twice the square root term of Eq. (2.5). If the net strains multiplying $D_u$ are compressional strains then the + sign of Eq. (2.5) corresponds to the heavy hole band and the - sign corresponds to the light hole band. If the strain is tensional then the ordering of the bands is reversed. For convenience of notation, let the heavy hole band be $E_{v1}$ and the light hole band be $E_{v2}$. From Eq. (2.5) the changes in these levels for <u>compressional</u> strain are

$$\Delta E_{v1} = D_d e + \{(\tfrac{2}{3} D_u)^2 (e_1^2 + e_2^2 + e_3^2 - e_1 e_2 - e_1 e_3 - e_2 e_3)$$

(2.6a)

$$+ \tfrac{1}{3}(D_u')^2 (e_4^2 + e_5^2 + e_6^2)\}^{1/2}$$

and

$$\Delta E_{v2} = D_d \, e - \{(\tfrac{2}{3} D_u)^2 \, (e_1^2 + e_2^2 + e_3^2 - e_1 e_2 - e_1 e_3 - e_2 e_3)$$

(2.6b)

$$+ \tfrac{1}{3}(D_u')^2 \, (e_4^2 + e_5^2 + e_6^2)\}^{1/2} \ .$$

For the sake of completeness the change in the split-off band $\Gamma_{25}'$ (j = 3/2), $E_{v3}$, is $\Delta E_{v3} = D_d \, e$. Figure 6 is a sketch of the bands for a compressional strain.
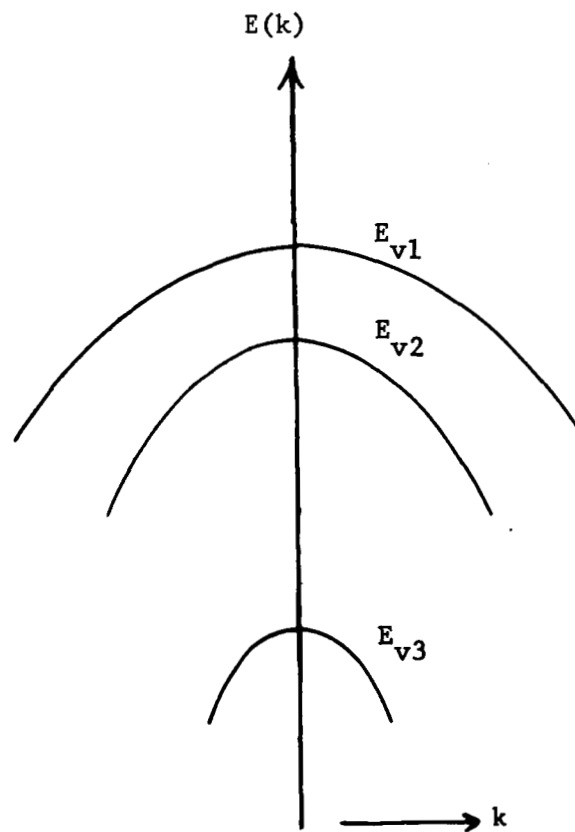


Fig. 6. The Split Valence Bands of Silicon for a Compressional Stress.

## 2.2.2 Conduction Band of Ge

The effect of strain on the conduction band of Ge has already been mentioned in Sect. 2.2. For the band edge point at $k = \pi a^{-1}(111)$ the shift in energy is

$$\Delta E_{c1} = \sum_{s=1}^{6} [\,]_s \, e_s \,, \tag{2.1}$$

where $E_{c1}$ is used to denote the conduction minimum at $k = \pi a^{-1}(111)$. Symmetry restrictions on the deformation potentials reduce the number of constants to two for germanium, $[\,]_u$ and $[\,]_d$ [16]. Equation (2.1) reduces to

$$\Delta E_{c1} = ([\,]_d + \tfrac{1}{3}[\,]_u)\, e + \tfrac{1}{6}[\,]_u(e_4 + e_5 + e_6) \,, \tag{2.7}$$

where $e = e_1 + e_2 + e_3$. The other seven band edge points in the $\langle 111 \rangle$ directions can be obtained by symmetry and will be stated in complete form later.

## 2.2.3 Conduction Band of Si

The effects of strain on the conduction band minima of silicon are considerably more complicated, due mainly to the fact that the minima are not located at highly symmetrical points in k-space. Strain can have the effect of shifting the band edge point in k-space. Hensel and Hasegawa [19,20] have derived the Hamiltonian as a function of the wave vector $\bar{k}$ and strain $e_s$ for the band edge point lying along the [100] axis. The Hamiltonian is given by

$$
H = \begin{bmatrix}
(\hbar V \, \kappa_x + \dfrac{\hbar^2}{2m_\parallel} \kappa_x^2 + \dfrac{1}{2m_\perp}(k_y^2 + k_z^2) & []_u' \, e_4 + N \, k_y \, k_z \\
\quad + []_d \, e + []_u \, e_1) & \\
& \\
[]_u' \, e_4 + N \, k_y \, k_z & (-\hbar V \, \kappa_x + \dfrac{\hbar^2}{2m_\parallel} \kappa_x^2 + \dfrac{1}{2m_\perp}(k_y^2 + k_z^2) \\
& \quad + []_d \, e + []_u \, e_1)
\end{bmatrix} \tag{2.8}
$$

where $m_\parallel$ and $m_\perp$ are the effective masses along the [100] and its transverse directions respectively, V and N are band parameters, $\kappa_x$ is the [100] component of the wave vector $\bar{k}$ as measured from the symmetry point $X_1$ ($\kappa_x = - [2\Pi a^{-1} - k_x]$) and $[]_u'$ is an additional deformation potential coefficient introduced as a result of symmetry analysis.

Diagonalizing the Hamiltonian and setting $k_y = k_z = 0$ (Eq. 2.8) gives

$$
E = \frac{\hbar^2}{2m_\parallel} \kappa_x^2 + []_d \, e + []_u \, e_1 \pm [\hbar^2 \, v^2 \, \kappa_x^2 + ([]_u' \, e_4)^2]^{1/2} \tag{2.9}
$$

In order to get some feel for the significance of this equation, let the strain be zero. Equation (2.9) then reduces to

$$
E = \frac{\hbar^2}{2m_\parallel} \kappa_x^2 \pm \hbar \, V \, \kappa_x \, . \tag{2.10}
$$

This now describes the unstrained energy as a function of $\kappa_x$. Referring to Fig. 2, this describes the energy bands $\Delta_1$ and $\Delta_2'$ where the positive sign of Eq. (2.10) corresponds to the $\Delta_2'$ band and the negative sign corresponds to the $\Delta_1$ band. The band edge point $\kappa_o$ is found by differentiating Eq. (2.10) with respect to $\kappa_x$ and equating the result to zero, i.e. the normal procedure for determining the stationary points of a function. Performing

this operation gives

$$\hbar \, \kappa_0 = - m_\parallel \, |v| \, . \tag{2.11}$$

The band edge point under zero strain conditions is $k_0 = 0.85(2\pi a^{-1})$.
Solving for $\kappa_0$ gives

$$\kappa_0 = - 0.15(2\pi a^{-1}) \, . \tag{2.12}$$

The energy value separating the two levels ($\triangle_1$ and $\triangle_2'$) at the point $\kappa_0$
as determined by the plus and minus sign of Eq. (2.10) is

$$\triangle E = 2m_\parallel \, v^2 \, . \tag{2.13}$$

Returning to Eq. (2.9), the same procedure as that just illustrated
can be used to determine the conduction band minimum and the band edge
point for a general strain. Taking the derivative of Eq. (2.9) with respect
to $\kappa_x$ and equating the result to zero gives

$$\hbar^2 (\kappa_x)^2_{min} = m_\parallel \, v^2 - \frac{([\,]_u' \, e_4)^2}{v^2} \, , \tag{2.14}$$

or

$$\hbar^2 (\kappa_x)^2_{min} = \hbar^2 \, \kappa_0^2 - \frac{([\,]_u' \, e_4)^2}{v^2} \, , \tag{2.15}$$

where $(\kappa_x)_{min}$ is the band edge point under strain. The band edge point,
$(\kappa_x)_{min}$, is a function of the shear deformation potential coefficient $[\,]_u'$
and of the shear strain $e_4$. Hensel, et. al. [19] have given estimated
values of $\triangle E$ as 0.5 ev and $[\,]_u'$ as 5.7 ev. Figure 7 is a plot of $(\kappa_x)_{min}$
as a function of $e_4$ and has been calculated using the above values of
$\triangle E$ and $[\,]_u'$, where $(k_x)_{min} = - [2\pi a^{-1} - (\kappa_x)_{min}]$. Note that $(k_x)_{min}$ increases
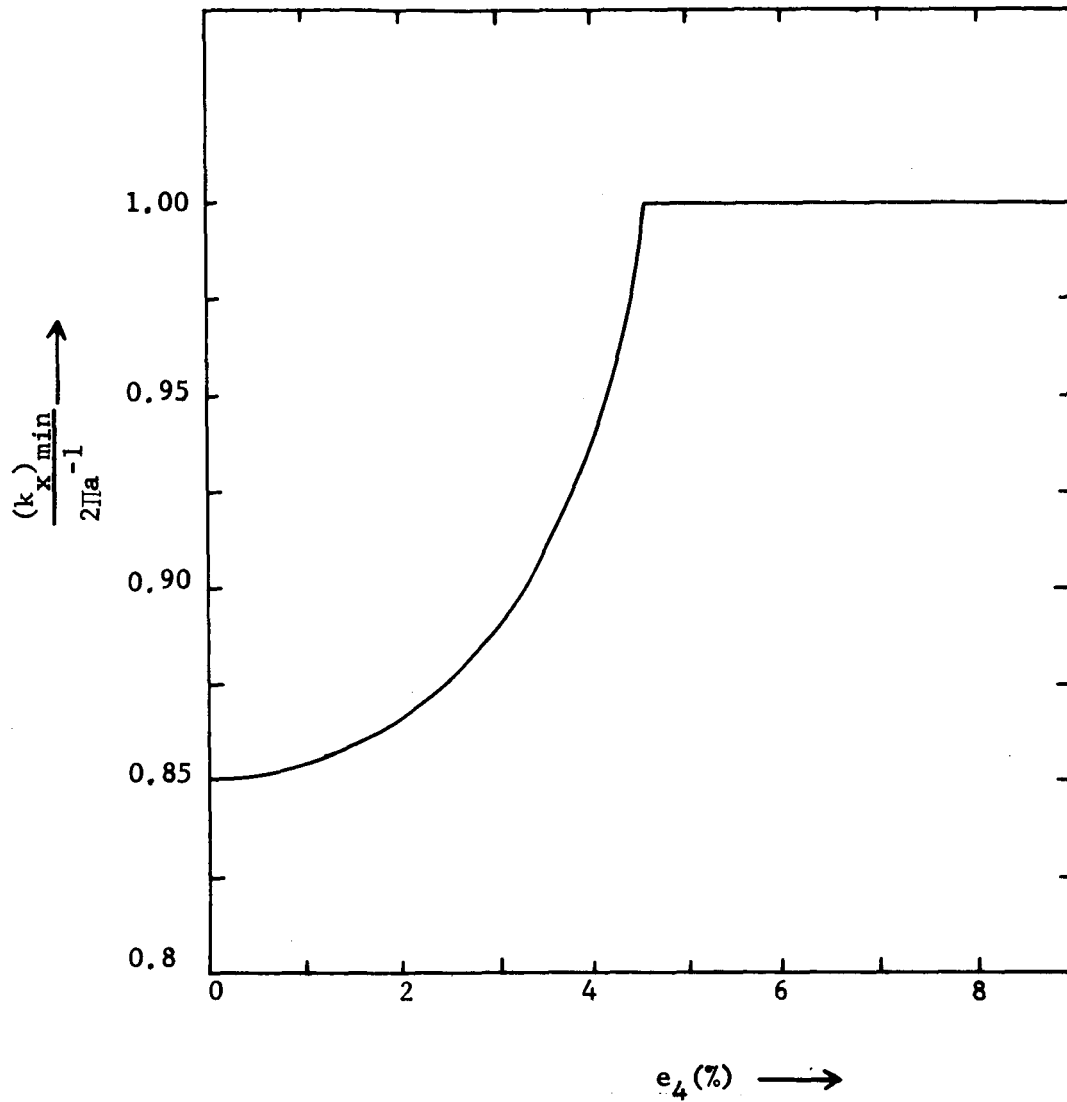
Fig. 7. Variation of the Band Edge Point as Measured from the Origin in the [100]-direction with Respect to the Shear Strain $e_4$.

with shear strain until it reaches the symmetry point $X_1$ where it assumes a value of $2\Pi a^{-1}$ for larger strains. Once $(k_x)_{min}$ reaches $X_1$ it can no longer increase due to symmetry restrictions, i.e. $(\kappa_x)^2_{min}$ must be greater than or equal to zero otherwise $(\kappa_x)_{min}$ would be imaginary. The strain level at which $(\kappa_x)_{min} = 0$ is

$$\left| e_4 \right| = \frac{\Delta E}{2[]_u'} \tag{2.16}$$

where the bars indicate the absolute magnitude.

Substituting Eq. (2.15) into Eq. (2.9) and evaluating at the band edge point gives

$$E = \frac{\Delta E}{4} - \frac{([]_u' e_4)^2}{\Delta E} + []_d e + []_u e_1 \pm \frac{\Delta E}{2} . \tag{2.17}$$

The positive and negative signs of Eq. (2.17) give the energy of the $\Delta_2'$ and $\Delta_1$ bands respectively at the band edge point as a function of strain. In order to reduce the notation, let $E_{ci}$ be the energy of the conduction band minimum where i = 1, 2, 3. Here 1, 2, 3 represent the [100], [010], [001] directions respectively. The [100] valley minimum is then

$$E_{c1} = - \frac{\Delta E}{4} + []_u e_1 + []_d e - \frac{([]_u' e_4)^2}{\Delta E} \tag{2.18}$$

The above equation is good for strains less than that required to shift the band edge point to $X_1$, i.e. $\left| e_4 \right| \leq \Delta E/(2[]_u')$. For strain above the critical value $(\kappa_x)_{min}$ is equal to zero. In this case the energy is obtained directly from Eq. (2.9) and is

$$E_{c1} = []_d e + []_u e_1 - \left| []_u' e_4 \right| . \tag{2.19}$$

The magnitude of the energy is not important here but rather the change in the energy with strain. The change in $E_{c1}$ with strain is as follows:

$$E_{cl} = \begin{cases} []_d \, e + []_u \, e_1 - ([]_u' \, e_4)^2/\Delta E; & |e_4| \leq \Delta E/(2[]_u') \\ \\ []_d \, e + []_u \, e_1 + \frac{\Delta E}{4} - []_u' \, |e_4|; & |e_4| > \Delta E/(2[]_u'). \end{cases} \qquad (2.20)$$

## 2.2.4 Deformation Potential Coefficients

The deformation potential coefficients have been calculated theoretically by Kleinman, et. al [21, 22, 23]. His calculations are for pure (no impurities) Ge and Si and are based upon a knowledge of the electronic wave functions. Many of the coefficients have been calculated from data taken from piezoresistance and cyclotron resonance experiments. Table I lists both experimental and theoretical values of the coefficients.

There is good reason to believe that the deformation potentials change with doping and type of impurity. Mason and Bateman [24, 25] and Csavinsky and Einspruch [26] have measured the change in the elastic constants of Si for doped samples using ultrasonic pulse techniques. They have been able to estimate the deformation potentials from their measurements, and they find that the shear deformation potential ($D_u'$) increases with increased doping. Table II shows the results of their measurements. As shown in Table II, it may be possible that $D_u'$ varies considerably. This large uncertainty will, of course, be reflected in later calculations of junction parameters.

Table I

Deformation Potential Coefficients (ev/unit dilation) for
Ge and Si.   (Kleinman's theoretical values are shown
in brackets.)

| | Si | Ge |
|---|---|---|
| $D_d$ | [-2.09] | [-2.09] |
| $D_u$ | $2.04^a$, [3.74] | $3.15^b$, [3.74] |
| $D'_u$ | $2.68^a$, [4.23] | $6.06^b$, [3.6] |
| $[\,]_d$ | [-4.99] | [-10.16] |
| $[\,]_u$ | $11^c$, $8.3^d$, [9.57] | $19.2^e$, [11.4] |
| $[\,]'_u$ | $5.7^f$ | |
| $D_d - ([\,]_d + \frac{1}{3}[\,]_u)$ | $-1.44^g$, [-0.30] | $4.82^g$, [4.27] |

a.   J. C. Hensel and G. Feher, Phys. Rev. 129, 1041 (1963).

b.   J. J. Hall, Phys. Rev. 128, 68 (1962).

c.   D. K. Wilson and G. Feher, Phys. Rev. 124, 1068 (1961).

d.   J. E. Aubrey, W. Gubler, T. Henningsen and S. H. Koenig, Phys. Rev. 130, 1667 (1963).

e.   H. Fritzche, Phys. Rev. 115, 336 (1959).

f.   J. C. Hensel and H. Hasegawa, paper presented at the International Conference on the Physics of Semiconductors, Paris, July 1964, and private communications.

g.   W. Paul, J. Phys. Chem. Solids 8, 196 (1959).

Table II

Values of the Shear Deformation Potential Coefficient $D'_u$ for
Boron Doped Si as a Function of Doping Concentration

| Concentration $(cm^{-3})$ | $D'_u$ (ev) |
|---|---|
| $1.4 \times 10^{16}$ | $8.5^b$ |
| $2.5 \times 10^{18}$ | $30^a$ |
| $3.2 \times 10^{18}$ | $5.8^b$ |
| $1.0 \times 10^{19}$ | $13^c$ |
| $1.1 \times 10^{20}$ | $11.8^b$ |

a. W. P. Mason and T. B. Bateman, "Ultrasonic Attenuation and Velocity Changes in Doped n-type Germanium and p-type Silicon and their use in Determining an Intrinsic Electron and Hole Scattering Time", Phys. Rev. Letters 10, 151, 1 March 1963.

b. P. Csavinsky and Norman G. Einspruch, "Effect of Doping on the Elastic Constants of Silicon", Phys. Rev. 132, 2434 (1963).

c. W. P. Mason and T. B. Bateman, "Ultrasonic Wave Propagation in Doped n-Germanium and p-Silicon", Phys. Rev. 134, A1387 (1964).

2.2.5 Summary

The effects of strain on the conduction minima and valence maxima of Ge and Si have been treated. These calculations have been based on the deformation potential theory of semiconductors. By way of summary, the following equations were obtained which can be used for calculating the change in energy of the valence and conduction band edge points with compressional strain:

## Valence Band of Ge and Si

$$\Delta E_{v1} = D_d e + \{(\tfrac{2}{3} D_u)^2 (e_1^2 + e_2^2 + e_3^2 - e_1 e_2 - e_1 e_3 - e_2 e_3)$$

$$+ \tfrac{1}{3}(D_u')^2 (e_4^2 + e_5^2 + e_6^2)\}^{1/2} \qquad (2.21)$$

$$\Delta E_{v2} = D_d e - \{(\tfrac{2}{3} D_u)^2 (e_1^2 + e_2^2 + e_3^2 - e_1 e_2 - e_1 e_3 - e_2 e_3)$$

$$+ \tfrac{1}{3}(D_u')^2 (e_4^2 + e_5^2 + e_6^2)\}^{1/2} \qquad (2.22)$$

where $E_{v1}$ is the "upper" hole band and $E_{v2}$ is the "lower" hole band.

## Conduction Band of Ge

$$\Delta E_{c1} = ([\,]_d + \tfrac{1}{3}[\,]_u) e + \tfrac{1}{6}[\,]_u (e_4 + e_5 + e_6) , \qquad (2.23)$$

$$\Delta E_{c2} = ([\,]_d + \tfrac{1}{3}[\,]_u) e + \tfrac{1}{6}[\,]_u (e_4 - e_5 - e_6) , \qquad (2.24)$$

$$\Delta E_{c3} = ([\,]_d + \tfrac{1}{3}[\,]_u) e + \tfrac{1}{6}[\,]_u (-e_4 + e_5 - e_6) , \qquad (2.25)$$

$$\Delta E_{c4} = ([\,]_d + \tfrac{1}{3}[\,]_u) e + \tfrac{1}{6}[\,]_u (-e_4 - e_5 + e_6) , \qquad (2.26)$$

where $E_{c1}$ is the conduction minimum in the $[111]$ and $[\bar{1}\bar{1}\bar{1}]$ directions, $E_{c2}$ is the minimum in the $[1\bar{1}\bar{1}]$ and $[\bar{1}11]$ directions, $E_{c3}$ is the minimum in the $[1\bar{1}1]$ and $[\bar{1}1\bar{1}]$ directions, $E_{c4}$ is the minimum in the $[11\bar{1}]$ and $[\bar{1}\bar{1}1]$ directions.

## Conduction Band of Si

$$\Delta E_{c1} = \begin{cases} [\,]_d e + [\,]_u e_1 - ([\,]_u' e_4)^2/\Delta E; & |e_4| \le \Delta E/(2[\,]_u') \\[2mm] [\,]_d e + [\,]_u e_1 + \dfrac{\Delta E}{4} - [\,]_u' |e_4|; & |e_4| > \Delta E/(2[\,]_u') \end{cases} \qquad (2.27)$$

$$\Delta E_{c2} = \begin{cases} []_d\, e + []_u\, e_2 - ([]'_u\, e_5)^2/\Delta E; & |e_5| \leq \Delta E/2([]'_u) \\[2ex] []_d\, e + []_u\, e_2 + \dfrac{\Delta E}{4} - []'_u\, |e_5|; & |e_5| > \Delta E/2([]'_u) \end{cases} \qquad (2.28)$$

$$\Delta E_{c3} = \begin{cases} []_d\, e + []_u\, e_3 - ([]'_u\, e_6)^2/\Delta E; & |e_6| \leq \Delta E/(2[]'_u) \\[2ex] []_d\, e + []_u\, e_3 + \dfrac{\Delta E}{4} - []'_u\, |e_6|; & |e_6| > \Delta E/(2[]'_u) \end{cases} \qquad (2.29)$$

where $E_{c1}$ is the conduction minimum in the [100] and [$\bar{1}$00] directions, $E_{c2}$ is the conduction minimum in the [010] and [0$\bar{1}$0] directions, $E_{c3}$ is the minimum in the [001] and [00$\bar{1}$] directions.

Referring to the set of Eqs. (2.23), (2.24), (2.25), (2.26) and to the set (2.27), (2.28), (2.29) it is seen that for a general strain some of the conduction minima increase in energy while others decrease. This means that electrons will populate the lowest minima and depopulate the higher minima. Likewise the valence levels shift relative to each other as shown by Eqs. (2.21) and (2.22). Again the holes will populate the higher energy level. The band gap $E_g$ is defined as the difference in energy between the lowest conduction minimum and the highest valence maximum. For hydrostatic pressure all of the conduction levels shift the same amount. Likewise the valence levels shift together. The shift of $E_g$ with strain is then simply the change in the conduction levels minus the change in the valence levels.

Chapter III

EFFECT OF STRAIN ON JUNCTION PARAMETERS

3.1  Carrier Concentration

Changes in the energy levels, as discussed in Chapter II, cause

changes in the carrier concentrations.  For non-degenerate material for

which Maxwell-Boltzmann statistics apply, the density of electrons  n

associated with an ellipsoidal energy surface at a band edge point is [27]

$$n = 2(2\pi kT/\hbar^2)^{3/2} m_c^{3/2} \exp[- (E_c - E_F)/kT] \tag{3.1}$$

where $m_c$ is the effective mass of the energy surface, $E_c$ is the energy of

the band edge point, and $E_F$ is the Fermi level.  If there are $\nu$ ellipsoidal

energy minima in k-space, the density of conduction electrons is

$$n = 2(\frac{2\pi kT}{\hbar^2})^{3/2} \{m_{c1}^{3/2} \exp[- \frac{(E_{c1} - E_F)}{kT}]$$

$$\tag{3.2}$$

$$+ m_{c2}^{3/2} \exp[- \frac{(E_{c2} - E_F)}{kT}] + \cdots + m_{c\nu}^{3/2} \exp[- \frac{E_{c\nu} - E_F}{kT}]\} .$$

The conduction band of Si has six energy minima in the <100> directions in

k-space with equal effective masses while Ge has eight minima in the <111>

directions with equal effective masses.  Pairs of energy minima are always

affected in the same manner by stress so that only three minima need be

(24)

considered for Si ([100], [010], and [001] directions) and four for Ge ([111], [1$\bar{1}\bar{1}$], [1$\bar{1}$1], and [11$\bar{1}$] directions). Referring to Eq. (3.2), the density of electrons depends on the effective mass, the energy of the particular conduction levels and the Fermi energy of the crystal. The effects of strain on the conduction minima have already been treated. It should be noted that the energy terms enter into the density relationship as an exponential while the effective mass enters as a 3/2 power. The effective mass $m_c$ may change slightly with strain; however, for the present discussion it will be assumed that it remains constant. The validity of this assumption is discussed in detail in Appendix B.

Assuming then that $m_c$ is constant and is the same for each energy minimum, the density of electrons under strained conditions for both Si and Ge can be written as

$$n = n_o \exp\left[\frac{\Delta E_F}{kT}\right] \frac{1}{\nu} \left\{ \exp\left[-\frac{\Delta E_{c1}}{kT}\right] + \cdots + \exp\left[-\frac{\Delta E_{c\nu}}{kT}\right] \right\} \qquad (3.3)$$

where $\nu = 3$ for Si and 4 for Ge, $n_o$ is the electron density in the unstrained condition, $\Delta E_F$ is the change in Fermi level, and the $\Delta E_c$'s are the changes in the energy minima of the conduction levels under strain.

The equation for the hole density differs slightly from that for electrons due to the degeneracy of the valence band levels at k = (000). The hole density, p, is

$$p = 2\left(\frac{2\pi kT}{\hbar^2}\right)^{3/2} \left\{ m_{v1}^{3/2} \exp\left[-\frac{(E_F - E_{v1})}{kT}\right] \right.$$

$$\left. + m_{v2}^{3/2} \exp\left[-\frac{(E_F - E_{v2})}{kT}\right] + m_{v3}^{3/2} \exp\left[-\frac{(E_F - E_{v3})}{kT}\right] \right\} \qquad (3.4)$$

where $E_{v1}$ and $E_{v2}$ are the energies of the $\Gamma'_{25}(j = 3/2)$ levels (heavy and light hole bands) and $E_{v3}$ is the energy of the $j = 1/2$ level. It will be assumed here that the $j = 1/2$ level can be neglected compared to the $j = 3/2$ level because it has a smaller effective mass and is lower in energy. The third term in Eq. (3.4) is thereby neglected. (This is a good assumption for Ge while for silicon the error in p will be less than 20%.)

In the unstrained case $E_{v1}$ and $E_{v2}$ are equal so that an effective mass $m_v^*$ can be defined for the combination of the two levels as follows

$$m_v^* = [m_{v1}^{3/2} + m_{v2}^{3/2}]^{2/3} . \tag{3.5}$$

This is the normal hole effective mass. Again it will be assumed that the effective mass of the individual levels do not change with strain (see Appendix B). The hole density under strain becomes

$$p = p_o \left\{ \frac{m_{v1}^{3/2}}{(m_v^*)^{3/2}} \exp\left[-\frac{\Delta E_F - \Delta E_{v1}}{kT}\right] + \frac{m_{v2}^{3/2}}{(m_v^*)^{3/2}} \exp\left[-\frac{\Delta E_F - \Delta E_{v2}}{kT}\right] \right\} \tag{3.6}$$

where $p_o$ is the hole density with zero strain.

Equations (3.3) and (3.6) are valid for either p- or n-type material. In non-degenerate n-type material, with zero applied stress, the electron density is approximately equal to the net donor density. Likewise, in non-degenerate p-type material the hole density is approximately equal to the net acceptor density. The effects of strain on impurity states in Ge and Si are not completely known. For hydrostatic stress, experiment has shown that the changes in impurity ionization energy are negligible compared with band gap changes [28]. Hall has

shown that ionization energy decreases with strain for large <111> uniaxial stresses in Al and In doped Ge [29]. Kohm [30] has also given a theoretical discussion in which it is suggested that the change in ionization energy is second order for shear strains. It will be assumed that shifts in ionization energy of impurities can be neglected and that the majority carrier concentration is independent of strain.

Since both the valence and conduction bands shift with strain, the Fermi level must also shift. This can be seen for p-type material by setting Eq. (3.6) equal to the acceptor density $N_a$. Since the ionization energy has been assumed to be independent of stress, the hole density remains constant, and

$$\exp[\frac{\Delta E_F}{kT}] = \frac{m_{v1}^{3/2}}{(m_v^*)^{3/2}} \exp[\frac{\Delta E_{v1}}{kT}] + \frac{m_{v2}^{3/2}}{(m_v^*)^{3/2}} \exp[\frac{\Delta E_{v2}}{kT}] \tag{3.7}$$

Substituting Eq. (3.7) into Eq. (3.3) and solving for the minority carrier concentration gives

$$n_p/n_{po} = (1/v) \left\{ \frac{m_{v1}^{3/2}}{(m_v^*)^{3/2}} \exp[\frac{\Delta E_{v1}}{kT}] + \frac{m_{v2}^{3/2}}{(m_v^*)^{3/2}} \exp[\frac{\Delta E_{v2}}{kT}] \right\}$$
$$\times \left\{ \exp[-\frac{\Delta E_{c1}}{kT}] + \cdots + \exp[-\frac{\Delta E_{cv}}{kT}] \right\} \tag{3.8}$$

where $n_p$ is the minority carrier concentration with strain and $n_{po}$ is the unstrained minority carrier concentration. If a similar calculation is made for n-type material, it is found that the same expression results for $p_n/p_{no}$ so that the minority carrier density can be written in general as

$$\gamma_v(e) = \frac{p_n}{p_{no}} = \frac{n_p}{n_{po}} = (1/v) \left\{ \frac{m_{v1}^{3/2}}{(m_v^*)^{3/2}} \exp\left[-\frac{\Delta E_{v1}}{kT}\right] + \frac{m_{v2}^{3/2}}{(m_v^*)^{3/2}} \exp\left[-\frac{\Delta E_{v2}}{kT}\right] \right\}$$

$$\times \left\{ \exp\left[-\frac{\Delta E_{c1}}{kT}\right] + \cdots + \exp\left[-\frac{\Delta E_{cv}}{kT}\right] \right\} \tag{3.9}$$

The factor $\gamma_v(e)$ gives the ratio of minority carrier density under strain to minority carrier density with zero applied strain. For hydrostatic stress Eq. (3.9) reduces to

$$\gamma_v(e) = \exp\left(-\frac{\Delta E_g}{kT}\right) \tag{3.10}$$

Figures 8 and 9 are plots of $\gamma_v(e)$ for Si and Ge respectively as a function of uniaxial compression stresses for several orientations. The uniaxial stresses were calculated as shown in Appendix A. The experimental values of the deformation potentials as shown in Table I and II were used in the calculations. Note in Figs. 8 and 9 that hydrostatic stress causes the minority carrier concentration for Ge to decrease while it causes the minority carrier concentration of Si to increase. Also $\gamma_v(e)$ is more sensitive to <100> uniaxial stresses in Si while <111> uniaxial stresses cause larger changes in Ge.

The above treatment of the effect of strain on carrier concentration is based on two assumptions (1) no change in effective mass with strain and (2) no change in ionization energy with strain.

The pn product (pn = $n_i^2$) is an important parameter in semiconductor theory because at equilibrium it remains constant with position in p-n junction devices. It does however change with strain. This can be seen by forming the pn product from Eqs. (3.3) and (3.6)
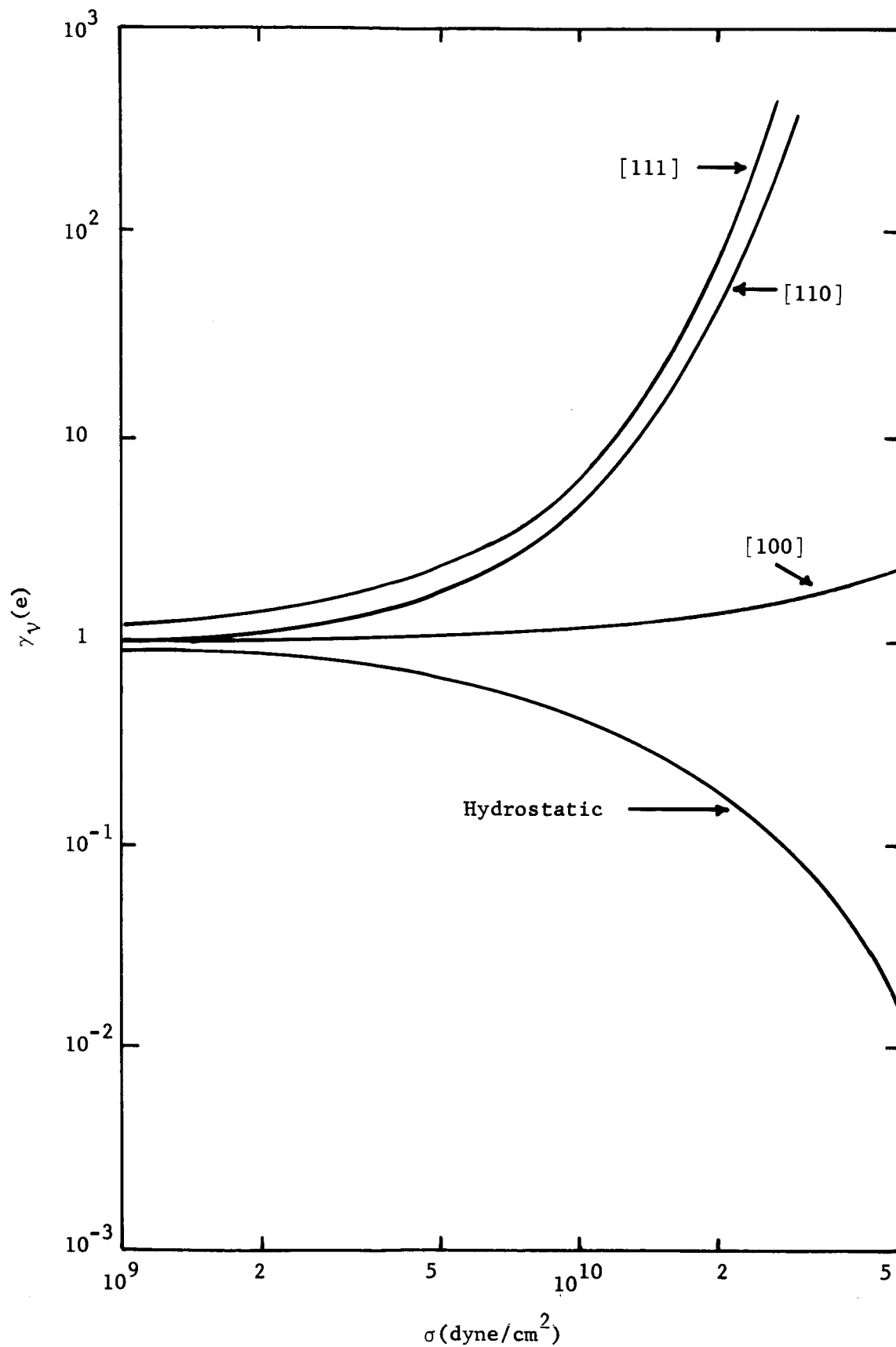
Fig. 8.   Ratio of Stressed to Unstressed Minority Carrier Density for Ge as a Function of Stress for Hydrostatic, [100], [110], and [111] Uniaxial Stress.
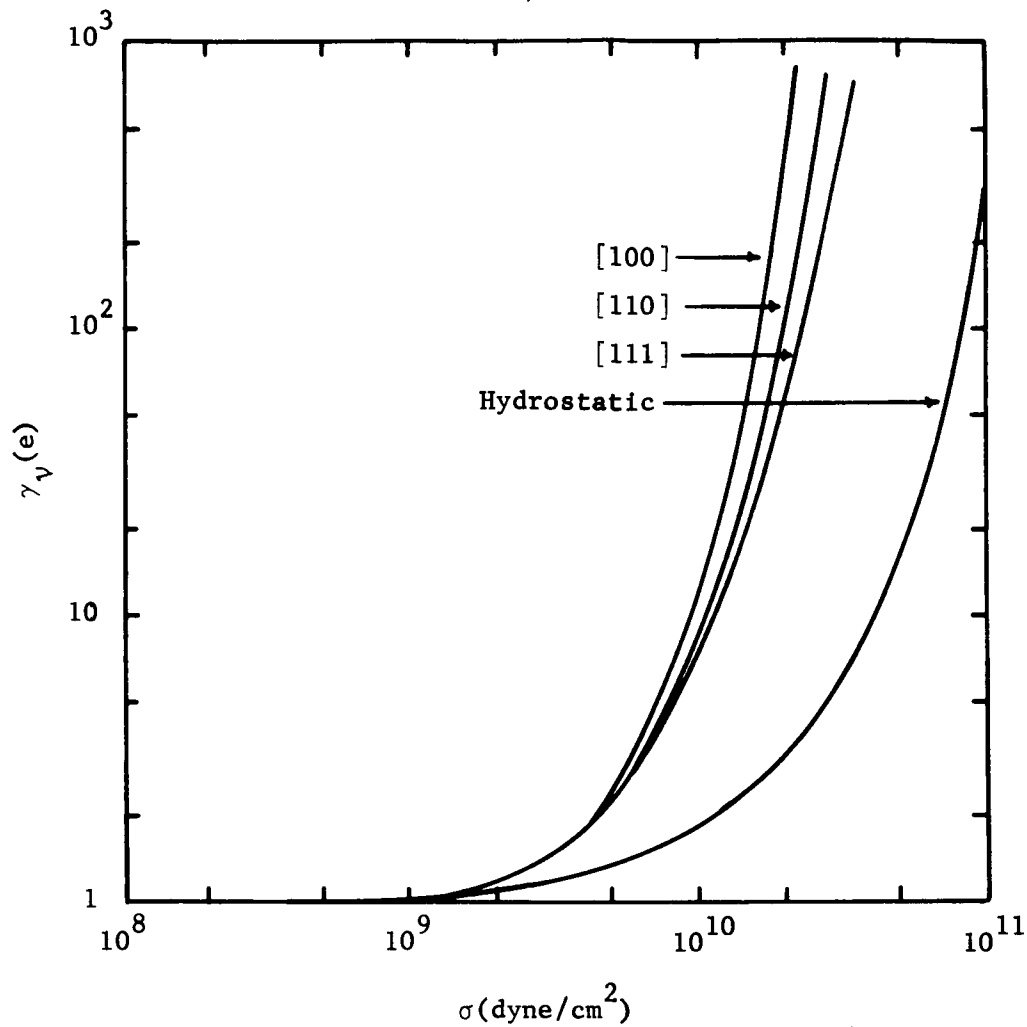
Fig. 9. Ratio of Stressed to Unstressed Minority Carrier Density, $\gamma_\nu(e)$, for Si as a Function of [100], [110], [111] and Hydrostatic Stress.

$$n_i^2 = pn = p_o n_o \, \gamma_\nu(e) \ . \tag{3.11}$$

Rewriting Eq. (3.11) gives

$$n_i^2 = n_{io}^2 \, \gamma_\nu(e) \tag{3.12}$$

where $n_i$ is the intrinsic carrier concentration under strain and $n_{io}$ is the intrinsic carrier concentration with zero strain.

## 3.2 Effect of Strain on the "Ideal" Current Components of p-n Junctions

This section discusses the "ideal" or diffusion currents in p-n junctions as predicted by the Shockley model. Generation-recombination currents are discussed in the following section. The p-n junction model to be discussed is shown in Fig. 10, where $A_T$ is the total junction area, $A_{sn}$ and $A_{sp}$ are the stressed areas at the edges of the depletion region on the n and p sides respectively, $W_n$, $W_p$, and $W_d$ are the respective widths of the n region, p region, and depletion region. The hole and electron currents are

$$I_p = \frac{qA_T D_p p_n}{L_p} \coth(\frac{W_n}{L_p}) \{\exp[\frac{qV_a}{kT}] - 1\} \tag{3.13}$$

$$I_n = \frac{qA_T D_n n_p}{L_n} \coth(\frac{W_p}{L_n}) \{\exp[\frac{qV_a}{kT}] - 1\} \tag{3.14}$$

where $D_p$ and $D_n$ are the hole and electron diffusion coefficient, $L_p$ and $L_n$ are the hole and electron diffusion lengths, $p_n$ and $n_p$ are the equilibrium minority carrier densities at the edges of the depletion region on the n and p sides of the junction respectively, and $V_a$ is the junction voltage.

Under stress there are two regions of the junction which must be considered. The current in the unstressed area is given by replacing $A_T$ with $A_T - A_{sn}$ in Eq. (3.13) and $A_T - A_{sp}$ in Eq. (3.14). The current through the stressed areas will be modified by the stress induced changes in the parameters. As shown in Figs. 8 and 9, the minority carrier concentrations change by several orders of magnitude for large strains. It is assumed here that changes in the other parameters are negligible compared to changes in minority carrier densities. This assumption is discussed in Appendix C.
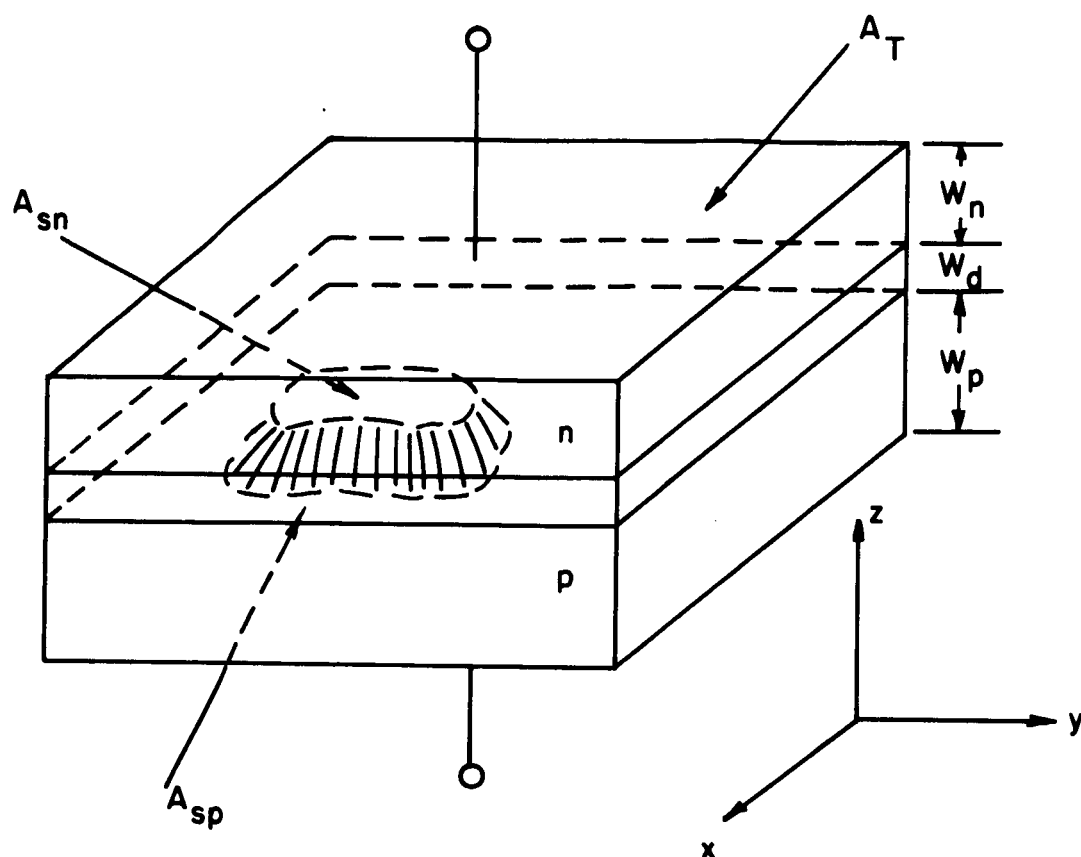
Fig. 10. Stressed p-n Junction Model.

Taking into account the stressed and unstressed regions, the equation for the "ideal" component of diode current can be written:

$$I_s = \frac{I_I}{\exp\left[\frac{qV}{kT}\right] - 1}$$

$$= I_{po}\left\{\frac{A_T - A_{sn}}{A_T} + \frac{1}{A_T}\int_{A_{sn}} \gamma_\nu(e_n)\ dx\ dy\right\} \tag{3.15}$$

$$+ I_{no}\left\{\frac{A_T - A_{sp}}{A_T} + \frac{1}{A_T}\int_{A_{sp}} \gamma_\nu(e_p)\ dx\ dy\right\},$$

where $I_I$ is the "ideal" diode current, $I_s$ is the reverse saturation current, $e_n$ and $e_p$ are the position dependent strains at the edges of the depletion region on the n and p sides respectively, and

$$I_{po} = \frac{qA_T D_p p_{no}}{L_p} \coth\left(\frac{W_n}{L_p}\right) ,$$

$$\tag{3.16}$$

$$I_{no} = \frac{qA_T D_n n_{po}}{L_n} \coth\left(\frac{W_p}{L_n}\right) .$$

Defining an effective ratio of minority carrier densities as,

$$\bar{\gamma}_\nu(e) \equiv \frac{1}{A_s} \int_{A_s} \gamma_\nu(e) \, dxdy ,$$

Eq. (3.15) reduces to

$$I_s = I_{po}\left\{\frac{A_T - A_{sn}}{A_T} + \frac{A_{sn}}{A_T} \bar{\gamma}_\nu(e_n)\right\} + I_{no}\left\{\frac{A_T - A_{sp}}{A_T} + \frac{A_{sp}}{A_T} \bar{\gamma}_\nu(e_p)\right\} . \tag{3.17}$$

Two special cases are of interest. The first occurs when the stress is symmetric across the junction, so that $A_{sn} = A_{sp} = A_s$, and $\bar{\gamma}_\nu(e_p) = \bar{\gamma}_\nu(e_n) = \bar{\gamma}_\nu(e)$. Then

$$I_s = [I_{po} + I_{no}]\left[\frac{A_T - A_s}{A_T} + \frac{A_s}{A_T} \bar{\gamma}_\nu(e)\right] . \tag{3.18}$$

or

$$I_s = I_{so}\left[\frac{A_T - A_s}{A_T} + \frac{A_s}{A_T} \bar{\gamma}_\nu(e)\right] , \tag{3.19}$$

where $I_{so}$ is the unstrained saturation current.

For hydrostatic pressure the stressed area is equal to the total area and $\gamma_\nu(e) = \exp\left[-\frac{\Delta E_g}{kT}\right]$. The reverse saturation current is then

$$I_s = I_{so} \exp\left[-\frac{\Delta E_g}{kT}\right] \tag{3.20}$$

For $\frac{\Delta E_g}{kT} \ll 1$, this may be written as

$$\frac{\Delta I_s}{I_s} \approx -\left[\frac{\Delta E_g}{kT}\right] \tag{3.21}$$

where $\Delta I_s$ is the change in saturation current for a change in band gap of $\Delta E_g$. This equation agrees with the results obtained by Hall, et. al. [31].

The dependence, on temperature, of the current through a stressed diode can be described. Referring to Eqs. (3.16) and (3.17), $\bar{\gamma}_v(e_n)$ and $\bar{\gamma}_v(e_p)$ as well as the diffusion coefficient, the diffusion lengths, and the minority carrier densities are temperature dependent. For small temperature variations near room temperature, only the changes in carrier density, $\bar{\gamma}_v(e_n)$ and $\bar{\gamma}_v(e_p)$ need be considered. The carrier densities $p_n$ and $n_p$ are proportional to $\exp\left[-\frac{E_g}{kT}\right]$ [32]. For large strains, $\bar{\gamma}_v(e) \propto \exp\left[-\frac{\Delta E_g}{kT}\right]$ where $\Delta E_g$ is of course strain dependent. For the case where the stress is symmetric across the junction and

$$\frac{A_s}{A_T} \bar{\gamma}_v(e) \gg \frac{A_T - A_s}{A_T}$$

(valid at high stress or when the entire junction is stressed),

$$I \propto \{\exp\left[\frac{qV}{kT}\right] - 1\} \exp\left[-\frac{E_g}{kT}\right] \exp\left[-\frac{\Delta E_g}{kT}\right] . \tag{3.22}$$

If $\frac{qV}{kT} \gg 1$

$$\frac{\partial \ln I}{\partial T} = \frac{1}{kT^2} [E_g + \Delta E_g - qV] , \tag{3.23}$$

devices when subjected to strains. They argue that the trap levels result as a consequence of dislocations introduced in the crystal by strain. It has been shown that small spherical indentor points can cause permanent indentations into the surface of germanium crystals at room temperature without any apparent fracture of the material 34, 35 . Further it has been shown that dislocations can be observed on the indented surfaces when etched 34 . Accepting the fact that dislocations can be introduced by high strains does not mean that they result in trap levels that are electrically active in p-n junctions. However there is good reason to suspect that such levels would be active.

Experimental observations on the piezojunction effect have shown that apparently the phenomenon is reversible at least over limited ranges. This means that if the introduction of generation-recombination levels by strain is the underlying mechanism responsible for the piezojunction effect it too must be reversible. At room temperature there is some doubt that generation-recombination centers could be created with strain and then disappear when strain is removed. This process would be much more likely to occur at very high temperatures. It seems very unlikely that the levels would be reversible and the number exponentially related to strain as required by the observations.

The second aspect of generation-recombination currents (change in the relative position of the trap energy with respect to the conduction and valence bands) can be important. The following discussion treats this problem. Hauser 36 has derived an approximate theoretical expression for the current for a single trap level located in the forbidden band. A review of Hauser's work is given in Appendix E. The space charge generation-recombination current, $J_U$, is given by:

and when $\frac{qV}{kT} \ll -1$,

$$\frac{\partial \ell n I}{\partial T} = \frac{1}{kT^2}[E_g + \Delta E_g] \ . \tag{3.24}$$

As shown in the above equations the slope of $\ell n I$ vs T depends upon the stress through $\Delta E_g$. $\Delta E_g$ is negative for uniaxial compressive stresses. Therefore the slope of $\ell n$ I vs T decreases with increasing stress.

The effect of a large stress applied to a small area of a p-n junction is to cause the "ideal" or diffusion current through the small area to increase. For high stress levels the current through the stressed area can become much larger than that through the unstressed area, hence the total diode current is essentially that flowing in the stressed area.

## 3.3 Effect of Strain on the Space Charge Generation-Recombination Current in p-n Junctions

Space charge generation-recombination current can be important in p-n junctions (particularly in silicon) [33]. This current adds to the "ideal" or diffusion current which is predicted by the Shockley theory. Mechanical strain can cause a change in generation-recombination currents in two ways. First, strain can cause the generation-recombination current to increase by simply increasing the number of generation-recombination centers located in or near the space charge region of a p-n junction. The second way strain can change the generation-recombination current is to shift the relative position of the energy of the trap levels with respect to the conduction and valence levels.

Rindner, et. al. [5,6] have suggested that the first effect, creation of trap centers by strain, is in fact the underlying mechanism responsible for large changes observed in the electrical characteristics of p-n junction

$$J_U = \frac{qn_i^2 \, W[\exp\{qV_a/kT\} - 1]}{(\tau_{no}p_1 + \tau_{po}n_1) \, (1 + \frac{[\tau_{no} + \tau_{po}] \, n_i \, \exp\{qV_a/kT\}}{[\tau_{no}p_1 + \tau_{po}n_1]})} \qquad (3.25)$$

where W is the width of the space charge region, $V_a$ is the applied voltage, $\tau_{no}$ is the lifetime for electrons injected into highly p-type material, and $\tau_{po}$ is the lifetime for holes injected into highly n-type material. The hole and electron densities $p_1$ and $n_1$ are given by [33]

$$n_1 = n_i \, \exp(E_t - E_i)/kT \qquad (3.26)$$

$$p_1 = n_i \, \exp(E_i - E_t)/kT \qquad (3.27)$$

where $E_t$ is the energy of the trap level and $E_i$ is the energy of the intrinsic Fermi level. The width of the space charge region, W, is a function of the applied voltage. For a step junction the width is

$$W = W_o(1 - V_a/V_o)^{1/2} , \qquad (3.28)$$

where $W_o$ is the width with zero applied voltage and $V_o$ is the built-in junction potential.

To see how the generation-recombination current changes with mechanical strain, each parameter in Eq. (3.25) is analyzed. The intrinsic carrier density has already been discussed in Sect. 3.1. Again it will be assumed that $\tau_{no}$ and $\tau_{po}$ are strain independent (see Appendix C). The built-in potential is related to the intrinsic carrier concentration by

$$V_o \propto \ell n(\frac{N_a N_d}{n_i^2}) \qquad (3.29)$$

Since changes in $V_o$ are logarithmically related to changes in $n_i^2$, it will be assumed that $V_o$ and hence W are independent of strain when compared to changes in $n_i$.

This leaves only $p_1$ and $n_1$ to be discussed. They are related to the energy of the trap level as shown by Eqs. (3.26) and (3.27). Unfortunately there is no information available on the effect of a general strain on $E_t$. In the absence of this information it is not possible to predict how $J_U$ varies with strain in the reverse biased and low forward biased regions.

For large forward biases $J_U$ is independent of $p_1$ and $n_1$. For this case $J_U$ is given by (see Appendix E):

$$J_U = \frac{qn_i W}{\tau_{no} + \tau_{po}} \exp\{qV_a/2kT\} \tag{3.30}$$

Substituting Eq. (3.12) into Eq. (3.30) one finds

$$J_U(e) = J_U(o) \sqrt{\gamma_\nu(e)} , \tag{3.31}$$

or

$$\frac{I_U(e)}{I_U(o)} = \sqrt{\gamma_\nu(e)} , \tag{3.32}$$

where $J_U(o)$ is the unstrained generation-recombination current. As shown by the above equations, the generation-recombination current is not as strain sensitive as the ideal current.

Taking into account the stressed and unstressed regions as was done for the "ideal" current, the generation-recombination current is

$$I_U = \left[\frac{A_T - A_s}{A_T} + \frac{A_s}{A_T} \sqrt{\bar{\gamma}_\nu(e)}\right] I_U(o) \tag{3.33}$$

It should be noted that it is the strain in the junction that is important here as opposed to the strain at the edge of the depletion region in the ideal current.

## 3.4  Effect of Stress on Transistor Characteristics

A p-n-p junction transistor model is considered.  The equations for the electron and hole components of emitter current are [32]

$$I_{pe} = p_n \{K_1 [\exp(\frac{qV_{eb}}{kT}) - 1] + K_2 [\exp(- \frac{qV_{cb}}{kT}) - 1]\} \tag{3.34}$$

and

$$I_{ne} = n_p K_3 \left\{ \exp[\frac{qV_{eb}}{kT}] - 1 \right\} \tag{3.35}$$

where $K_1$, $K_2$, and $K_3$ are functions of the device dimensions and material constants, $n_p$ and $p_n$ are the minority carrier densities in the emitter and base respectively, $V_{eb}$ is the emitter-base voltage, and $V_{cb}$ is the collector-base voltage.  The minority carrier densities are shown explicitly to indicate the dependence of $I_{pe}$ and $I_{ne}$ on stress.  Under normal forward bias transistor operation, $qV_{eb}/kT \gg 1$ and $qV_{cb}/kT \gg 1$.  Using these restrictions, the emitter currents under stress conditions similar to those discussed for the p-n junction are

$$I_{pe} \approx I_{po} \{A_b + B_b \bar{\gamma}_v(e_b)\} \exp \frac{qV_{eb}}{kT} , \tag{3.36}$$

$$I_{ne} \approx I_{no} \{A_e + B_e \bar{\gamma}_v(e_e)\} \exp \frac{qV_{eb}}{kT} , \tag{3.37}$$

where $I_{po} = K_1 p_{no}$, $I_{no} = K_3 n_{po}$, $A_b = (A_T - A_{sn})/A_T$, $A_e = (A_T - A_{sp})/A_T$, $B_b = A_{sn}/A_T$, and $B_e = A_{sp}/A_T$.

The base current is

$$I_b = I_{ne} + I_r \equiv I_{ne} + \theta I_{pe} , \tag{3.38}$$

since $I_r$, the total recombination current (bulk and surface), is proportional to $I_{pe}$. Combining Eqs. (3.36), (3.37) and (3.38) gives for the emitter current, $I_e = I_{pe} + I_{ne}$; base current; and collector current, $I_c = I_e - I_b$:

$$I_e = \exp[\frac{qV_{eb}}{kT}]\{I_{po}[A_b + B_b \, \bar{\gamma}_\nu(e_b)] + I_{no}[A_e + B_e \, \bar{\gamma}_\nu(e_e)]\} \qquad (3.39)$$

$$I_b = \exp[\frac{qV_{eb}}{kT}]\{\theta I_{po}[A_b + B_b \, \bar{\gamma}_\nu(e_b)] + I_{no}[A_e + B_e \, \bar{\gamma}_\nu(e_e)]\} \qquad (3.40)$$

$$I_c = \exp[\frac{qV_{eb}}{kT}](1 - \theta) \, I_{po}[A_b + B_b \, \bar{\gamma}_\nu(e_b)] \qquad (3.41)$$

The forward grounded base current gain $\alpha$ is

$$\alpha = (\frac{\partial I_c}{\partial I_e})_{V_{cb}} = \frac{1 - \theta}{1 + \dfrac{I_{no}}{I_{po}} \dfrac{A_e + B_e \, \bar{\gamma}_\nu(e_e)}{A_b + B_b \, \bar{\gamma}_\nu(e_b)}} \qquad (3.42)$$

It has been assumed in the preceding equations that the emitter-base voltage is the same for the stressed and unstressed regions. If the stressed region is small compared with the total junction area there can be a significant base spreading resistance associated with the stressed area. In this case the equations becomes:

$$I_e = \{I_{po}[A_b + B_b \, \bar{\gamma}_\nu(e_b) \, \exp(- \frac{qRI_{bs}}{kT})]$$
$$+ I_{no}[A_e + B_e \, \bar{\gamma}_\nu(e_e) \, \exp(- \frac{qRI_{bs}}{kT})]\} \, \exp[\frac{qV_{eb}}{kT}] \quad , \qquad (3.43)$$

$$I_b = \{I_{no}[A_e + B_e \, \overline{\gamma}_\nu(e_s) \, \exp(-\frac{qRI_{bs}}{kT})]$$

$$+ \theta I_{po}[A_b + B_b \, \overline{\gamma}_\nu(e_b) \, \exp(-\frac{qRI_{bs}}{kT})]\} \, \exp[\frac{qV_{eb}}{kT}] \; , \qquad (3.44)$$

$$I_c = I_{po}(1 - \theta)[A_b + B_b \, \overline{\gamma}_\nu(e_b) \, \exp(-\frac{qRI_{bs}}{kT})] \, \exp[\frac{qV_{eb}}{kT}] \; , \qquad (3.45)$$

where R is the spreading resistance and $I_{bs}$ is the base current flowing into the stressed area:

$$I_{bs} = I_{no} \, B_e \, \overline{\gamma}_\nu(e_s) \, \exp[\frac{qV_{eb} - qRI_{bs}}{kT}] \; . \qquad (3.46)$$

The base resistance associated with the unstressed part of the emitter-base junction has been neglected. The inclusion of the spreading resistance term makes the analysis considerably more difficult since a transcendental equation must be solved for $I_{bs}$; however, the major features are the same as before. Changes in R have been neglected here. The effect of large strains on conductivity are discussed in Appendix D.

All of the equations developed for p-n-p transistors will hold for n-p-n transistors if n and p are interchanged each time they appear.

As an example of the transistor theory, consider a silicon p-n-p transistor with the following parameters:

$$A_T = 5 \times 10^{-5} \; cm^2$$

$$I_{po} = 5 \times 10^{-15} \; amp$$

$$I_{no}/I_{po} = 10^{-3}$$

$$\theta = 2 \times 10^{-2}$$

$$\rho_{base} = 2 \; ohm\text{-}cm$$

Let the stress be applied over a circle of diameter $d = 3.56 \times 10^{-4}$ cm. The spreading resistance of a flat circular area is

$$R \approx \frac{\rho_{base}}{2d} = 2800 \text{ ohms} .$$

Case I. Let the stress be applied in the [111] directon to both sides of the emitter-base junction, $e_e = e_b$, $A_{sn} = A_{sp} = 10^{-7}$ cm$^2$. Figure 11 is a plot of base current $I_b$ as a function of emitter-base voltage $V_{eb}$ for several stress levels. Figure 12 is a plot of collector current as a function of $V_{eb}$ for the same stress levels. As shown by the curves, both $I_b$ and $I_c$ are changed by several orders of magnitude for small changes in stress in the high stress region. The effect of spreading resistance is shown by the convergence of $I_b$ and $I_c$ toward their unstressed value for high applied voltages. The effect of stress on the spreading resistance has been neglected. It would reduce the resistance and thereby cut down on the rate at which the stressed curves converge to the unstressed curves. The larger the spreading resistance the more rapidly the currents converge to their unstressed values. Note that $\alpha$ is not affected by the stress when both sides of the emitter-base junction are stressed Eq. (3.42).

Case II. Assume the same conditions as before except that only the emitter side of the emitter-base junction is stressed $e_e \gg e_b$. Figure 13 is a plot of $I_b$ and $I_c$ as a function of $V_{eb}$ for several stress conditions. Note that $I_c$ is not changed by the stress while $I_b$ is changed. This means that $\alpha$ is changed. In this case, where $\theta > I_{no}/I_{po}$, the base current is not as sensitive to stress as it was for the previous case.
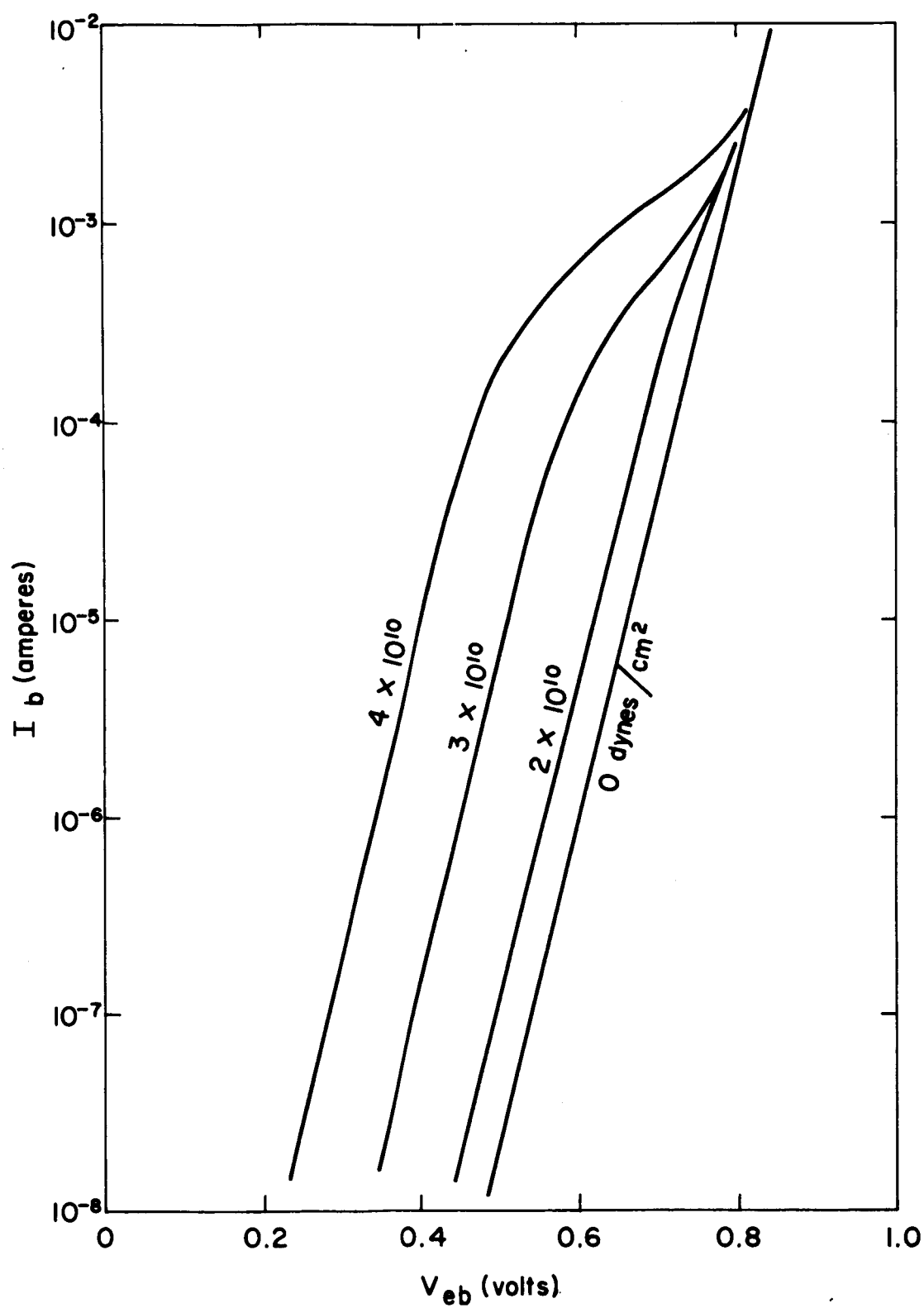
Fig. 11.  Effect of Stress on Transistor Base Current for a Symmetrically
Stressed Emitter-base Junction.
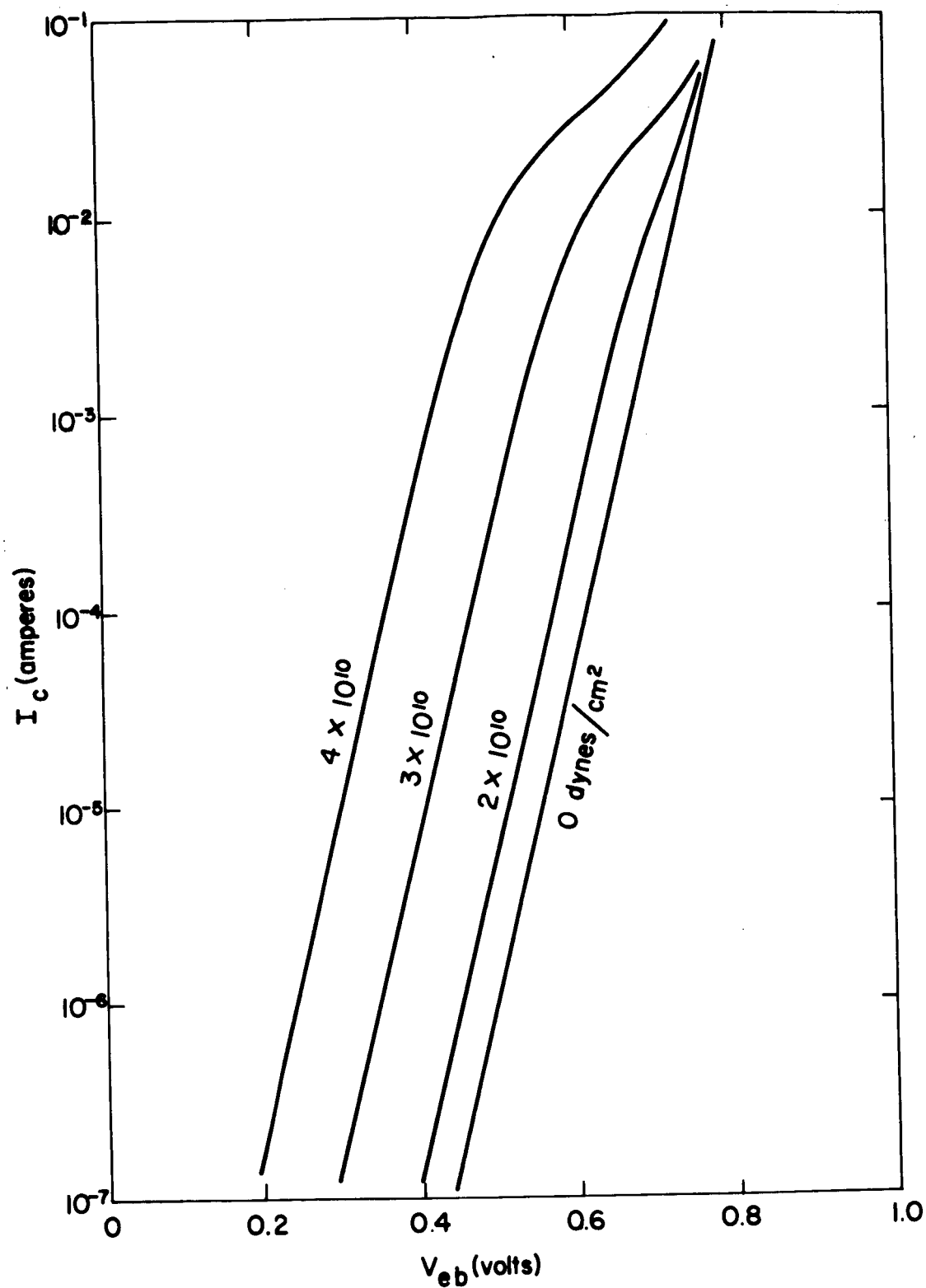
Fig. 12. Effect of Stress on Collector Current for a Symmetrically Stressed Emitter-base Junction.
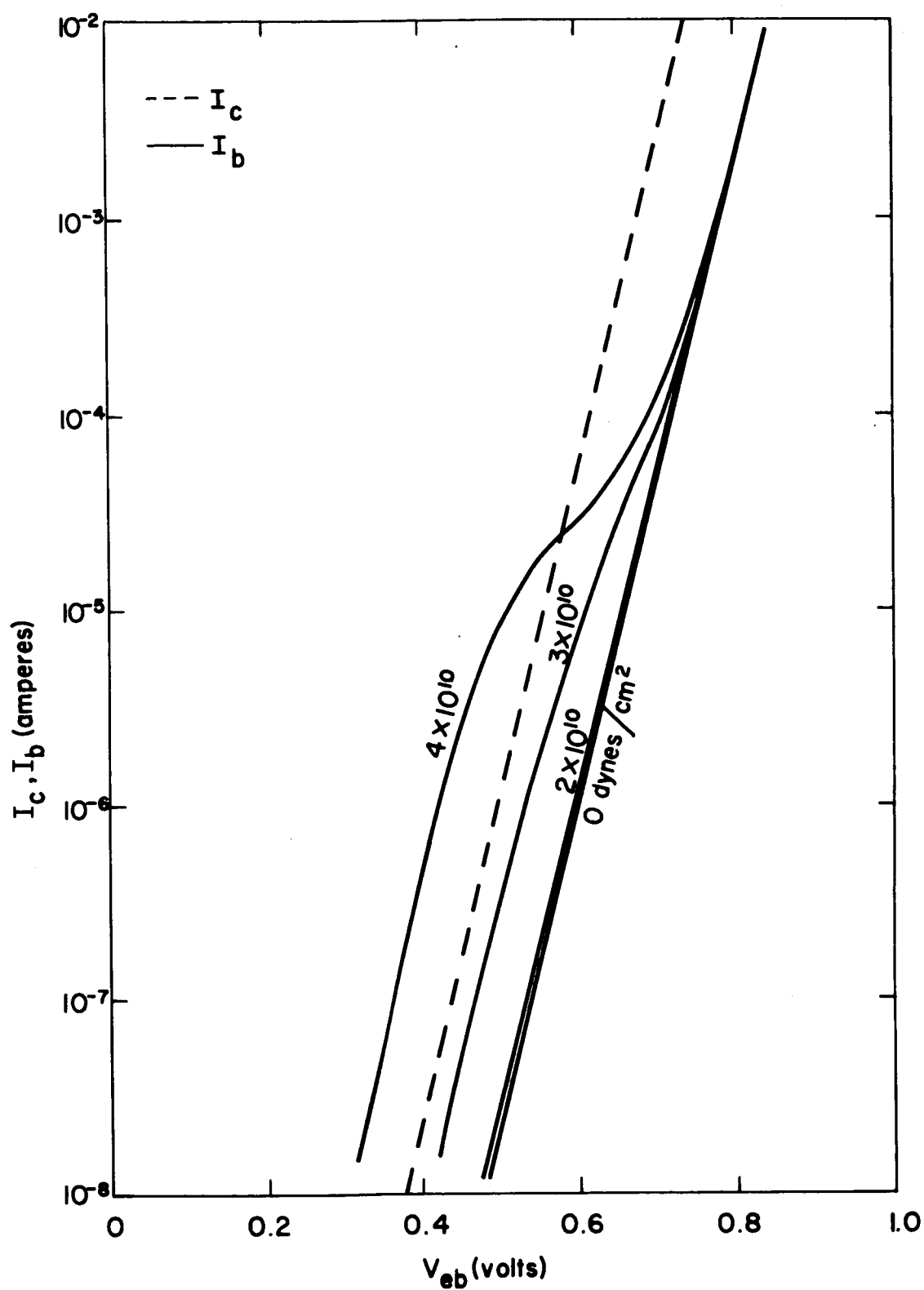
Fig. 13.   Collector and Base Current as a Function of Emitter-base
Voltage for Several Stress Levels in the Emitter Only.

In Fig. 14, $I_c/I_{co}$ is plotted as a function of stress for constant emitter current and for constant base current, where $I_{co}$ is the collector current with no stress. Spreading resistance was neglected in these calculations. As shown, changes in $I_c/I_{co}$ are larger when the base current is held constant as compared to holding the emitter current constant.

Case III. Assume that the stress is applied only to the base side of the emitter-base junction ($e_e \ll e_b$). Using the assumed transistor parameters in Eqs. (3.42) and (3.44) it can be shown that $\alpha$ and $I_b$ will remain approximately constant. However, in devices where $\theta$ is very small compared to $I_{no}/I_{po}$ (Ge for example) the base current can change significantly depending upon the ratio of $I_{no}/I_{po}$. For constant base current, the collector current is constant.

These examples are not intended to be a complete analysis of the many implications of the preceding theory of stressed transistors but are intended to illustrate some of its salient features.

3.5 Discussion

The preceding theory considers both the effect of strain on the "ideal" and bulk generation-recombination currents in p-n junctions. The theory of the "ideal" currents neglects any effects other than band gap changes. The bulk generation-recombination theory assumes that stress does not increase the number of trapping centers but rather it changes the relative position of the energy of existing trap levels with respect to the conduction and valence levels. It has not been possible to treat the generation-recombination current except in the forward biased case since the energy levels of the traps cannot, at this time, be described as a function of strains.
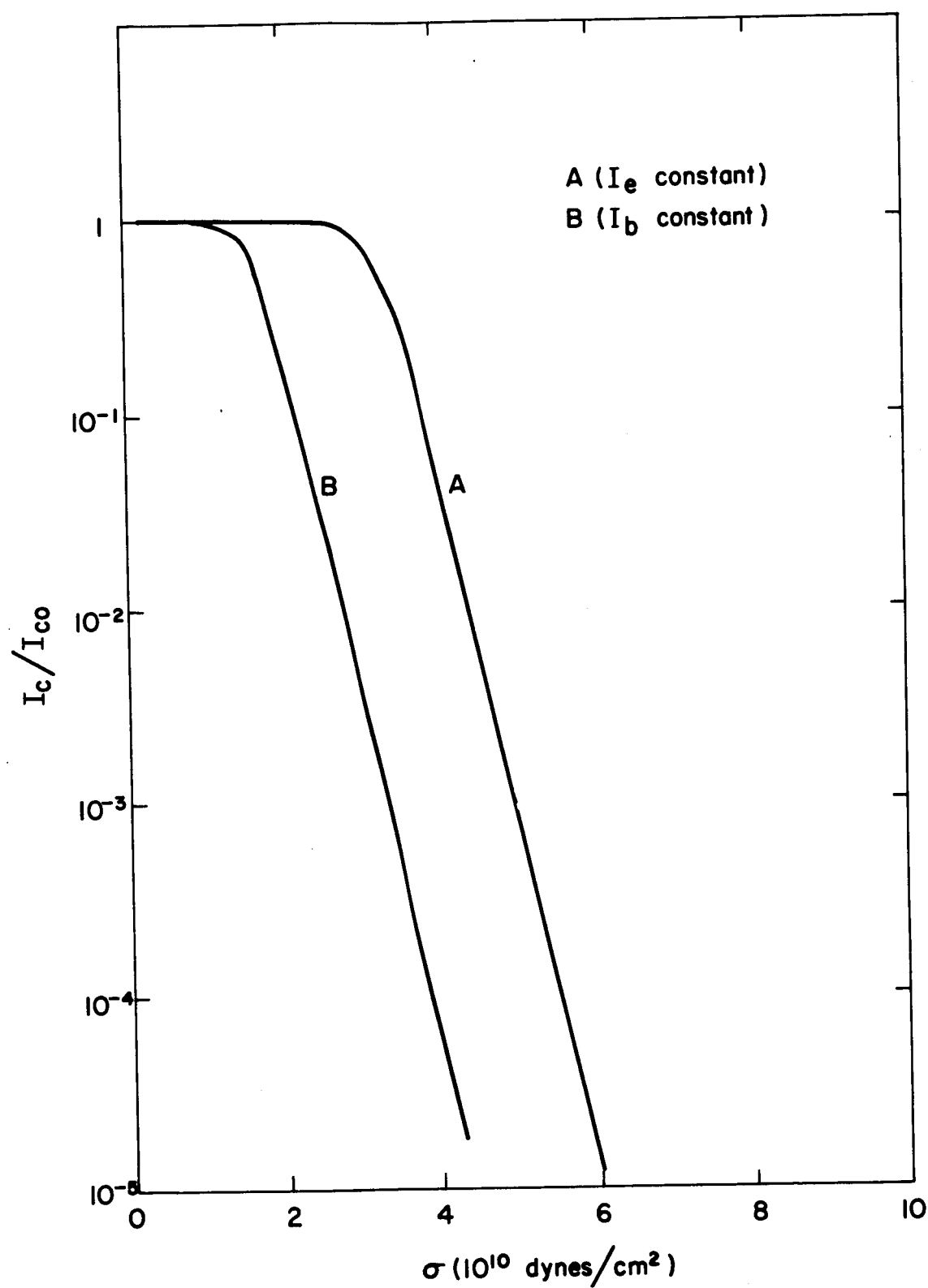
Fig. 14. Effect of Stress on Normalized Collector Current for Constant
Emitter Current and for Constant Base Current. Stressed only
in the emitter.

In regards to the introduction of new trap levels with strain, it is very likely that if these levels were created they would remain and hence the electrical characteristics would not be reversible with strain. That is, as new centers are created they too could contribute to the current but would not disappear when the strain is removed.

Another problem which has not been discussed here and which is important is generation-recombination currents which are located at or near the surface of the diode structure. Most methods of applying mechanical stress do not apply stress to the surfaces that are important in determining these currents. At the present time there is no way of predicting the effect of strain on these currents.

Chapter IV

EXPERIMENTAL


4.1  Introduction

A variety of experimental measurements have been made on silicon diodes, transistors, and 4-layer diodes in order to determine the effect of large anisotropic stresses on the electrical characteristics of the devices. While most of the test devices were fabricated in the laboratory, some were obtained from commercial sources.  The devices fabricated in the laboratory were designed specifically to allow measurements to be made which would delineate the effect on the piezojunction phenomenon of such parameters as crystal orientation, junction depth, and material resistivity.  The object of the experimental work has been to acquire an understanding of the phenomenon and to check the applicability of the theory with the goal of applying the phenomenon in stress transducer applications.


4.2  Experimental Apparatus

An experimental test station was built and calibrated.  The primary purpose of this apparatus was to apply a known mechanical stress to a semiconductor junction device and to measure the appropriate electrical parameters under various stress conditions.  To obtain the large mechanical stress necessary to change the electrical characteristics of the devices, it

(49)

was necessary to restrict the stressed area to less than ten square mils

in order to work with practical forces, 0 to $10^5$ dynes. This was accomplished

in all cases by using either a steel, sapphire or diamond phonograph needle.

Figure 15 is a schematic diagram of the stressing apparatus. Figure

16 is a photograph of the test station. The needle or indentor point which

was used to apply the stress to the device was mounted near the end of a

phonograph pick-up arm in much the same mannner as that normally used in a

phonograph system. A dc solenoid was attached to the stationary part of

the pick up arm a short distance from the pivot point of the arm. The

plunger of the solenoid was attached to the arm. This arrangement permitted

a continuous force range of 0 to $10^5$ dynes by simply varying the current

supplied to the solenoid. The force was calibrated in terms of the solenoid

current. The device to be tested was mounted under the needle on a precision
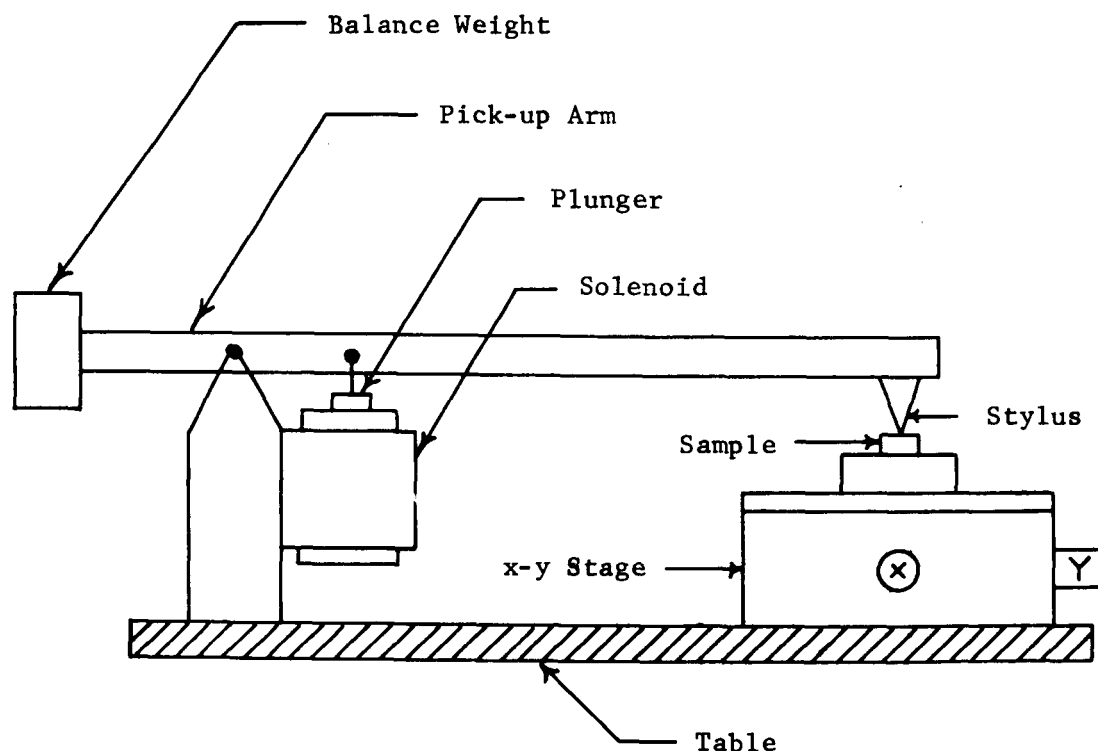


Fig. 15. Schematic of Experimental Stressing Apparatus.
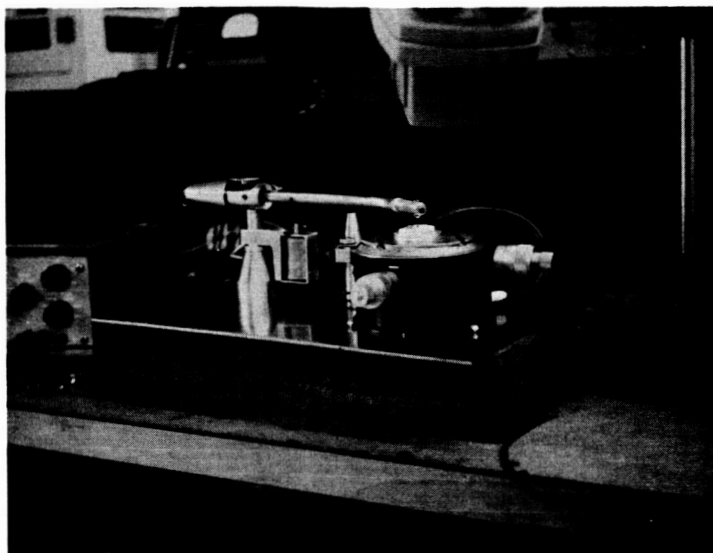
Fig. 16. Photograph of Experimental Stressing Device.

x-y stage. Due to the small size of the devices under test it was necessary to perform the alignment between the device and needle under a microscope.

Several test jigs of the type shown in Fig. 17 were constructed to perform temperature and long term stability tests. These jigs consisted of two brass blocks insulated from each other by a thin sheet of mylar. The bottom block served as a support for the sample and provides for electrical contact to one side of the device. The top block has a hole drilled through it into which a steel phonograph needle is inserted. The needle serves both as an electrical contact and as the stressing mechanism. To use this jig, one simply positions the sample to be tested beneath the needle and applies the desired force on the needle by means of a weight attached to a pin with the pin inserted in the hole of the top block and in mechanical contact with the needle.

The electrical current-voltage characteristics as a function of stress were the parameters of interest. The current range of interest covered about
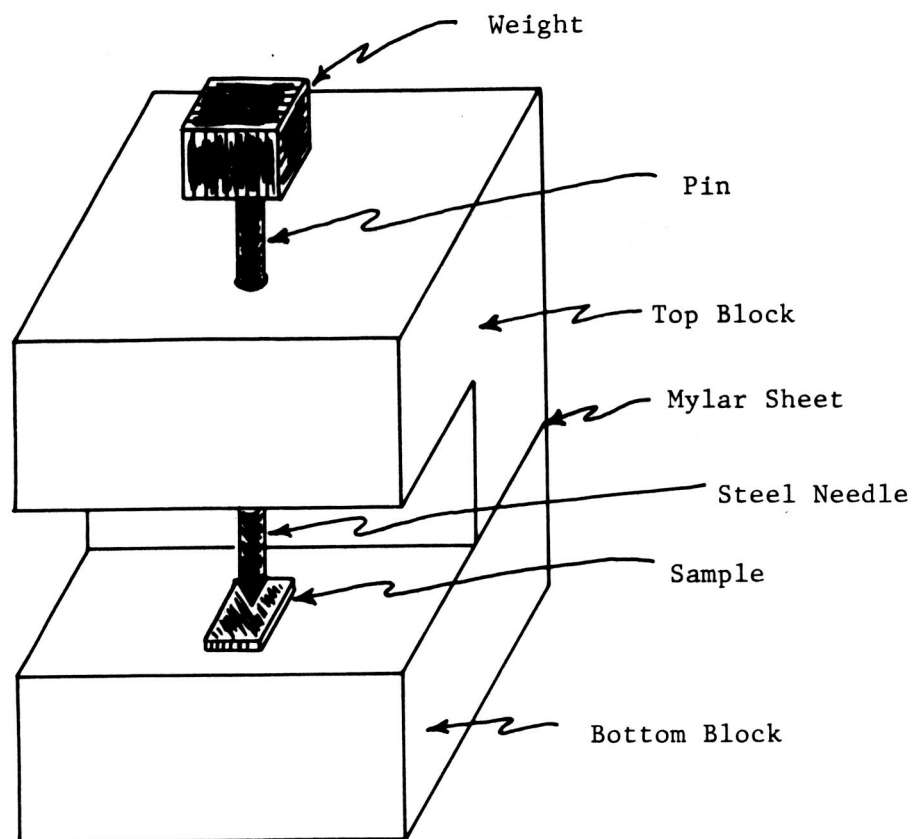
Fig. 17. Stressing Jig

four to eight orders of magnitude. Most of the data taken on the devices were recorded directly on an x-y recorder. In order to cover the large current range a circuit was constructed which allowed the x-y recorder to plot the natural logarithm of current as a function of either voltage or solenoid current. An "ideal" diode (one in which the current through the device is proportional to the exponential of the voltage across the junction) was used as the logarithm element. The diode used was the emitter-base junction of a Texas Instrument 2N1711 planar transistor in which the base and collector leads were connected together. Figures 18 and 19 are schematic drawings of the test arrangement used for measuring the I-V characteristics of diodes and transistors under stressed conditions.
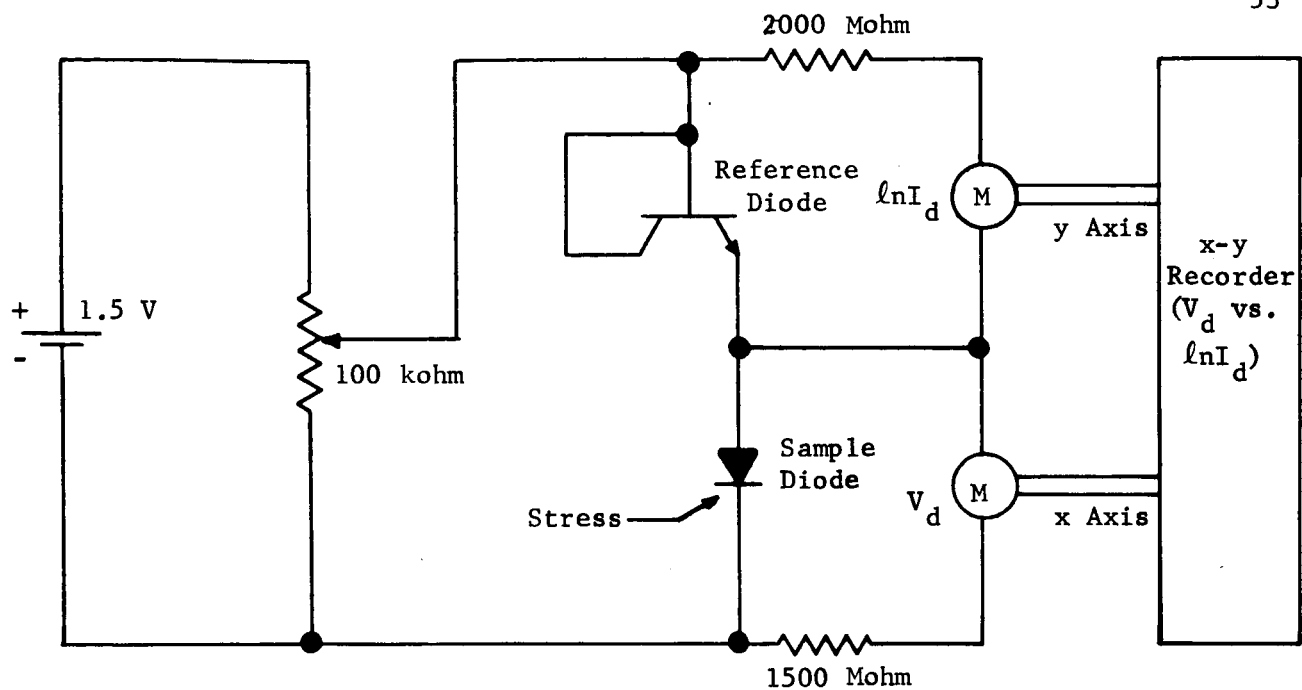
Fig. 18. Schematic of Diode Test Circuit.
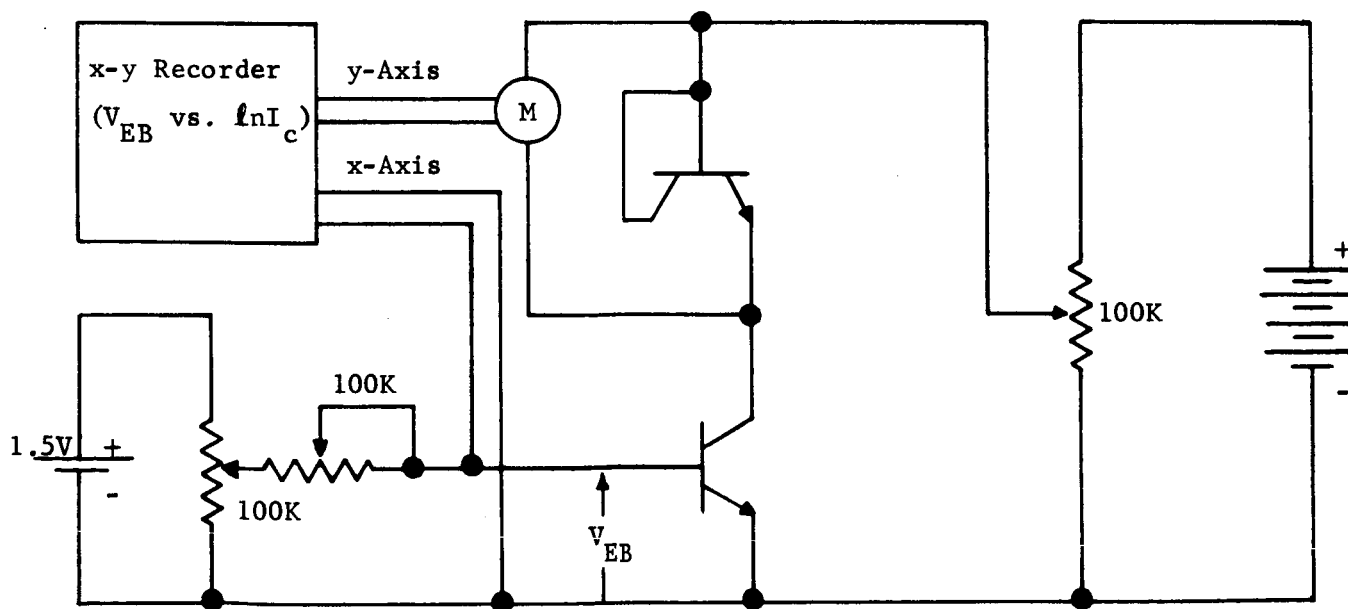


Fig. 19. Schematic of Transistor Test Circuit.

## 4.3  Mesa Diodes

Mesa diodes were studied more extensively than any other junction

device due mainly to the fact that they are easier to fabricate and are

more accessible for the application of stress.  Since mesa diodes stand up

on their base substrate, stress can be applied over their entire area by a

post which has a cross-sectional area larger than that of the diode.  This

is particularly convenient since the stress sensitivity of a diode is propor-

tional to the ratio of the diode area under stress to the total diode area,

see Eqs. (3.17) and (3.33).  Figure 20 is a sketch of the mesa structure.

In this structure, the steel post also serves to make electrical contact to

one side of the diode.
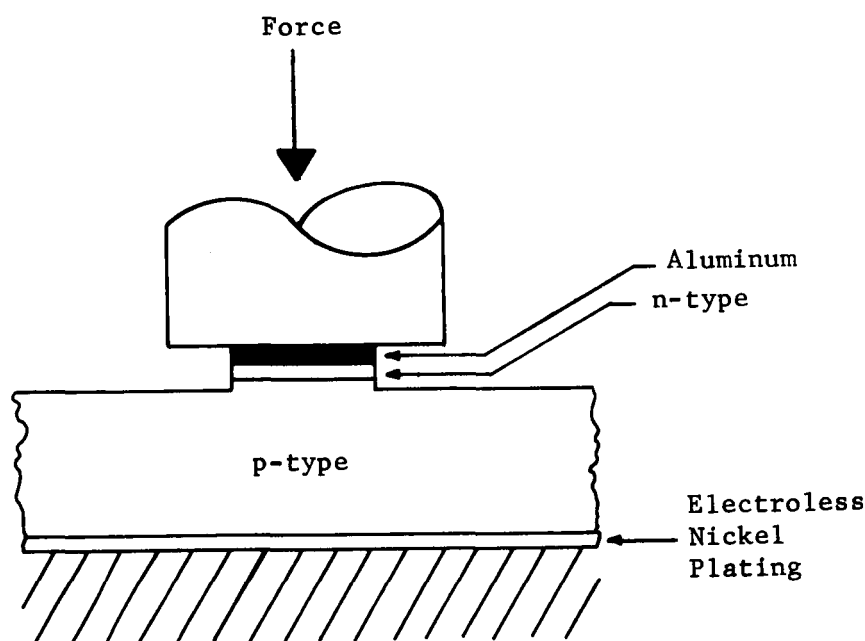
Fig. 20.  Sketch of Mesa Diode Structure.

Mesa diodes were fabricated in the laboratory by diffusion and photo-lithographic techniques. The photoengraving techniques used here were of the contact printing type and are described fully in reference [37]. The diffusion process used was the gas source type and is described in reference [38]. The following paragraphs describe in some detail the procedure used to form a p-n diode on an n-type substrate.

The silicon substrate was cleaned by the following method:

1. Boil in trichloroethylene (T.C.E).

2. Rinse in methyl alcohol.

3. Rinse in deionized water.

4. Boil in nitric acid ($HNO_3$).

5. Rinse in deionized water.

Following the cleaning the n-type sample was placed into a diffusion furnace where a p-type layer was diffused into the entire surface. The diborane gas diffusion process was used. Junction depth and surface concentration were varied so that their effects on the piezojunction phenomenon could be determined.

Following the diffusion process, the p-type layer was removed from one side of the sample (wafer) by mechanically lapping the surface. This was done to provide electrical contact with the n-region of the finished diodes. After lapping, the nonlapped side of the wafer was coated with wax and the sample was again cleaned and transferred to an electroless nickel plating bath. Thus the lapped or n-region of the wafer was coated with a nickel layer to provide a good electrical contact.

The wafer was then cleaned again and placed into a vacuum evaporator where a layer of aluminum was evaporated onto the side opposite the nickel. This provides an electrical contact to the p-region of the wafer. A

photosensitive acid resist was then placed on the aluminum side of the wafer. Following a curing cycle, the resist was exposed through a mask designed to leave unexposed 25 patterns of six small circular dots. The exposed photoresist was then removed in a developing solution leaving only the 150 dots where diodes were desired. The developed wafer was then submerged in a solution of $HNO_3$ and HF to etch away the aluminum and underlying silicon. The wafer was allowed to remain in the etch solution until it had etched through the diffused p-type layer.

The 6 diodes in each pattern were of three different sizes. Typical diameters of the diodes were 90, 45, and 28 microns. A photomicrograph of a 6 diode pattern as described above is shown in Fig. 21.
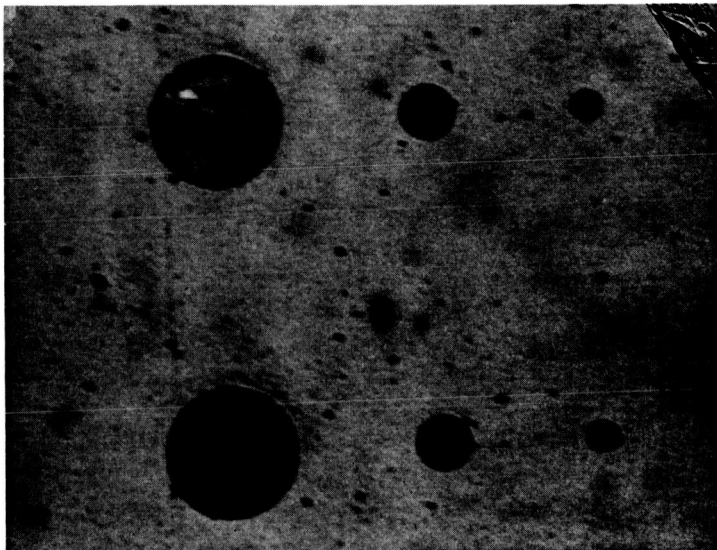


Fig. 21. Photomicrograph of a 6 Mesa Diode Pattern.

In the forward biased case the current is exponentially related to voltage. When plotted on linear graph paper the I-V characteristics have a knee at approximately 0.6 volts at current levels in the μamp range.

When subjected to large mechanical stresses the knee is shifted in voltage toward the origin. This can be seen from the theory discussed in Sect. 3 above. Assuming first that the diode current is "ideal" and second that the stress is large enough ($\sim 10^{10}$ dynes/cm$^2$) so that $\overline{\gamma}_\nu(e)_\alpha\ e^{\frac{qc}{kT}}$, then from Eq. (3.19) which applies for mesa diodes

$$I = I_o\ e^{\frac{qc\sigma}{kT}}\ (e^{\frac{qV}{kT}} - 1) \ , \tag{4.1}$$

where c is a constant depending on the stress orientation. For forward voltages greater than a few hundredths of a volt such that $e^{\frac{q}{kT}} \gg 1$, Eq. (4.1) becomes

$$I = I_o\ e^{\frac{q}{kT}(V + c\sigma)} \ . \tag{4.2}$$

As can be seen from Eq. (4.2), the voltage at which the knee occurs as seen on a linear plot of I vs V will be shifted toward the origin. The same procedure can be used to show that the same type of behavior is observed for generation-recombination currents as a function of forward voltage.

Figure 22 shows the I-V characterization of an experimental mesa diode as displayed on a transistor curve tracer. The horizontal scale is 0.2 volts/cm and the vertical scale is 0.01 ma/cm. The curve to the far right of the figure is that obtained for zero applied stress. The curves beginning with the second from the right and progressing left are those obtained by applying an increasing stress to the diode.

A typical set of forward biased current-voltage characteristics of a mesa diode for different stress levels is shown in Fig. 23. The diode was fabricated on a 0.01 ohm-cm crystal with a (100) orientation. The junction depth was approximately 3 microns and the diode diameter was 42 microns.
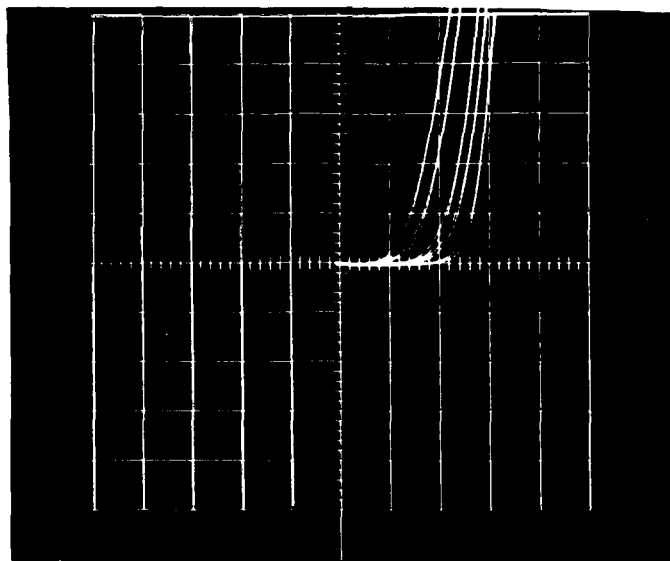
Fig. 22. Forward I-V Characterization of a Mesa Diode Under Stress.

There are several significant features of the characteristics as shown in Fig. 23. For voltages below 0.3 volts, all of the curves have the same slope, qV/kT, where kT $\simeq$ 0.026 ev at room temperature. For low stress levels and voltages above 0.3 volts the slopes of the curves are functions of stress. In the latter case where the stress is zero, the slope is approximately qV/2kT. As stress is increased the slopes again approach a constant of qV/kT.

The change in the slope of the I-V characteristics can result from either the "ideal" or generation-recombination components or both. Considering first the "ideal" component, the slope of the I-V characteristics can change from qV/kT at low injection levels to a qV/2kT at high injection levels. The voltage at which high injection takes place for 0.01 ohm-cm crystal resistivity is approximately 0.65 volts. Since the slope change in the diode occurs at approximately 0.3 volts, high injection can be eliminated. Turning to the generation-recombination component of current, it is seen from Eq. (3.25)
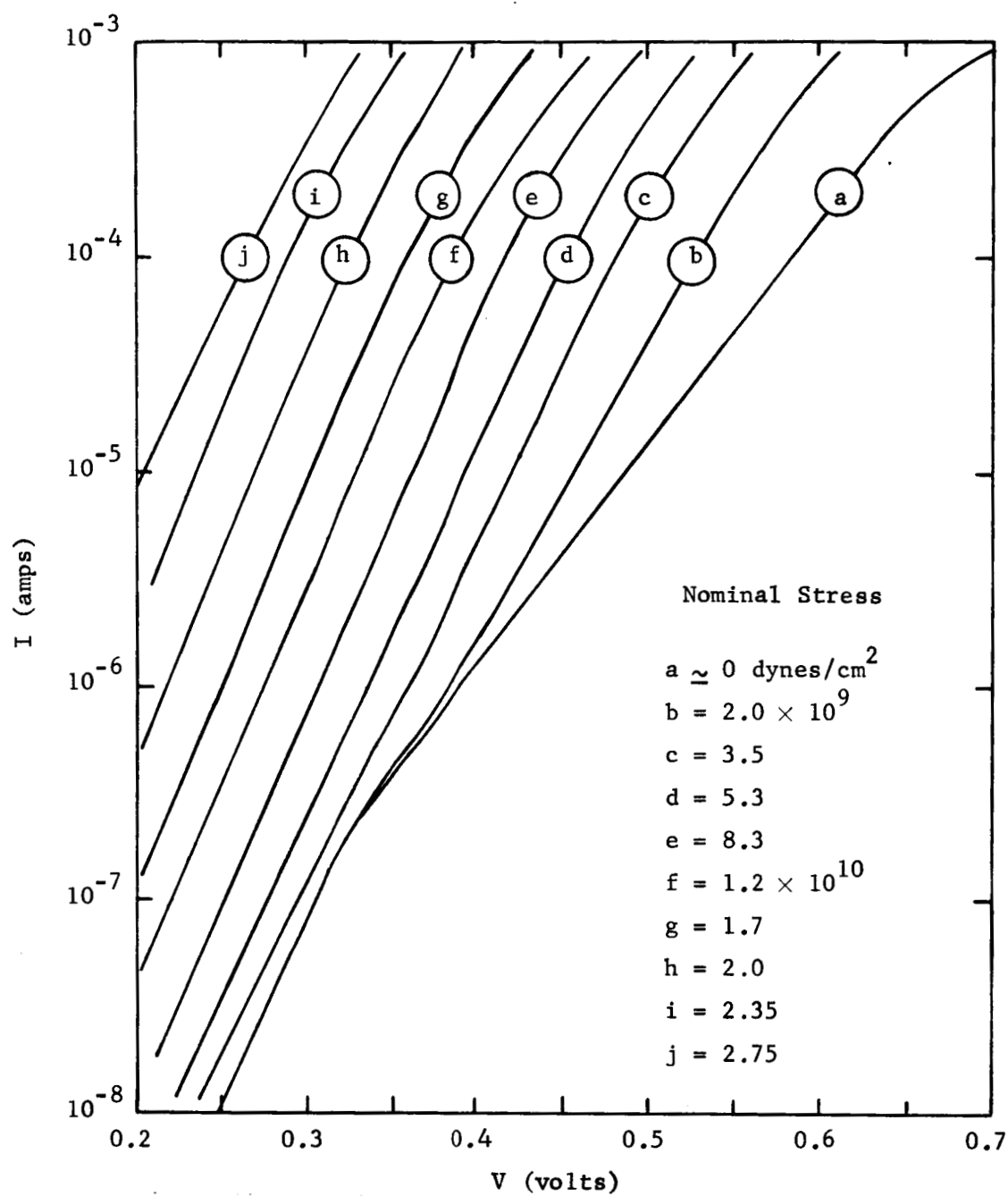
Fig. 23.  Current vs Forward Voltage Characteristics of a Mesa Diode Under
          Various Stress Levels.

(neglecting the change in junction width as a function of voltage) that the $I_U$ can have a slope change from qV/kT at low voltages to a qV/2kT at higher voltages.

From Chapter III it is seen that the "ideal" component increases in magnitude in proportion to $\gamma_\nu(e)$ with increasing stress and that the generation-recombination component increases in proportion to $\sqrt{\gamma_\nu(e)}$ with increasing stress. Stress then has the effect of amplifying the "ideal" component more than the generation-recombination component. In light of the above discussion, if the unstressed current is essentially generation-recombination current, then as stress is increased the "ideal" component becomes increasingly important and at higher stress levels the "ideal" component dominates the total current. The "ideal" component has the qV/kT slope. The theory is therefore consistent with the experimental data.

Current-stress characteristics of the diode just discussed for several voltages are shown in Fig. 24. These curves are essentially $\gamma_\nu(e)$ since $\gamma_\nu(e) \simeq I(e)/I(o)$. Comparing the data in Fig. 24 with that shown in Fig. 9 for $\gamma_\nu(e)$ which was calculated theoretically it is seen that there is excellent agreement. A large number of samples were tested in order to determine experimentally the parameter $\gamma_\nu(e)$ as a function of stress. Contrary to the above good agreement with the theoretical dependence of $\gamma_\nu(e)$ on stress, it was found experimentally that $\gamma_\nu(e)$ had the same general characteristics as the theoretical but in most cases the magnitude of the force required to give the same value of $\gamma_\nu(e)$ was lower than the theoretical value and varied from sample to sample. This variation was found with samples made on the same crystal at the same time and stressed with the same needle. Figure 25 shows an example of this variation for two diodes on the same crystal.

The large variation in $\gamma_\nu(e)$ as a function of stress is expected since $\gamma_\nu(e)$ is exponentially related to stress. The nominal stress in the present
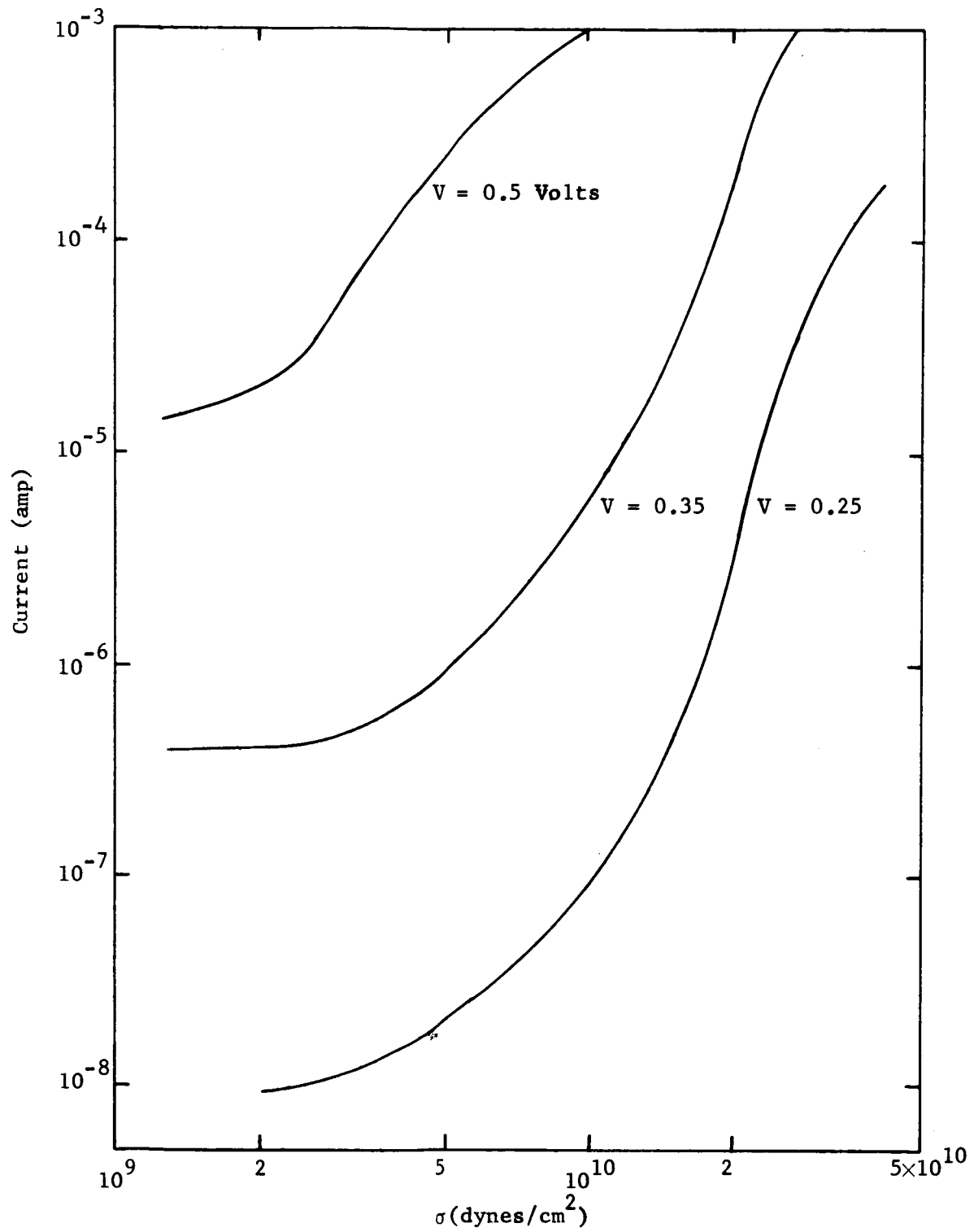
Fig. 24. Current as a Function of Stress at Several Voltage Levels for the Diode Characteristics Shown in Fig. 23.
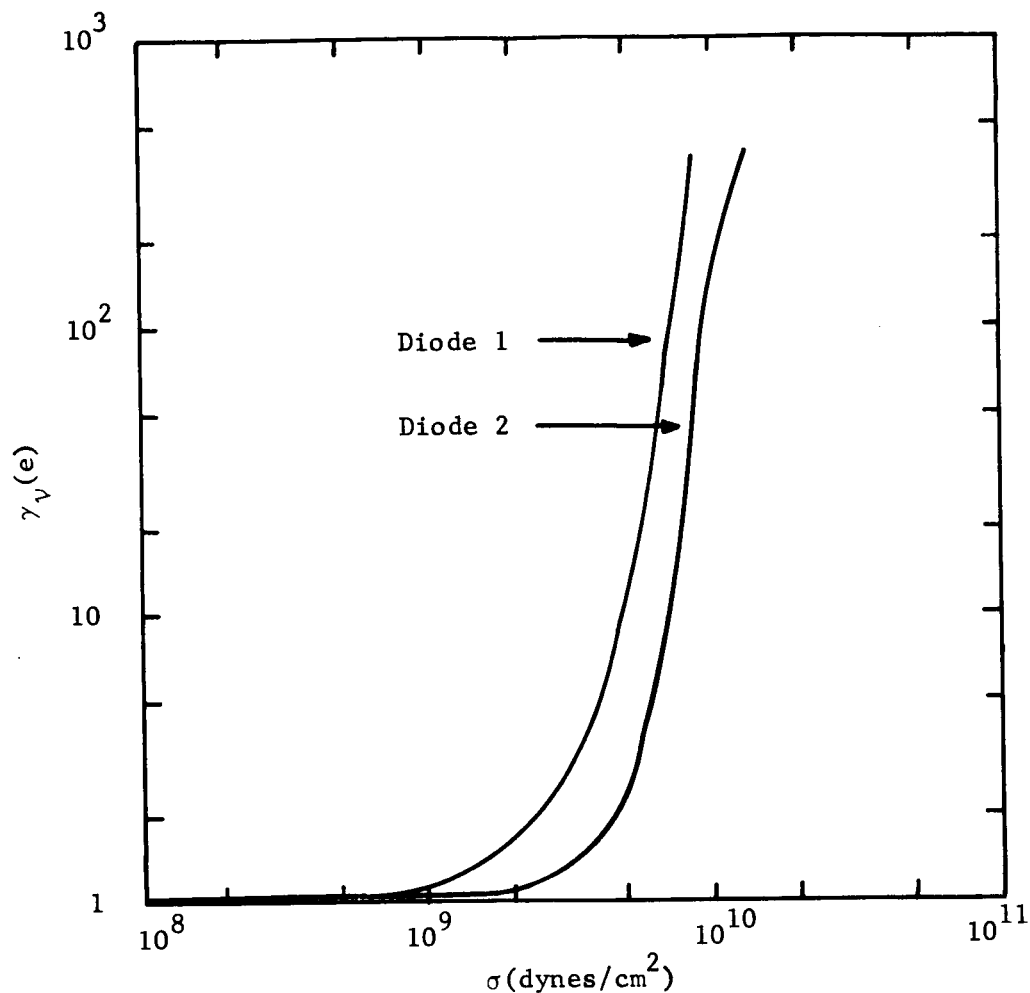
Fig. 25.  $\gamma_\nu(e)$ as a Function of Stress for Two Diodes Made on the ⸱⸱⸱e (111) Wafer.

experiments was calculated from measurements of force and diode diameter.  The data indicate that the actual or effective stress varies from sample to sample. This probably results from variations in the area over which the force acts. This is believed to result from a non-uniform or rough surface on the diode and from the non-linearity of $\gamma_\nu(e)$ vs strain.  Since the junctions are very close to the surface of the diode (0.5 - 10 microns), a rough diode surface would cause uneven stress to be set up in the junction.

A series of tests was made to determine the effect of crystal orientation on the phenomenon. Figure 26 is a typical plot of $\gamma_\nu$(e) for three different crystal orientations. As shown in the figure, the orientations in order of decreasing sensitivity are <100>, <110>, and <111>. This is in agreement with the theory as shown in Fig. 9 in which the theoretical values of $\gamma_\nu$(e) are plotted.
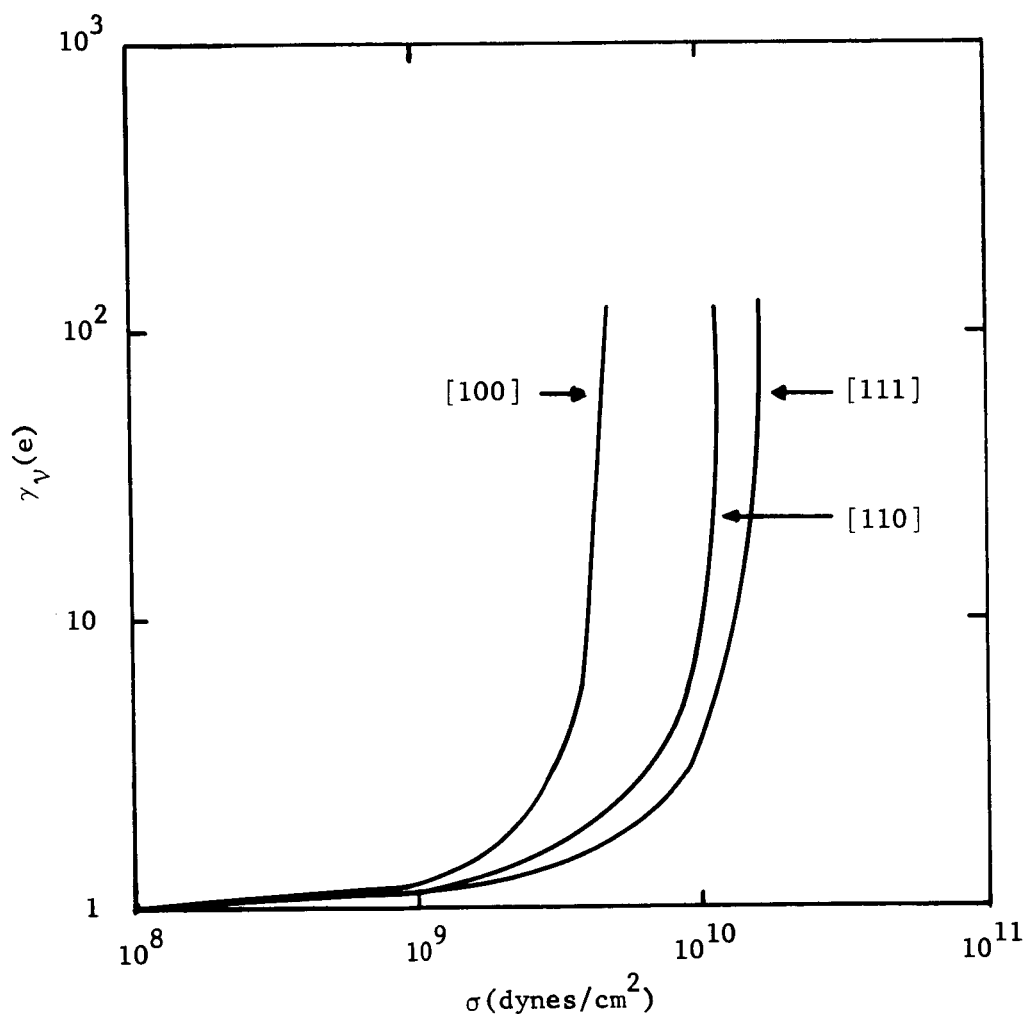


Fig. 26. $\gamma_\nu$(e) as a Function of Stress for a [100], [110], and [111] Uniaxial Stress.

Experiments were performed to determine the effect of junction depth on the phenomenon. It was found that the shallower the junction depth the more sensitive the devices are to stress. Figures 27 and 28 show the I-V characteristics at several stress levels for 0.6 and a 2.5 micron junction respectively. There are two reasons why stress sensitivity increases with decreasing junction depth. First, for shallow junctions the "ideal" current component is larger than it is for deep junctions. This is due to larger minority carrier density gradients (see Eq. (E.2) and E.3) of Appendix E). The closer the junction is to the surface the steeper the gradient for the minority carriers near the surface. The second reason for increased stress sensitivity is that the closer the junction is to the surface the more nonuniform the stress is in the junction due to surface roughness of the diode.

The observations described above on mesa diodes have been limited to the forward biased characteristics. The reverse biased characteristics of these diodes are very complicated and difficult to compare to the existing diode theories. Figure 29 is a plot of the I-V characteristics under reverse bias conditions. As can be seen from the figure, the characteristics cannot be correlated with either the ideal currents (I = constant) or th $_{\text{bu}}$ generation-recombination current ($I \propto V^{1/3}$ or $V^{1/2}$). This means that the major contribution to the diode current in the reverse biased case is probably either surface channels or surface generation-recombination currents. The fact that such currents are present is not surprising since the mesa structure has no junction passivation. A theoretical analysis of these currents is beyond the scope of this work. However, a thorough treatment of diode characteristics in general is given in Ref. [39].
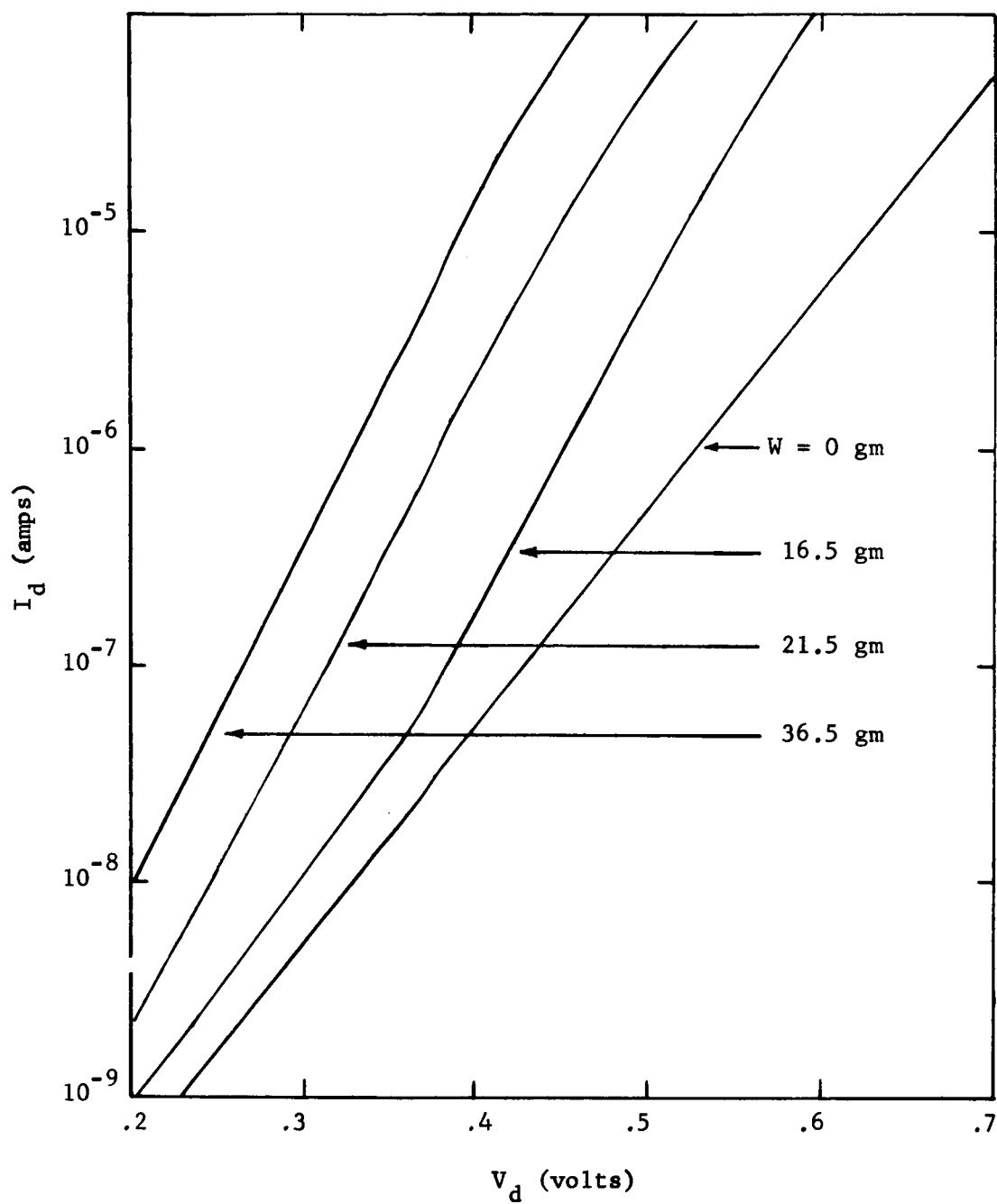
Fig. 27. I-V Characteristics of a Mesa Diode Under Varying Stress Conditions. The Junction Depth Was 0.6μ and the Orientation Was a (111) Plane.
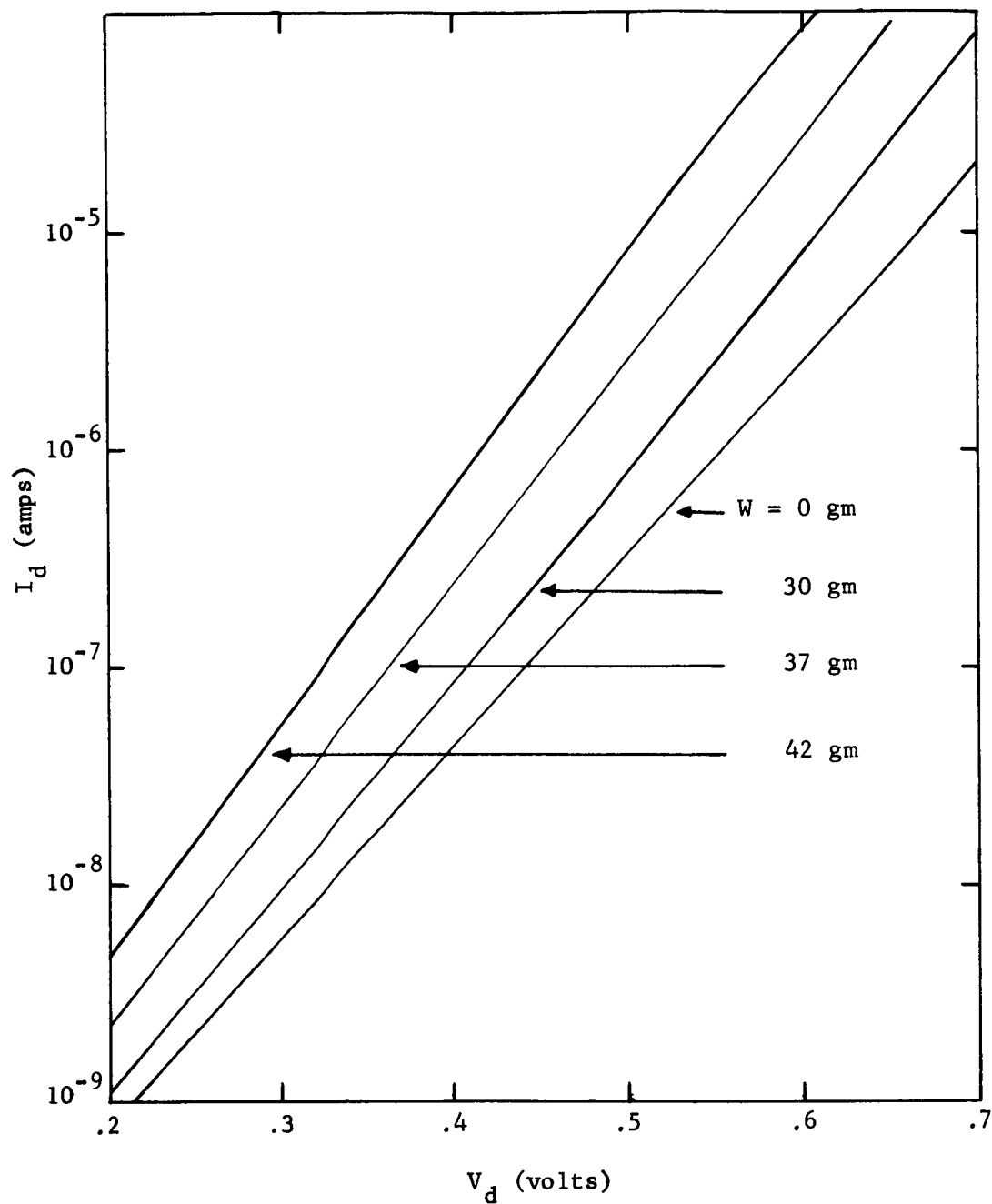
Fig. 28. I-V Characteristics of a Mesa Diode Under Varying Stress Conditions. The Junction Depth was 2.5µ and the Orientation Was a (111) Plane.
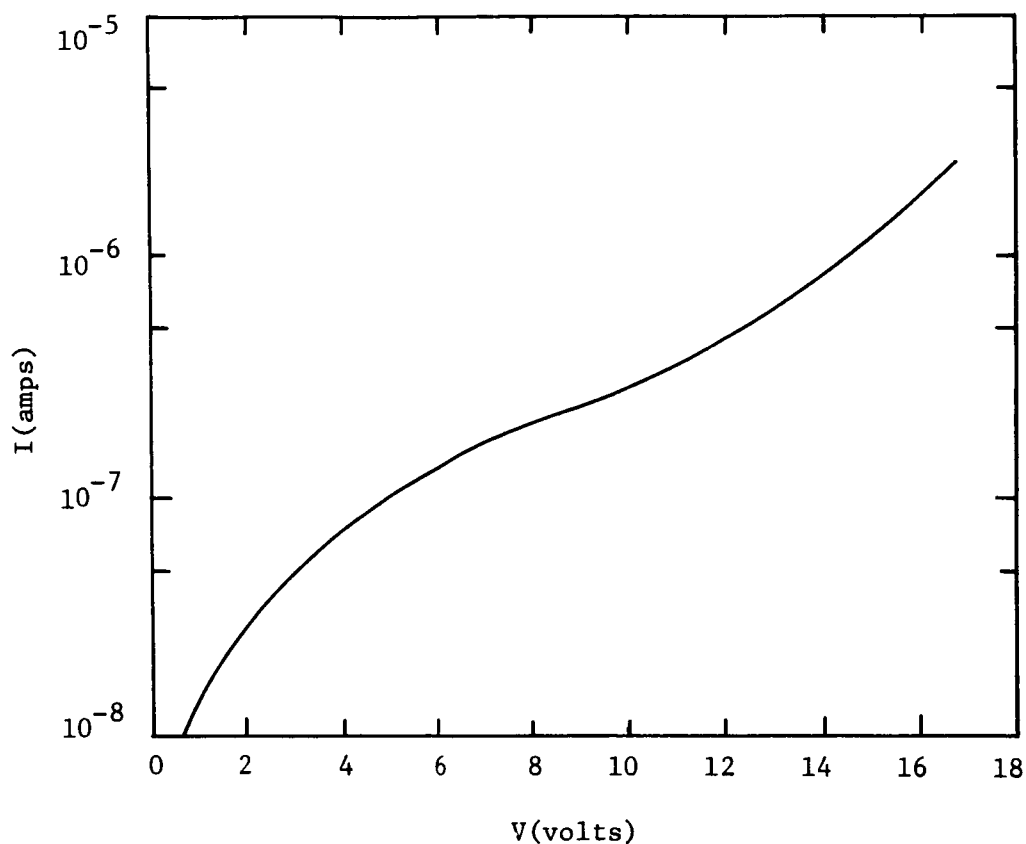
Fig. 29.  Reverse I-V Characteristics of a Mesa Diode.

Measurements on the reverse characteristics of the mesa diodes observed here have shown that there is little if any effect on the characteristics due to mechanical stress.  Due to the physical geometry of the mesa structure, one would not expect stress applied to the top of the mesa to have much effect on surface channels that might be present on the periphery near and below the junction.  Even if the currents are of the surface generation-recombination type there is no present means of describing the effect of mechanical stress on these currents.  In fact, as discussed in Sect. 3, one cannot describe the reverse characteristics of bulk type generation-recombination currents since there are no present data on the effect of stress on the trap levels which cause these currents.

The fact that mesa diodes, in particular those discussed above, are
not stress sensitive in the reverse direction does not eliminate their appli-
cation as a transducer. It simply requires that they be operated in a forward
biased condition. This may or may not be detrimental depending on the output
levels and impedances required in a particular application. Also, mesa diodes
can be fabricated with passivated junctions which could possibly eliminate
this objection.

Mesa diodes were tested to determine the effect of temperature on the
piezojunction phenomenon. Figures 30, 31 and 32 are plots of current vs forward
voltage for stress levels of 0, 8.1 $\chi$ $10^9$ dynes/cm$^2$ and 1 $\chi$ $10^{10}$ dynes/cm$^2$
respectively. As can be seen in the figures, the forward current is a strong
function of the diode temperature and the higher the stress level the less
temperature effects the characteristics. Figure 33 shows these same charac-
teristics plotted as a function of temperature for a constant voltage of
0.3 volts. The slope of $\ln I$ vs T decreases with increasing stress as predicted
in Sect. 3.

In terms of transducer applications it is unfortunate that the stress
sensitivity of diode current is a function of temperature. Analyzing the data
in Figs. 30 - 33 reveals that it would be very difficult to temperature
compensate a diode if current is used as a measure of stress. At temperatures
on the order of $40^{\circ}C$ to $60^{\circ}C$ the current sensitivity is approximately constant
which means that over this limited range one could probably temperature compen-
sate.

The diode voltage dependence on stress at a constant current is a
more attractive parameter to work with in temperature compensation. Voltage,
however, is a linear function of stress while current is an exponential function,
hence less sensitivity will be obtained. From Eq. (4.2) it is seen that at high
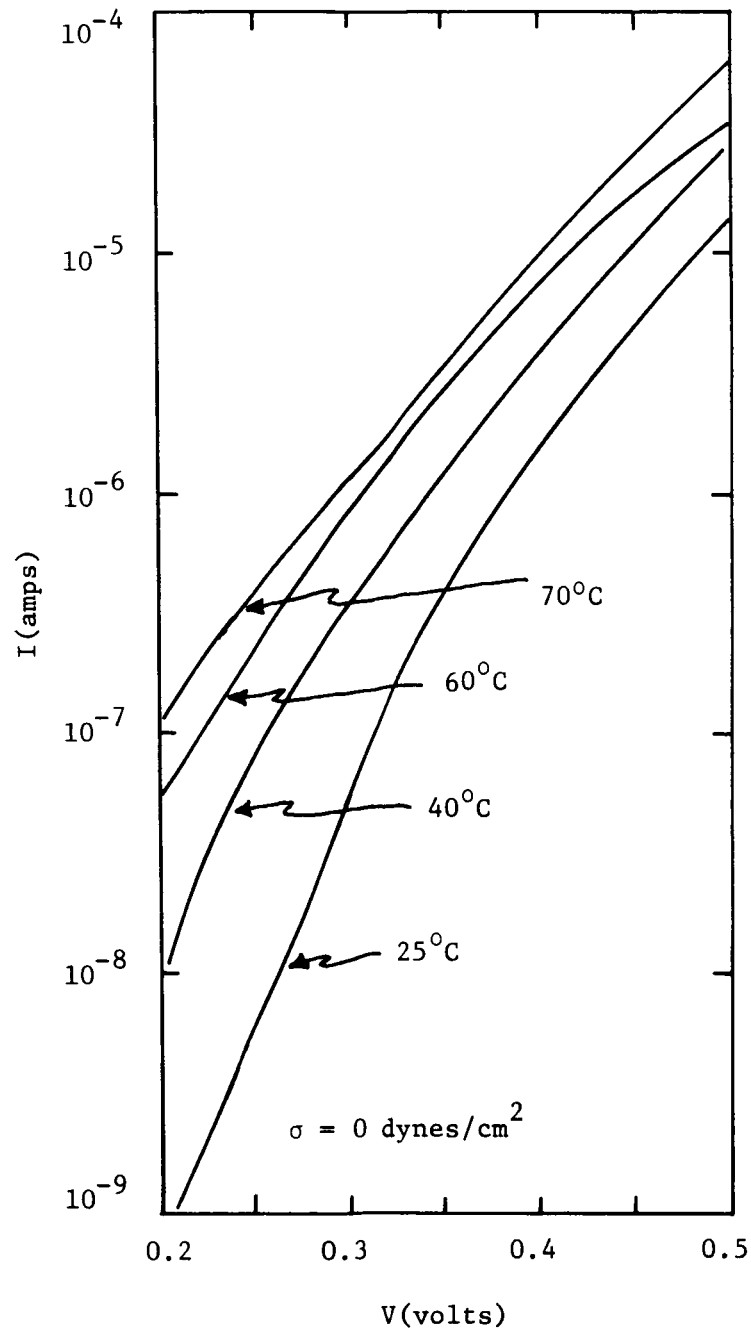
Fig. 30. I-V Characteristics as a Function of Temperature under no Load Condition.
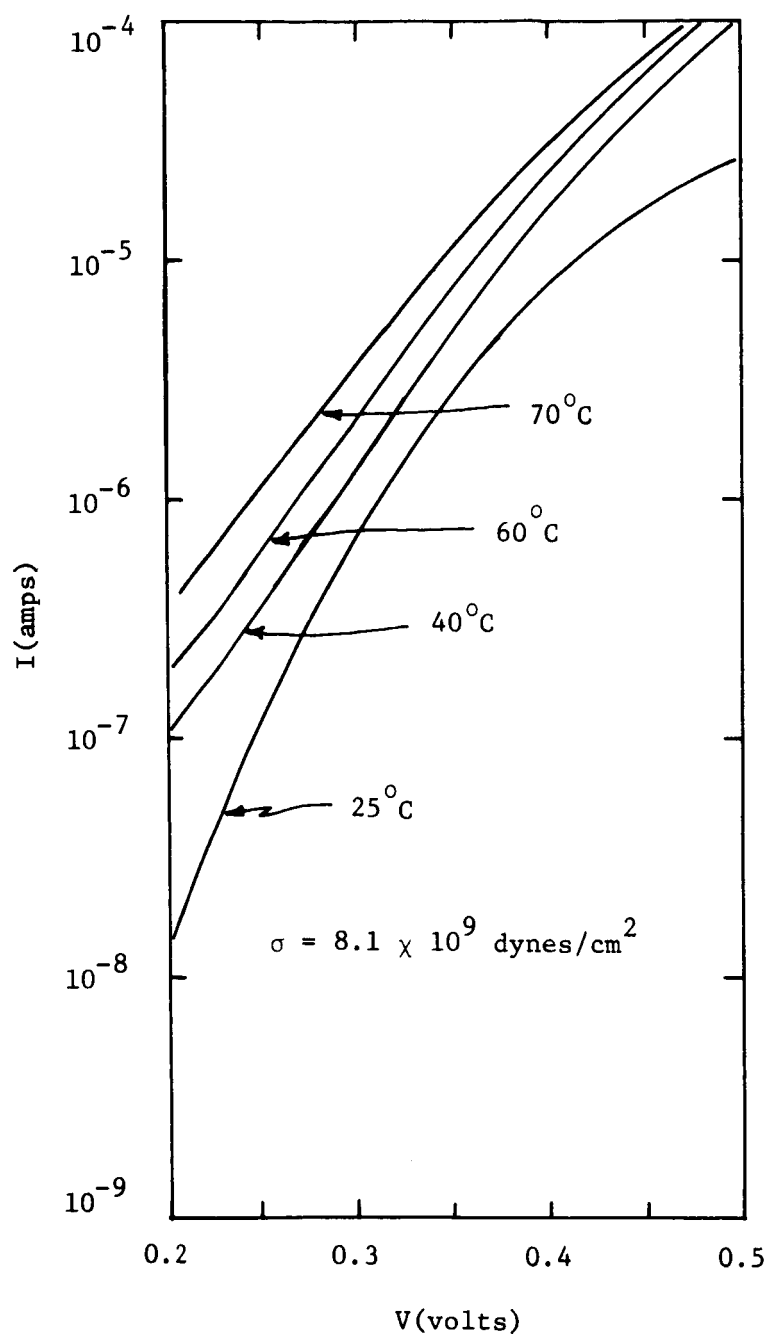
Fig. 31. I-V Characteristics as a Function of Temperature for a Load of
8.1 × 10$^{10}$ dynes/cm$^2$.
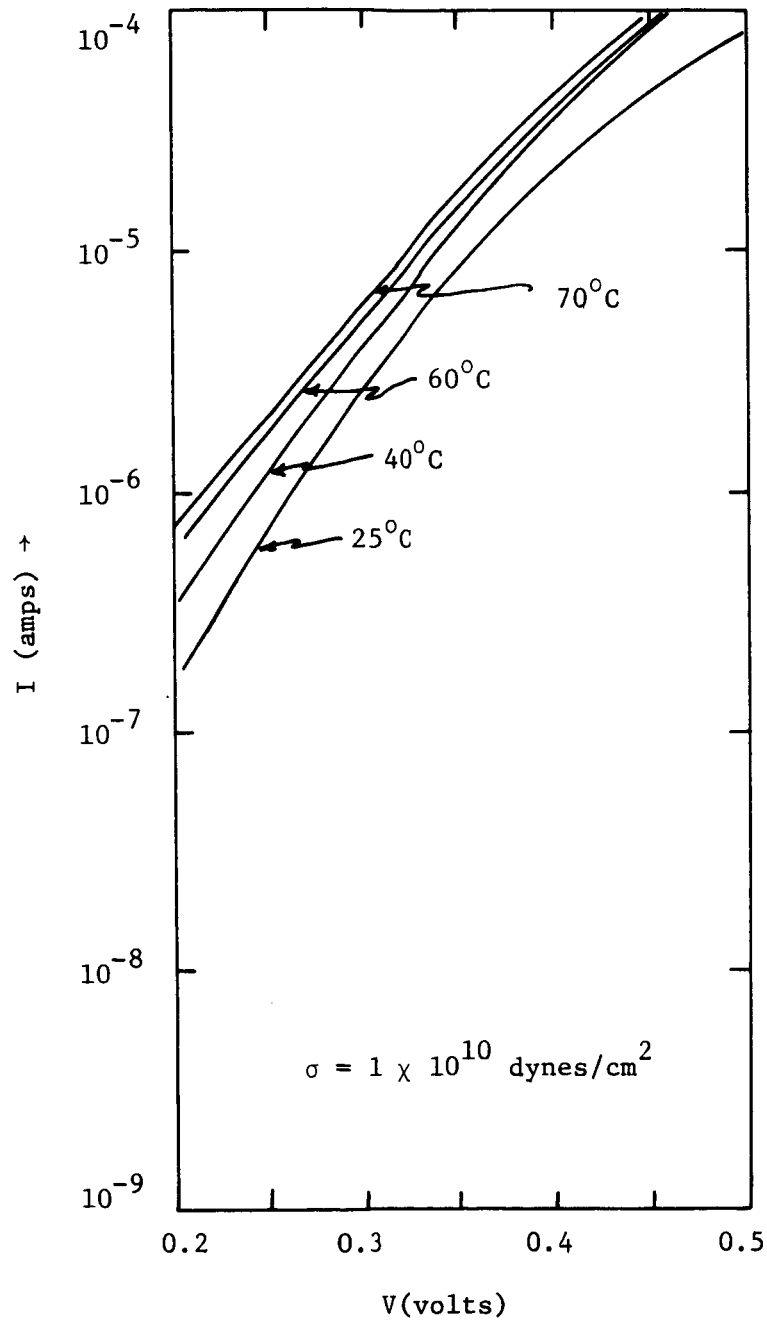
Fig. 32. I-V Characteristics as a Function of Temperature for a Load of $1 \times 10^{10}$ dynes/cm$^2$.
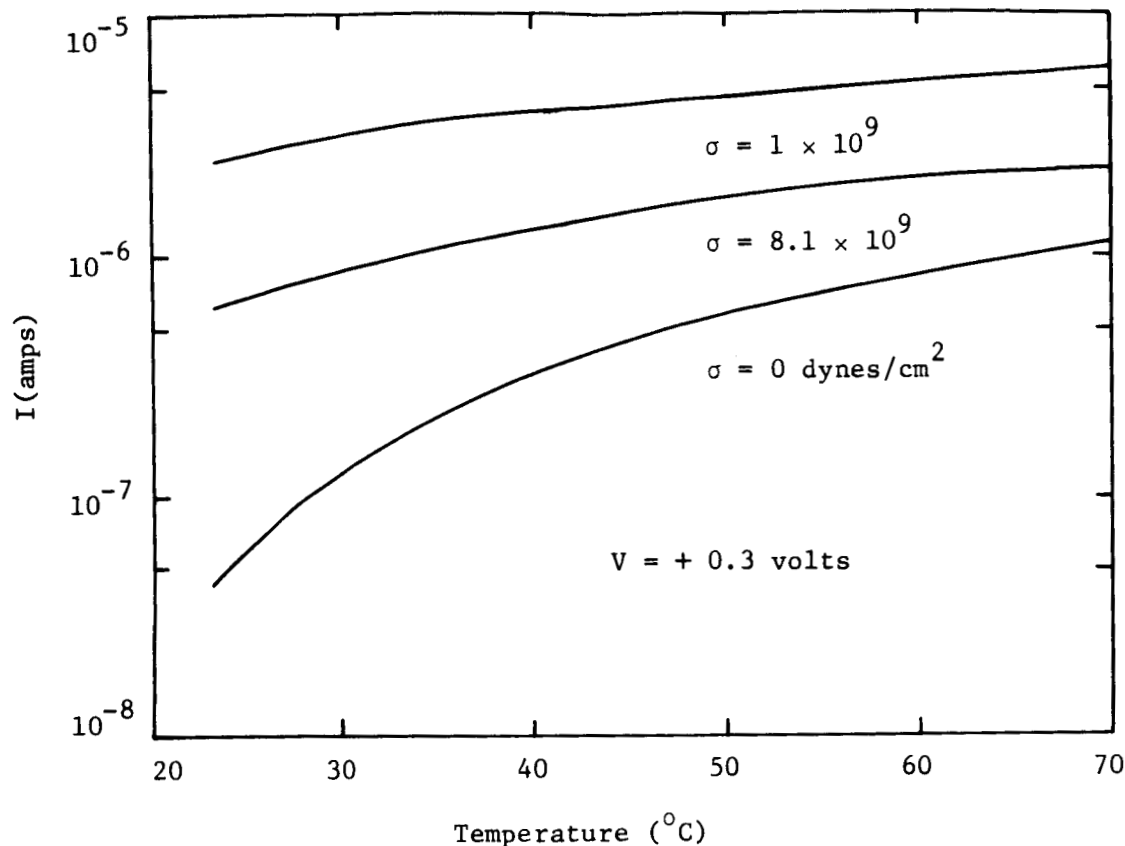
Fig. 33. Current as a Function of Temperature for the Three Stress Levels Shown in Figures 30, 31 and 32.

stress levels the voltage and stress can be combined into the same exponential term, i.e.

$$I = I_o(T) \, e^{\frac{q(V+c\sigma)}{kT}} \, . \tag{4.2}$$

One way to temperature compensate is to use a bridge of the type shown in Fig. 34 in which two identical diodes are used with one being stressed. In this circuit, if the two diodes are identical with the exception of stress, and $R_1$ and $R_2$ are much larger than the resistance of the diodes so that the current through each diode is constant, the voltmeter should read a voltage which is $c\sigma$ in Eq. (4.2) and be independent of temperature. That is, a
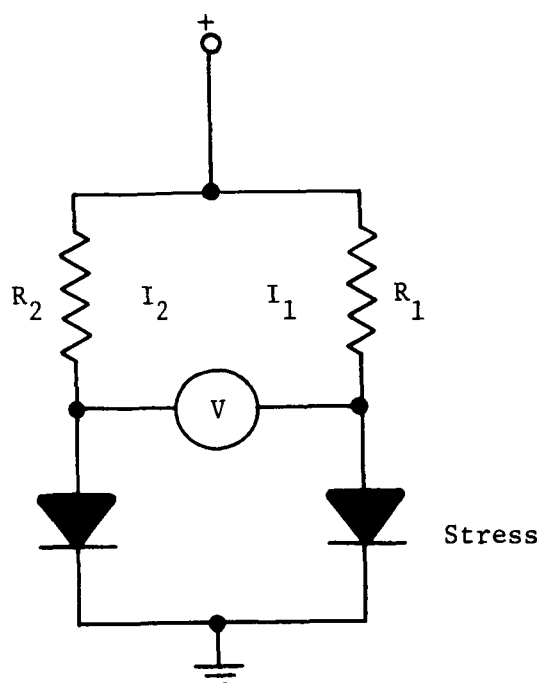
Fig. 34. Bridge Circuit for Eliminating Temperature in Diode Sensors.

linear output which is independent of temperature. Preliminary tests have

shown that this circuit may work, however more tests are required before any

definite conclusion can be drawn. The big problem is to obtain two identical

diodes. In some applications it may be desirable to hold temperature constant.

In order to determine the stability of the piezojunction phenomenon with

time, a mesa diode was placed in one of the brass test jigs with the diode

under a constant load and allowed to remain there for several months. The

I-V characteristics were monitored daily to determine if there was any change.

It was found, that within the accuracy of the measuring equipment, there was

no change. Based on this test, a transducer using the present phenomenon should

be very stable with time while the device is operated under static conditions.

No tests have been run to determine the long term effects of dynamic loading.

Based on the present theory and experiments, it is concluded that mesa diodes can be used as a mechanical stress transducer. It should be pointed out that, contrary to the present work, mesa diodes characteristics are, in general, susceptible to variations with environment and time. This will depend largely on the fabrication process and operating environment.

## 4.4  Planar Diodes

Planar type silicon diodes have been fabricated in the laboratory and tested to determine the effect of stress on their characteristics. Standard photoengraving and diffusion techniques were used to fabricate these diodes. Figure 35 is a sketch of the structure. The planar diodes as fabricated here
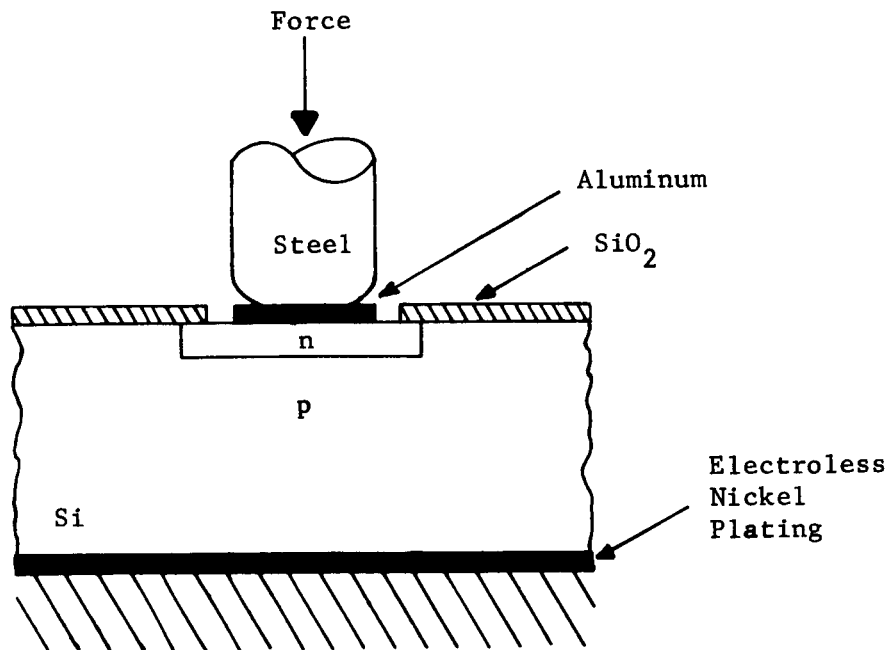
Fig. 35.  Schematic of Planar Diode Structure.

had a silicon dioxide glass layer over the region where the p-n junction

comes to the surface of the device. This, of course, passivates the junction, and hence, the diodes were found to be relatively stable with time and environment.

Figure 36 is a typical plot of diode current versus forward voltage for several stress levels. The sample crystal was 1 ohm-cm with a (111) orientation. As was the case for mesa diodes, the slopes of the curves for planars are stress sensitive at low stress levels. It appears that the total diode current in this case is almost all "ideal" as evidenced by the slope of approximately $qV/kT$ and the many orders of magnitude of current over which the slope is constant. The effect of spreading resistance can be seen by the turnover of the curves at the higher voltage levels. Figure 37 shows the current vs stress characteristics for several voltage levels. The characteristics are essentially the same as those for mesa diodes.

Figure 38 shows the effect of stress on the reverse biased characteristics of a planar diode. Unlike the mesa diodes, the reverse current is stress dependent in planar devices. This means that planar devices have less surface currents and more bulk generation-recombination and "ideal" currents. In planar diodes the reverse current can easily be used as a measure of the diode stress.

## 4.5 Transistors

A variety of commercial and laboratory silicon transistors have been tested with the aim of exhibiting the many facets of the piezojunction phenomenon in the two-junction devices. All transistors used in these experiments have been of the planar diffused type. The laboratory transistors were fabricated by using standard photoengraving techniques and a gas source diffusion
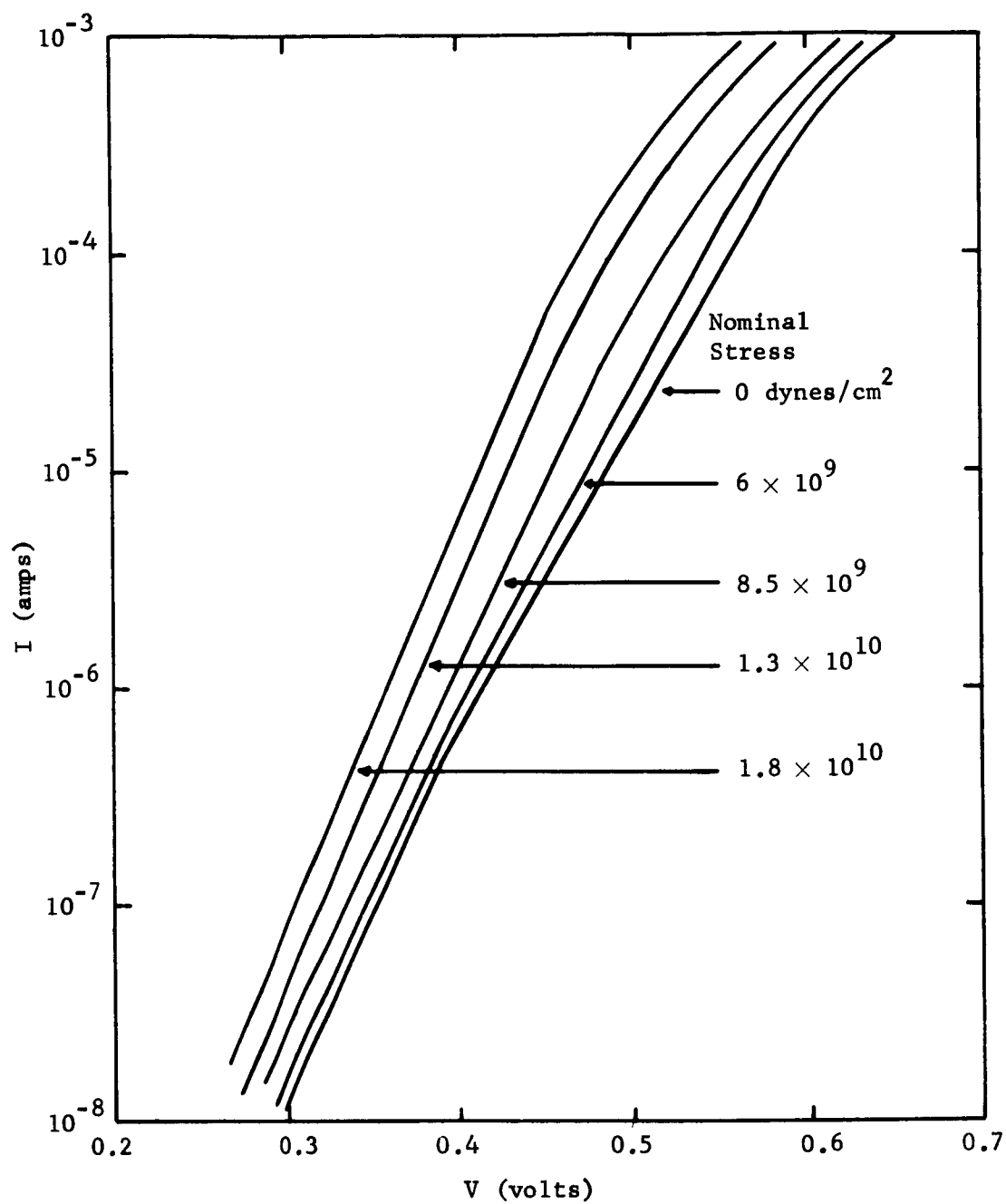
Fig. 36 .  I-V Characteristics of a Planar Diode Under Several Nominal Stress
Conditions.
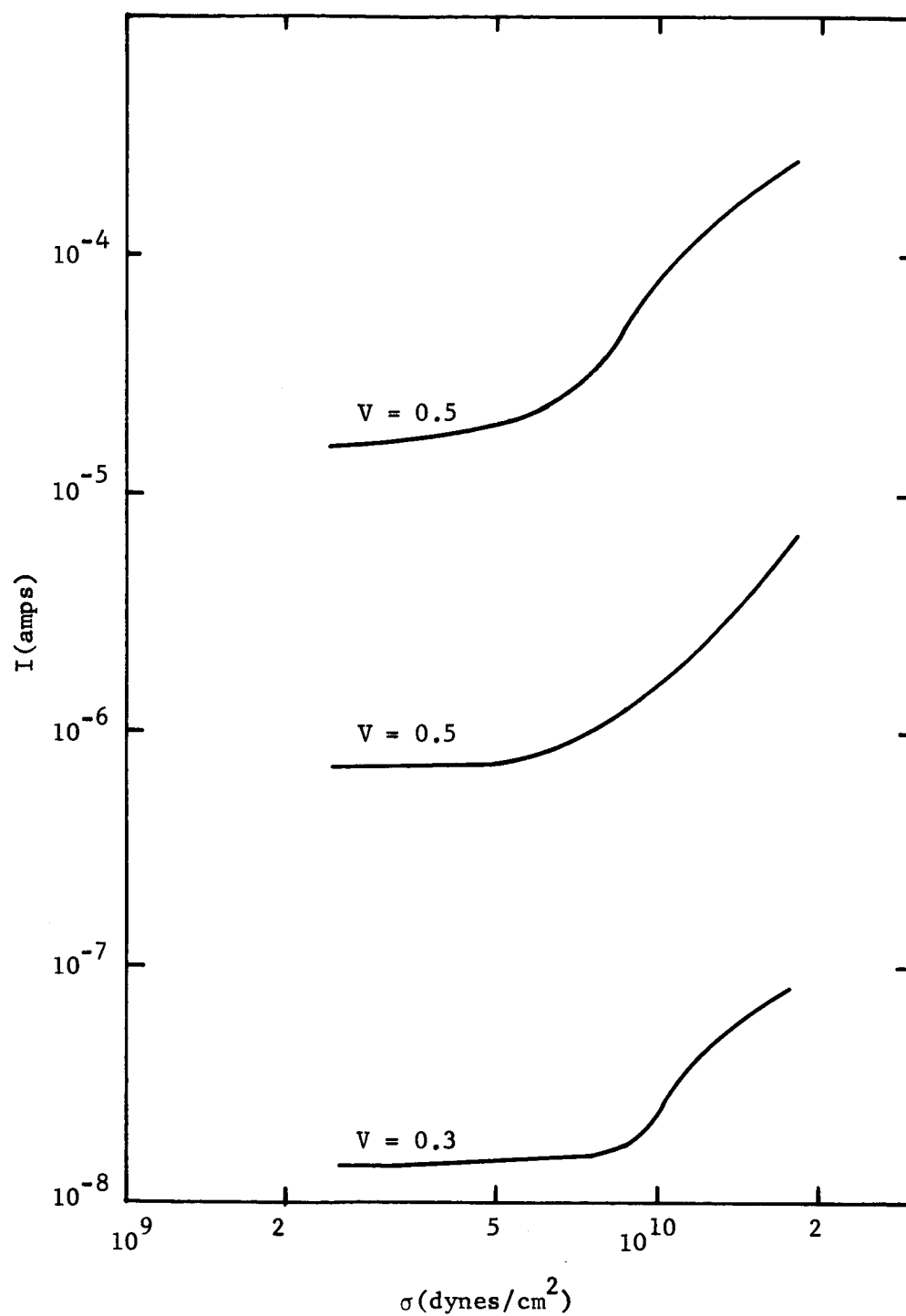
Fig. 37. Current vs Nominal Stress for a (111) Plane Planar Diode for Several Voltage Levels.
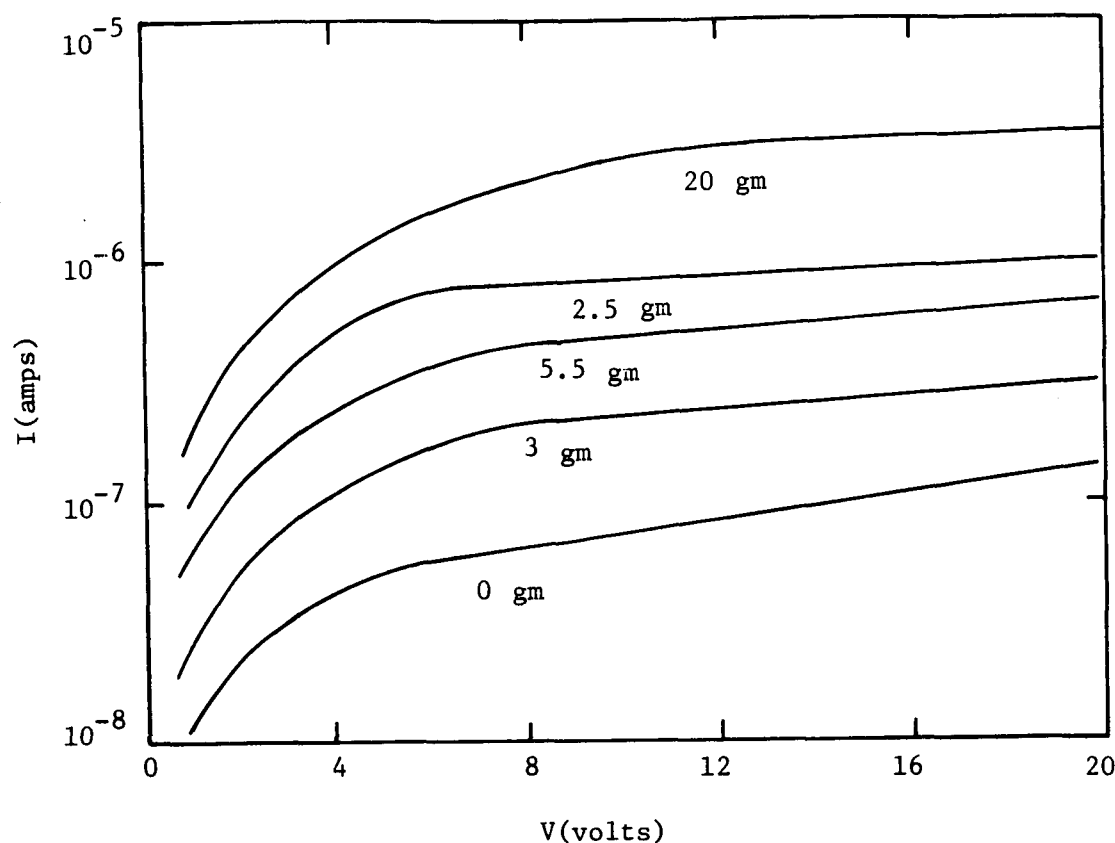
Fig. 38. Reverse I-V Characteristics of a Planar Diode Under Stress.

furnace. Figure 39 is a sketch of a typical planar transistor showing the several locations at which stress was applied to the device by small indentor points. In all locations, the stress or strain field must be at or near a junction in order to alter the electrical characteristics. Indentor points made of steel, sapphire, and diamond have been used in the experiments. Of these, diamond is harder than silicon and consequently produced more anisotropic stress than steel or sapphire.

The most interesting results have been obtained on transistors in which stress was applied either directly on the emitter-base junction or near the emitter-base junction on the emitter side. The latter can be done in two ways. The first method is to place the indentor very close to the junction where the junction comes to the surface. The second is to apply
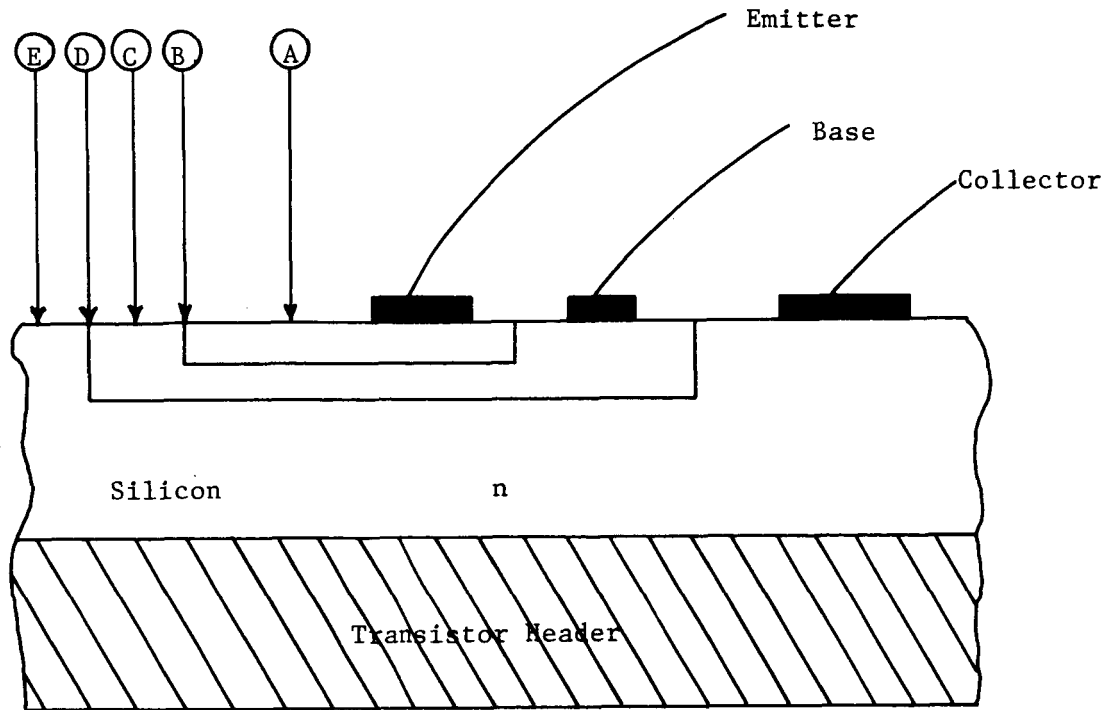
Fig. 39.  Cross section of a Planar Transistor Showing Points of Stress
Application.

the indentor anywhere in the emitter region.  The stress produced by a

spherical indentor point is attenuated very fast with distance underneath

the indentor.  When the indentor is placed on the emitter there is some

stress on the base side of the junction; however, the stress on the emitter

side of the junction is larger and essentially dominates the piezojunction

effect.

As discussed in Sect. 3, stress induced changes in the electrical

characteristics are dependent on the particular mode of transistor opertaion

and the location of the mechanical stress field in the device.  The fact that

different modes of operation give different stress dependent characteristics

is illustrated in Fig. 40 which shows photographs made on a transistor

curve tracer.  This figure depicts the effect of stress on the collector

current vs collector voltage of a 2N3053 transistor operated in both the

Common Emitter
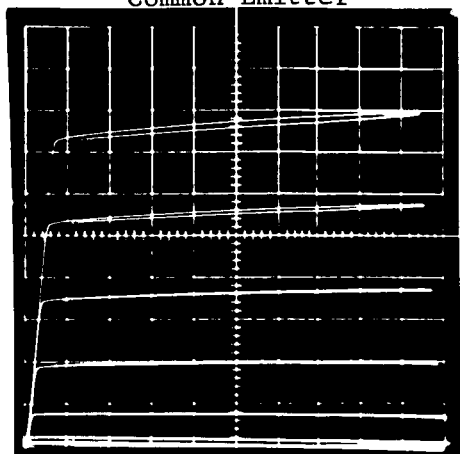
Common Base

(a)   F = 0 gm
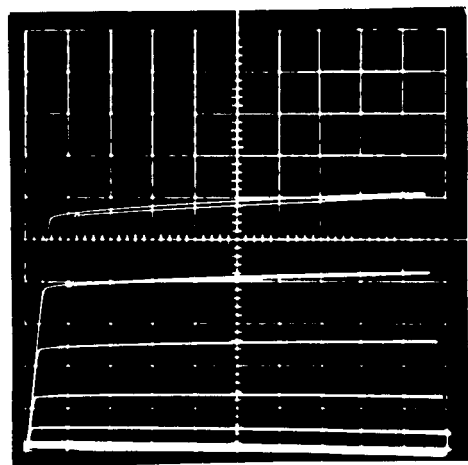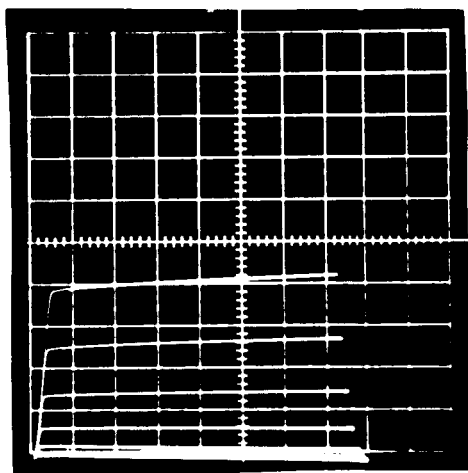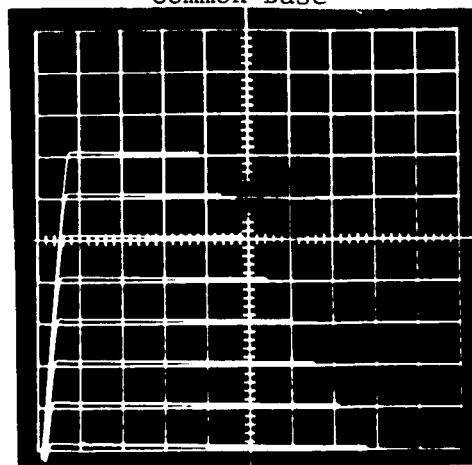
(d)   F = 0  gm
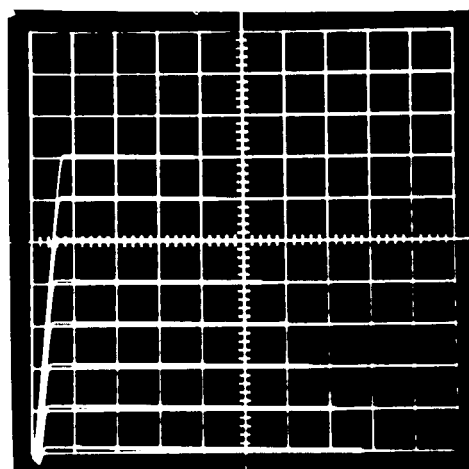
(b)   F = 75 gm

(e)   F = 75  gm
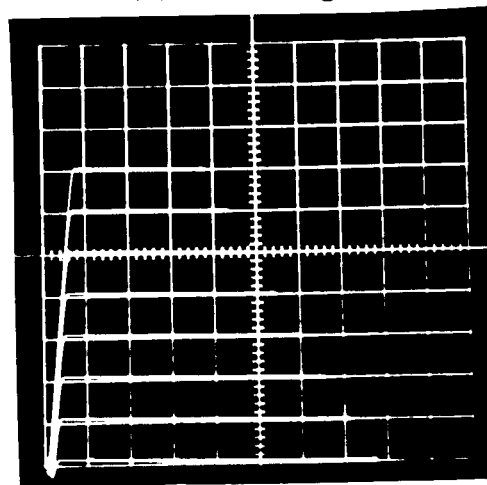
(c)   F = 115 gm

(f)   F = 115 gm

Fig. 40.   $I_c$ vs $V_c$ for a 2N3053 Under Stress.

common emitter mode and common base mode. In Fig. 40 (a), (b), and (c) are

common emitter characteristics with a base current drive of 0.05 ma/step while

(d), (e), and (f) are common base characteristics with an emitter current

drive of 2 ma/step. The vertical scale is 2 ma/cm and the horizontal scale

is 2 volts/cm. Stress was applied by a 3 mil steel needle to the emitter

region of the device (position A of Fig. 39). Characteristics (a) and (d)

were obtained with zero stress applied, (b) and (e) with 75 grams and (c) and

(f) with 115 grams.

From Fig. 40, it is seen that when the transistor is operated in the

common emitter mode ((a), (b), (c)) the gain or $\beta$ of the device is drastically

reduced by stress. In the common base mode the gain or $\alpha$ is reduced only

very slightly as seen in (d), (e), and (f). This is expected however since

$$\beta = \frac{1}{1 - \alpha} \; . \tag{4.3}$$

If $\alpha$ is near unity then small decreases induced by stress will be reflected

by large changes in $\beta$.

The effect of stress on the collector current with either emitter

current constant or base current constant for a 2N1958 n-p-n transistor is

shown in Fig. 41. The stress was applied to the emitter by a 0.7 mil

sapphire needle. As shown in Fig. 41 the collector current is more sensitive

to stress with base current held constant than it is with emitter current

held constant. By comparing Fig. 41 with Fig. 14, which was calculated

theoretically, it is seen that the experimental results are in good qualita-

tive agreement with the theory.

Figure 42 is a plot of $I_c$ as a function of $V_{eb}$ for several stress

levels in a laboratory n-p-n planar transistor. In this case the stress was
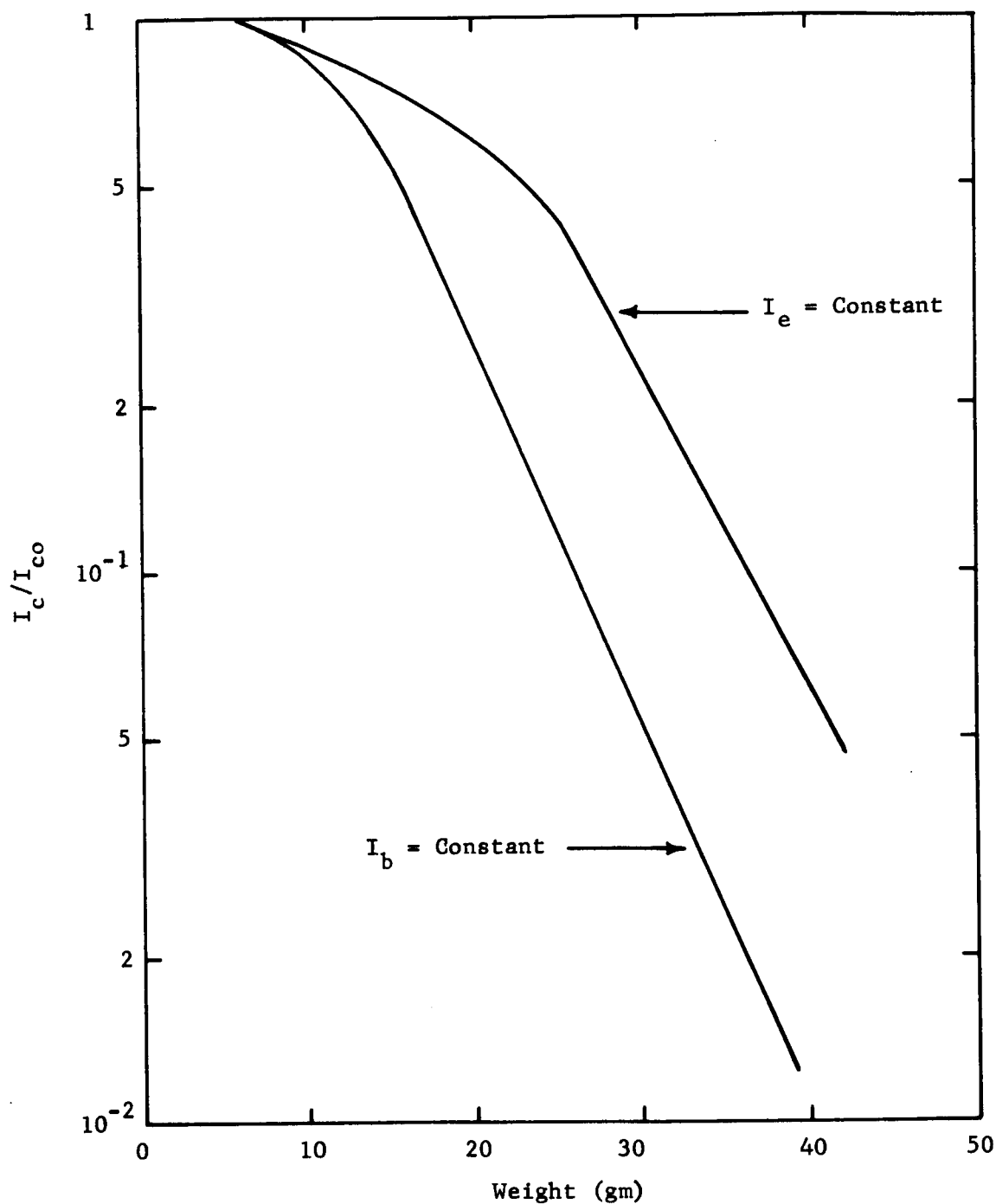
Fig. 41.  Ratio of Stressed to Unstressed Collector Current of a 2N1958
n-p-n Transistor with Base Current Held Constant and with
Emitter Current Held Constant.
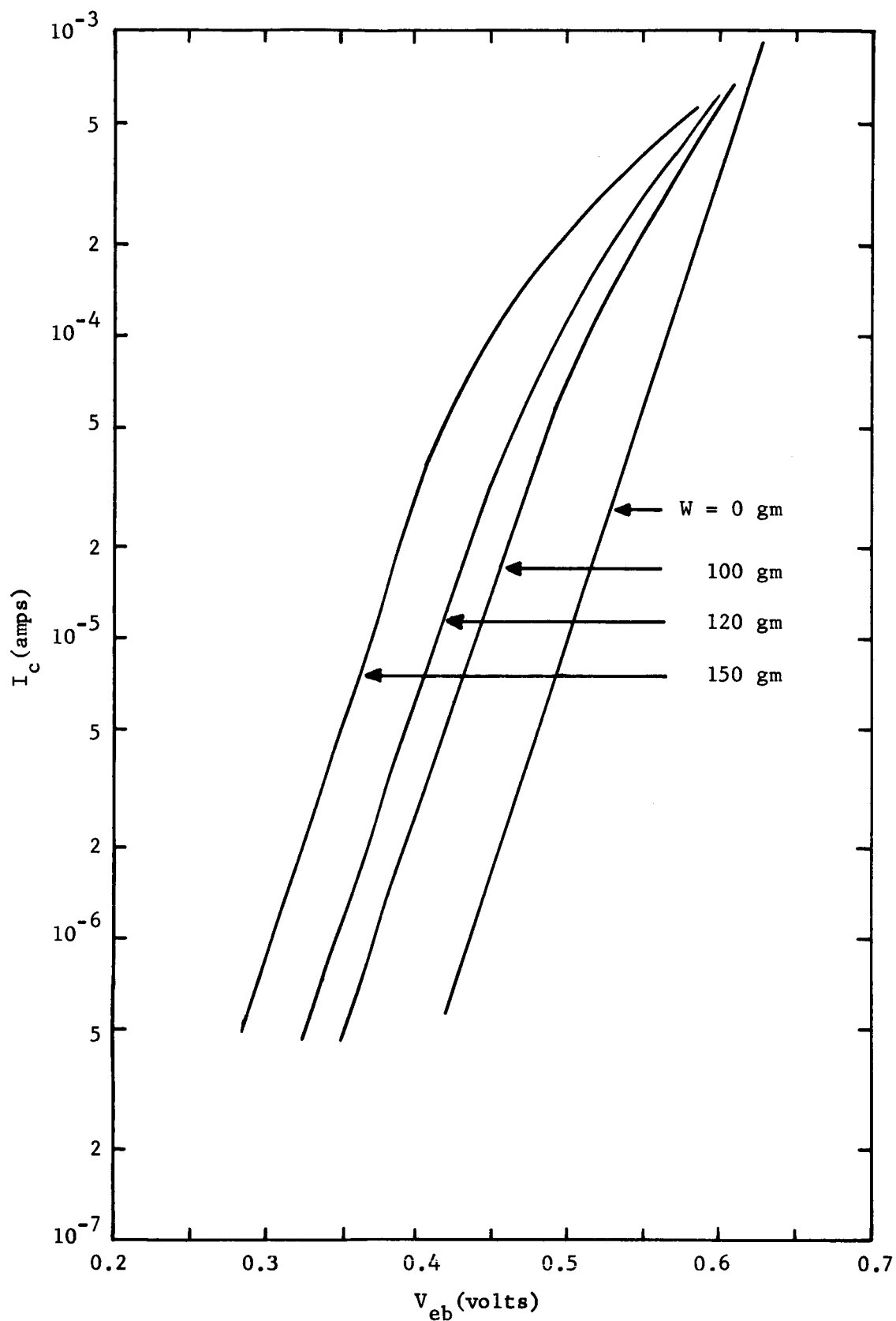
Fig. 42. Collector Current as a Function of Emitter Base Voltage for
Constant Base Current and Several Stress Levels in an n-p-n
Silicon Transistor Stressed in the Emitter Area with a Steel
Needle.

applied to the emitter with a 3 mil steel needle. The effect of stress on the base current with collector current and emitter-base voltage held constant is shown in Fig. 43. The transistor was a 2N2102 n-p-n device with stress applied by a 0.7 mil sapphire needle. The base current of an n-p-n 2N2102 transistor as a function of emitter-base voltage for several levels is shown in Fig. 44. In this case the emitter-base junction was stressed where it comes to the surface with a 3 mil sapphire needle. This particular device had an oxide over the junction and the stress was applied through the oxide.
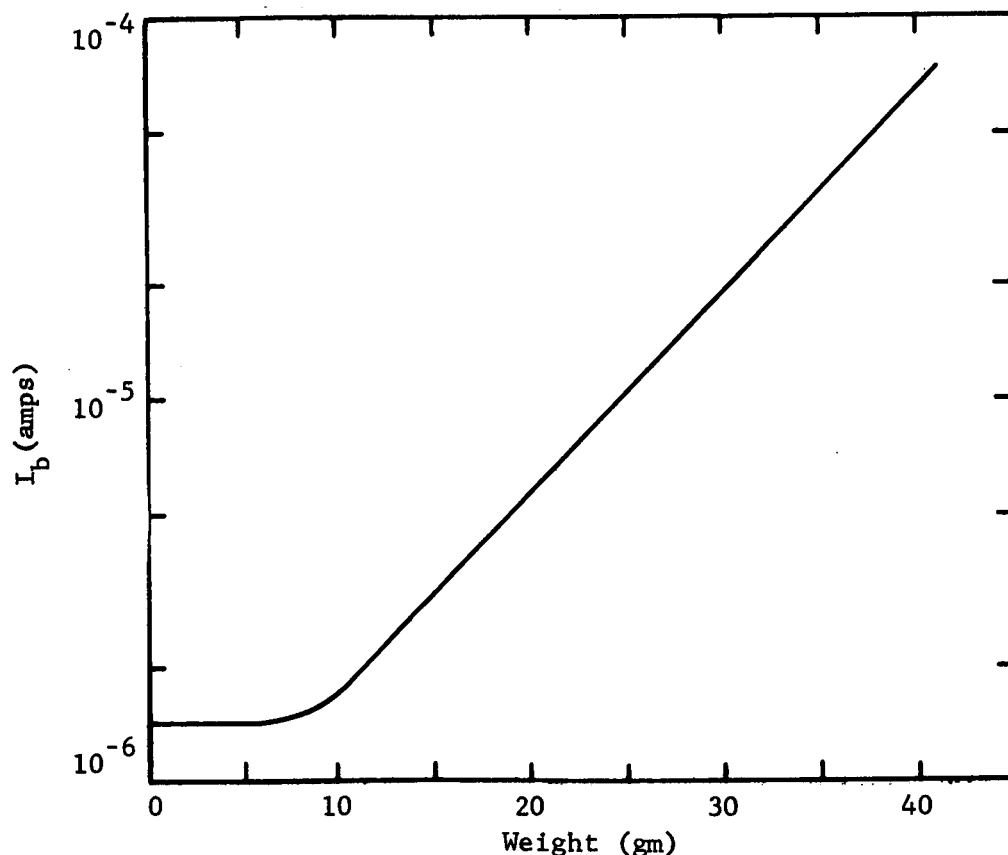


Fig. 43. Base Current as a Function of Stress with the Emitter-Base Voltage Held Constant for an n-p-n 2N2102 Transistor Stressed in the Emitter Area with a Sapphire Needle.
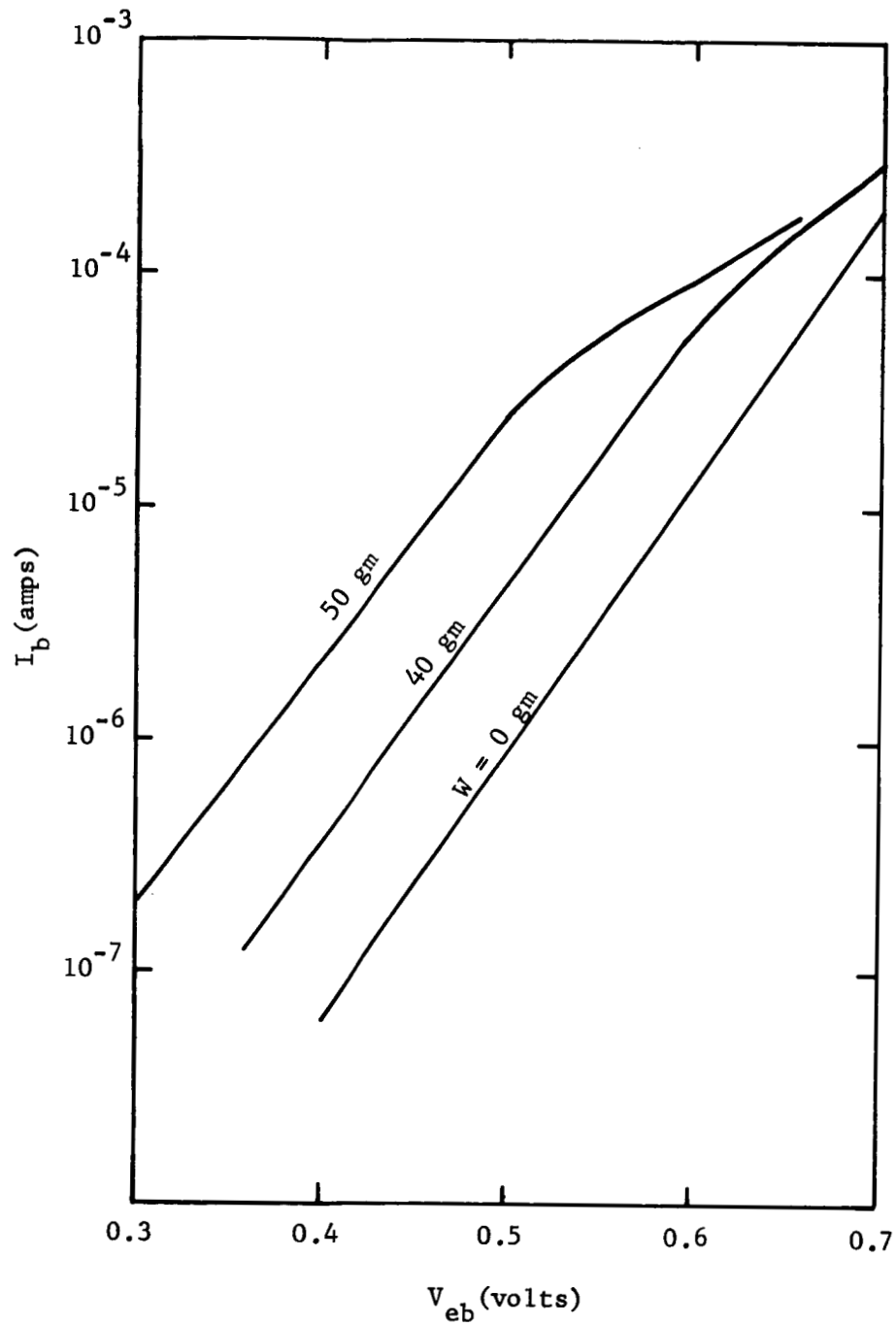
Fig. 44. Base Current as a Function of Emitter Base Voltage for Three Stress Levels in an n-p-n Silicon Transistor. The transistor was stressed on the emitter base junction with a 3 mil Sapphire needle.

Stress applied on the base side of the emitter-base junction has a much smaller effect on the electrical characteristics of most transistors. It was found, however, that in some power transistors a stress on the base side of the e-b junction causes the base current to decrease. Figure 45 is a plot of base current as a function of emitter-base voltage for constant emitter current and several stress levels. This device was an n-p-n power transistor manufactured by Solid State Products Inc. The stress was applied with a 0.7 mil sapphire needle near the emitter-base junction on the base side. As shown in the figure the base current can be made to decrease and go negative at low voltages and high stress levels. This means that the collector-base potential has been lowered by the stress to the point that the collector leakage is larger than the emitter current. Stress applied on the collector side of the base-collector junction was found to have little or no effect on transistor characteristics.

It can be concluded from this study of stress induced changes in the electrical characteristic of transistors that the most sensitive operating configuration for use in transducers is the common emitter mode with stress applied to the emitter side of the emitter-base junction. In this mode the gain or $\beta$ is changed with stress. Another way of looking at the phenomenon is to consider the emitter-base junction as a diode which, when stressed, results in altered electrical characteristics amplified by the gain of the transistor. In other words, similar effects could be obtained by using a diode stress transducer to bias a transistor. In many ways, this can be desirable since stress alters parameters in addition to gain.

One important point which has not been mentioned is the effect of generation-recombination current in transistors. These currents cause the base current not to have the same slope as the collector current when plotted
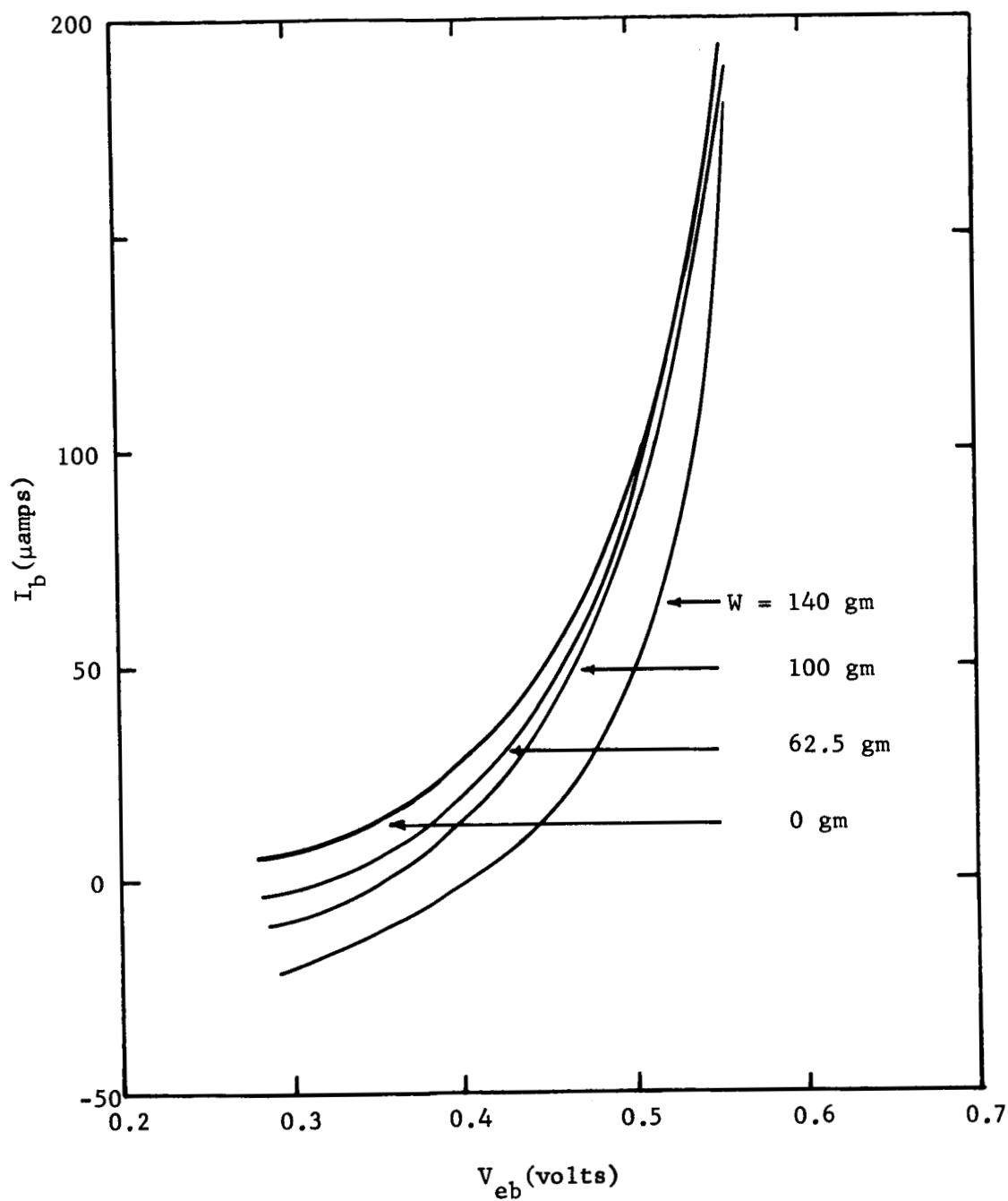
Fig. 45. Base Current of a Silicon Transistor as a Function of Emitter-Base Voltage with Constant Emitter Current and with Stress Applied to the Base with a 0.7 Mil Sapphire Needle.

against emitter-base voltage. These currents tend to lower the gain, especially at low emitter-base voltages. Although generation-recombination currents are subject to change with stress, as discussed in Sect. 3, they are not as sensitive to stress as the "ideal" currents. Like diodes, a transistor will be more sensitive to stress if the "ideal" currents predominate.

4.6  Four-Layer Diodes

Three junction devices (four-layer diodes) were fabricated and tested to determine the effect of mechanical stress on their characteristics. Both planar and mesa type devices were studied. The mesa structures were constructed in the same manner as the mesa diodes by replacing the single diffusion step in the diode case with three diffusions. In four-region devices, the first diffusion must be deep and must have a low surface concentration.

Two processes have been used to perform this diffusion. The first has been to use low impurity concentrations in the furnace and to diffuse for a long period of time ($\sim$ 64 hrs). The second method has been to make a shallow diffusion with a high surface concentration followed by a drive-in period. The drive-in has consisted of placing the sample in a furnace with no impurities present. The temperature and time allows the shallow junction to spread much deeper into the sample and also lowers the surface impurity concentration. The drive-in process was successful and yielded good reproducibility.

Figure 46 shows a sketch of a mesa 4-layer diode. Steel needles have been used to apply force to these devices. A simple analysis of the characteristics of these devices can be made by assuming they behave as two transistors connected together as shown in Fig. 47. In this arrangement,
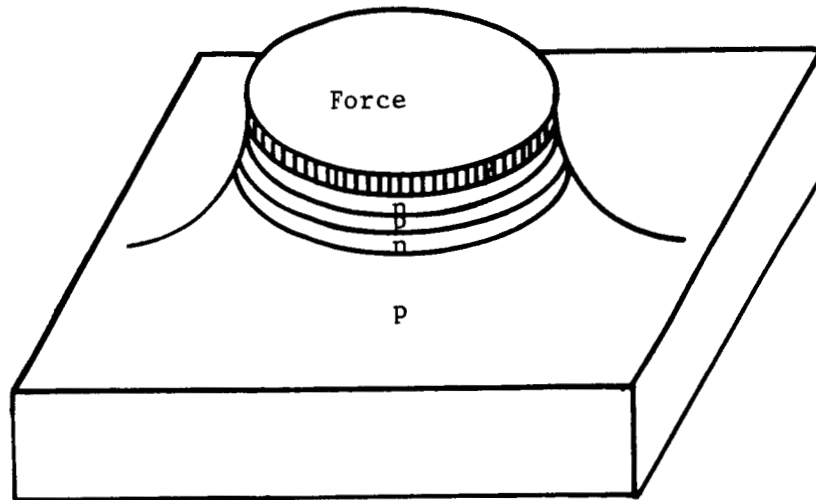
Fig. 46.  Sketch of a Mesa Type Four Region Device.
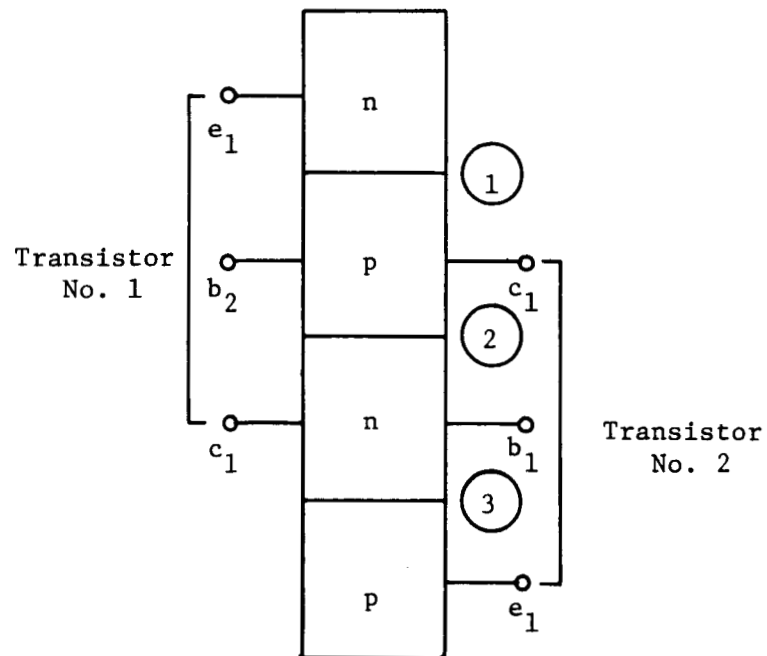


Fig. 47.  Transistor Equivalent of a 4-Layer Device.

transistor No. 1 has a base region common to the collector of transistor

No. 2 and a collector common to the base of transistor No. 2.

When a negative potential is applied to the top layer and a positive

potential to the bottom layer, junctions ① and ③ are forward biased while

junction ② is reverse biased. Since junction ② is reversed biased the

total device exhibits a large impedance. This remains the case until the

current reaches a level such that the sum of the two $\alpha$'s of transistors

No. 1 and No. 2 reach unity. At this point the voltage across junction ②

is near the breakdown voltage. It is at this point that the voltage-current

relationship becomes unstable and a lower voltage supports the same current

flow. Figure 48 is a photograph made on a transistor curve tracer showing

the I-V characteristics of a typical mesa 4-layer diode. Current is shown

on the vertical scale and voltage on the horizontal.
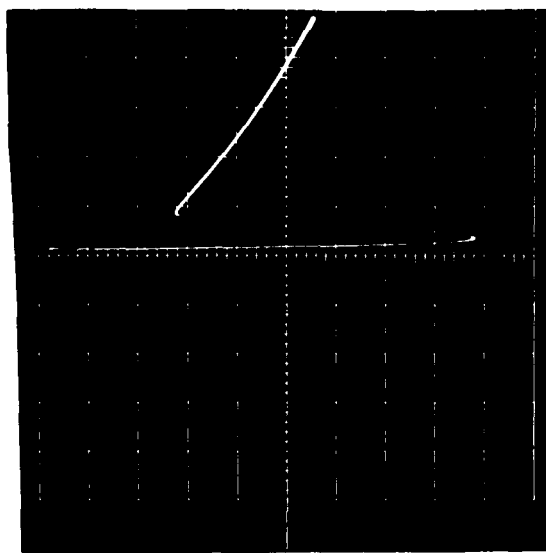


Fig. 48. I-V Characteristics of a Four Region Device.

When four region devices are subjected to mechanical stress the breakdown voltage is lowered. Figure 49 shows a photograph of the characteristics for several stress levels. In the figure the vertical scale is 2 ma/cm and the horizontal scale is 2 volts/cm. The curves from the right to left are for 0, 2.5, 100, and 115 grams respectively.
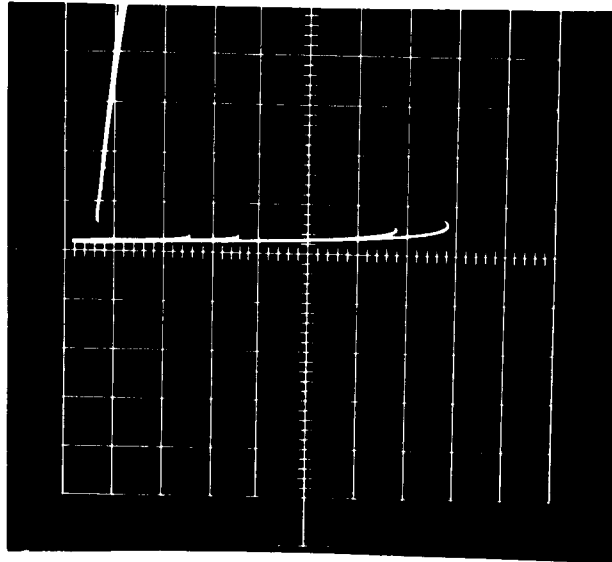


Fig. 49.   I-V Characteristics of a Mesa 4-Layer Device Under Stress.

Due to the negative resistance characteristics of 4-layer diodes, they are ideal elements to use in oscillator circuits. Figure 50 is a schematic of an oscillator circuit used to determine the effect of stress on the 4-layer diode and its relation to output frequency. Figure 51 shows the waveform of such an oscillator. When the four-region device is stressed, the oscillator increases and the amplitude decreases. Both of these parameters can be used as a measure of the force applied to the diode. Figure 52 is a plot of Δf and amplitude as a function of applied force for a device stressed with a 3 mil radius of curvature steel needle. Figure 53 is also a typical plot of Δf as a function of stress. In these devices, the stress level necessary to cause significant changes is slightly lower than for regular diodes or transistors.
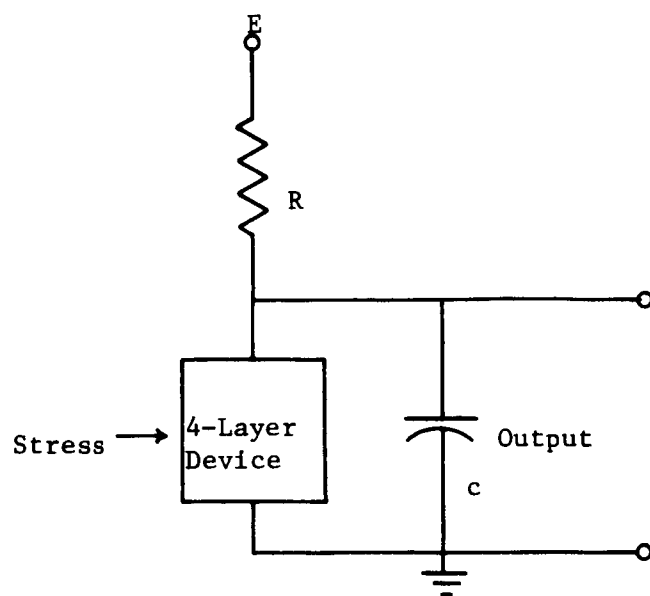
Fig. 50. Oscillator Circuit for 4-Layer Diodes.
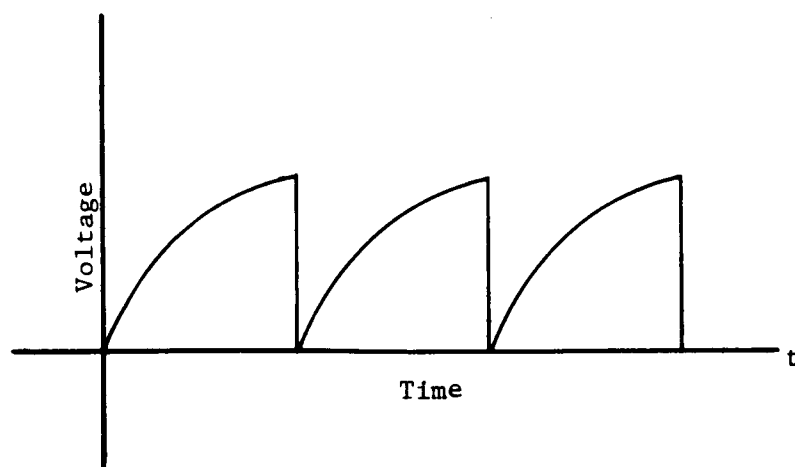


Fig. 51. Output Waveform of the Circuit Shown in Fig. 50.
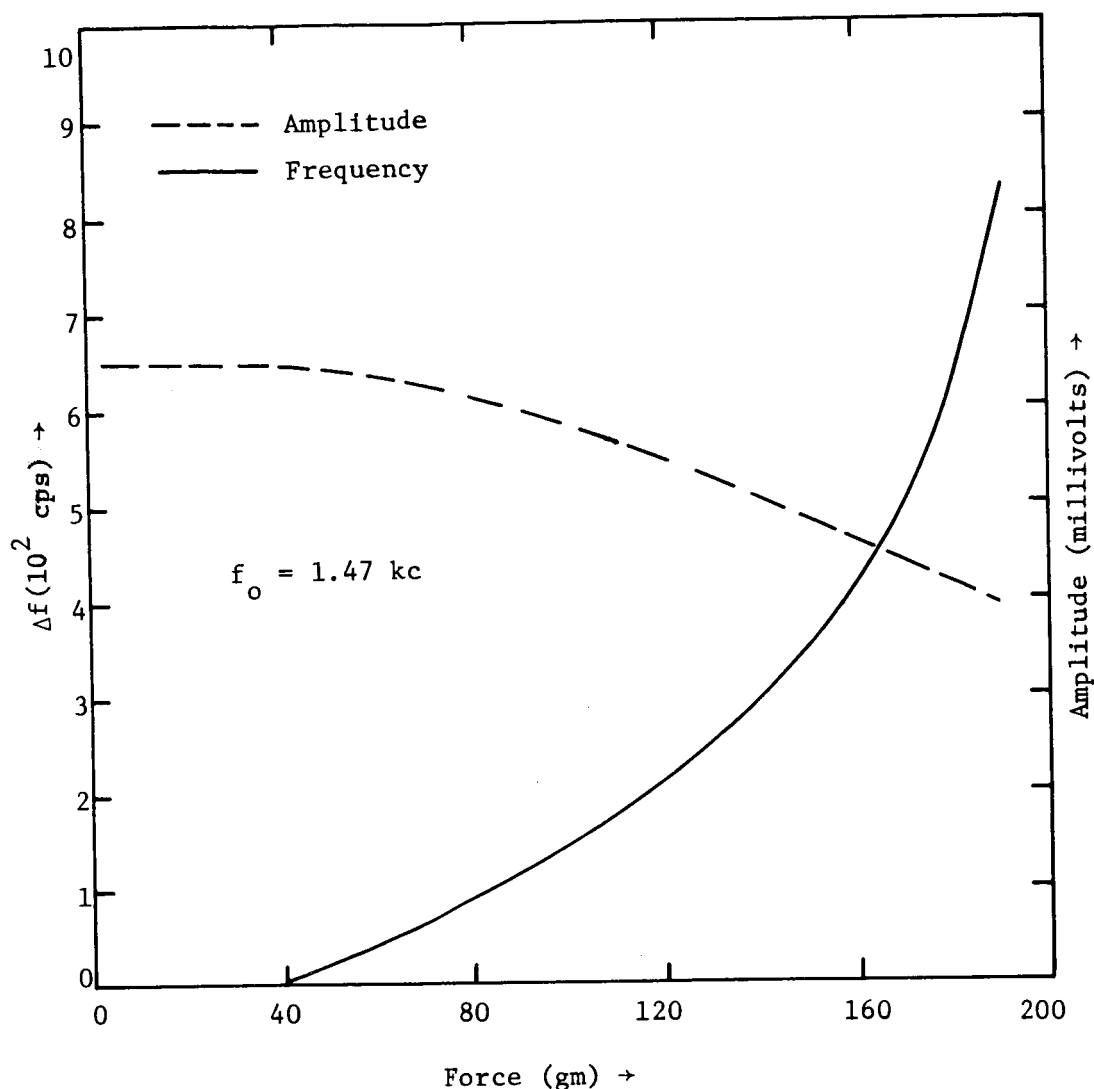
Fig. 52.  Oscillator Amplitude and Frequency Change (Δf) as a Function of
Force for a 4-Layer Switch Oscillator Under Stress.

Of the many different ways of using p-n junction devices as stress

sensors, the 4-layer diode oscillator is one of the most interesting.  It

is not only as sensitive as other devices but also provides a direct frequency

modulated output.  In general, it is much easier to read small changes in

frequency than it is current or voltage.  One very important consideration

along these lines is that the frequency of the oscillator can be varied over

a large operating range by simply varying the values of the resistor and

capacitor.
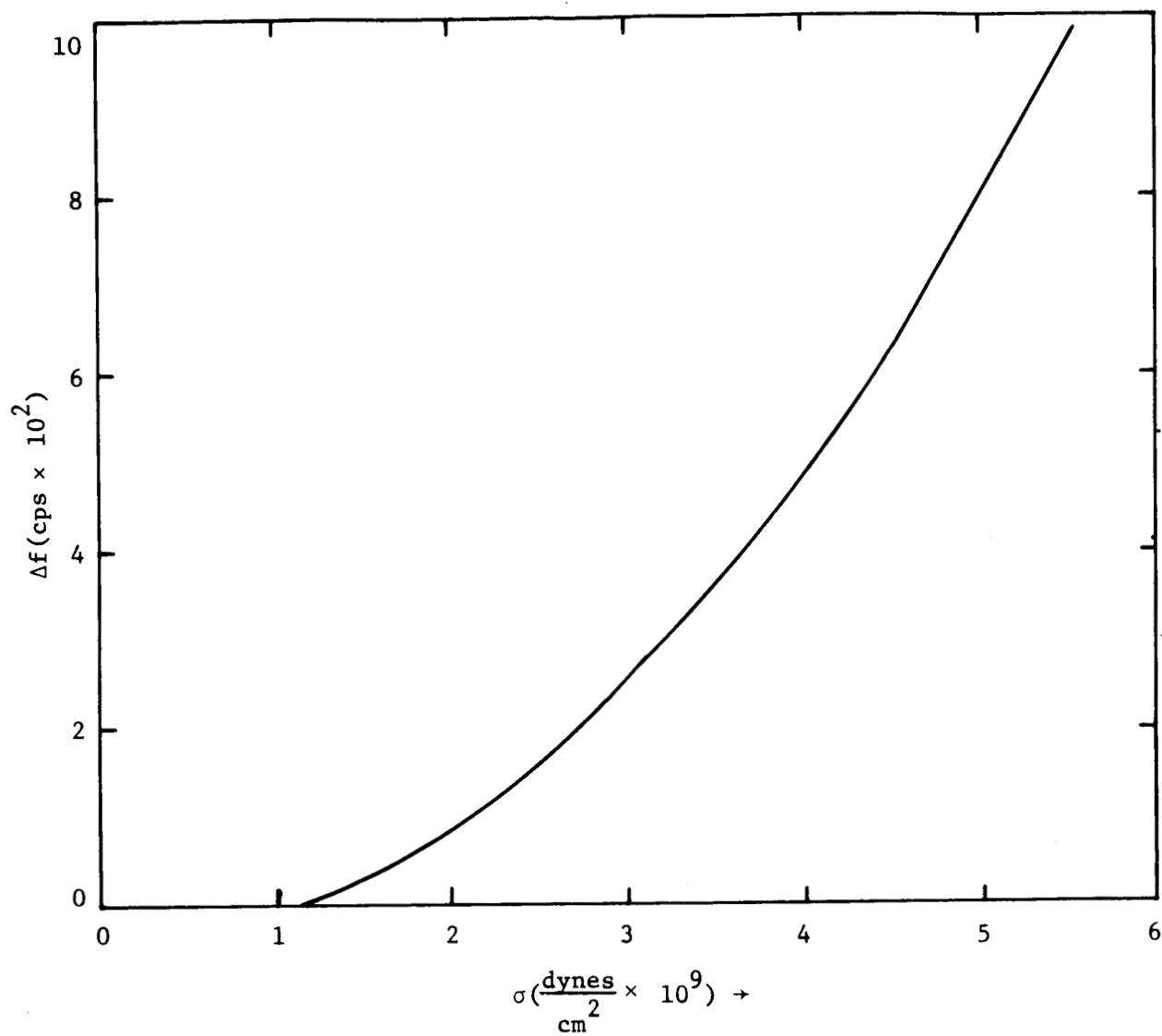
Fig. 53. Frequency Change as a Function of Stress for a Typical 4-Layer Switch Oscillator.

Chapter V

TRANSDUCER DEVELOPMENT

5.1 Introduction

In order to utilize p-n junction devices as stress transducers the stress level must be on the order of $10^9$ - $10^{10}$ dynes/cm$^2$. These stress levels are near the fracture strength of silicon and germanium. The fracture strength as measured using silicon bars is on the order of $3 \times 10^9$ dynes/cm$^2$. This value might be considered as a bulk value and, as evidenced by the stress levels used in this work, the fracture strength over small regions is considerably larger ($\sim 3 \times 10^{10}$ dynes/cm$^2$). Any useful transducer which utilizes the piezojunction effect will have to be designed with this fracture strength in mind.

There are several methods of obtaining the high stress levels needed for the piezojunction effect. Some of these methods are discussed in the following sections.

5.2 Indentor Point

The most widely used method of applying stress to p-n junction devices in early piezojunction experiments and transducers has been with indentor points. An indentor point, in most cases, is simply a steel, diamond, or

sapphire phonograph needle. Stress is applied to a p-n junction device by first placing the indentor point on the junction to be stressed and then applying a calibrated force to the indentor.

The major advantage to using an indentor point is that the stress is not a linear function of the applied force. As force is increased the stressed area increases. This means that fracture due to overstressing is less likely to occur. The most serious disadvantage inherent in this method of stress application is the difficulty of aligning the indentor point and the small junction area so that the point makes contact to the desired location on the junction. Since the stress levels required to produce the piezojunction phenomenon are high, it is necessary that the stressed area be small ($\sim$ mils) in order that the force required to generate these stress levels is not mammoth. The alignment process is very tedious and must be performed with the aid of a microscope. The complexity of this process is magnified several times when the indentor point stressing method is used in workable transducers which must be subjected to other than laboratory environments. Any lateral movement of the indentor point removes it from the desired junction area and often causes permanent damage to the junction.

Another disadvantage of the indentor point method of stress application is the difficulty of determining the area over which the stressing force is applied. This area, along with applied force, must be known in order to accurately predict the applied stress.

The indentor point method of stressing has been used successfully to build laboratory transducers for accelerometers [40]. Reference [40] describes in some detail the methods used and the results obtained using the indentor point method.

A variation of the indentor point method is often used to apply stress to mesa devices. The indentor point is called a post in this instance because the radius of curvature of the indentor point is much larger than the diameter of the device being stressed. Thus, the entire area of the junction device is stressed by the post. Alignment in this case is not as critical and difficult.

## 5.3 Cantilever Beam

A cantilever beam can be used to apply stress to a p-n junction. This can be accomplished by first fabricating a small, thin beam from single-crystal silicon. A p-n junction is then formed on one side of the beam. Stress is applied by forcing the loose end of the beam up or down. The big disadvantage to such a system is the fracture strength of silicon. In general, a cantilever beam will fracture before the stress levels necessary to effect p-n junction characteristics are reached. Attempts have been made to solve this problem by etching a notch in the beam directly opposite the junction [41]. Although this method of concentrating the stress has had some success, the manufacturing processes and yield would very likely prohibit their use. Also, it would be very fragile and easy to overstress.

A variation of the cantilever beam is a beam which is attached to a fixed base at both ends. The principle of operation is identical to the cantilever beam except force is applied to the center of the beam.

The advantages of these methods over the indentor point and post methods is that no alignment problem exists. Also, electrical contact with all junctions is easily attained.

## 5.4 Diaphram

Another method of utilizing the piezojunction phenomenon is a semi-conductor diaphram. The diaphram is etched from a substrate of the desired material to a thickness at which a reasonable force will create the desired stress level. For silicon and reasonable seismic masses the thickness is less than 5 mils. A p-n junction is formed in the center of the diaphram. It is preferable to use the planar process for this junction formation. Stress is applied to the junction in the same manner as for the cantilever beam.

This diaphram is extremely fragile and, thus, very difficult to fabricate. However, it shows a great potential for application to pressure transducers.

## 5.5 Semiconductor Needles

Another method of applying stress to a junction device, and the method considered most applicable to acceleration transducers, is the semi-conductor needle. The semiconductor needle is an outgrowth of alignment difficulties encountered with the indentor point stressing method. A semiconductor needle is fabricated from a bar of the desired material by using an electroetching technique developed for this purpose. A p-n junction is formed on the apex of the needle by either the mesa or planar techniques, and stress is applied by forcing the needle onto a conductive surface. The silicon semiconductor needle is covered in detail in the following section of this report.

5.6  Silicon Needle Development

As stated in the previous section, the semiconductor needle was developed to alleviate difficulties encountered with other methods of stress application to a p-n junction device. Although the method is equally applicable to any semiconductor, all descriptions of the processes and techniques will specify n-type silicon for convenience.

The needle fabrication process begins by using a diamond saw to slice the sample material into rectangular bars approximately $\frac{1}{2}$ inch long and 20 mils on each side. (The sample material most extensively used has been 1 ohm-cm n-type silicon). These bars are then silver soldered into the ends of brass rods which have been previously drilled for this purpose so as to provide mechanical support and electrical contact for the following electroetching operation.

A plastic vat with a valve near the bottom is used to hold and control a nitric acid-hydrofluoric acid etching solution. The ratio of $HNO_3$ to HF is 21 : 4. A platinum wire is wound around the inner periphery of the vat for use as an electrode for the process. The etching solution is allowed to slowly drain out through the valve and thereby lower the liquid level in the vat at a controlled rate.

A mechanical manipulator is used to raise and lower the brass rod-silicon bar assembly, and is initially set so that the tip of the silicon bar is approximately $\frac{1}{8}$ inch below the surface of the etching solution. The solution surface is simultaneously allowed to recede at a rate of approximately $\frac{1}{8}$ inch per minute. A high intensity light source is used to provide hole-electron pairs at the silicon-solution interface to aid in the electroetching process [42,43]. An ac potential of approximately 30 volts

RMS is applied using the brass rod-silicon bar assembly as one electrode and the platinum wire as the other. This allows a current of approximately 20 ma RMS to flow through the system.

Silicon needles fabricated by this process are highly polished and possess tip diameters on the order of 1 to 50 microns. The radius of curvature of the tip depends on the initial size of the silicon bar, the initial depth of the bar beneath the surface of the etching solution, the solution surface descent rate, the solution concentration and mixture ratio, the current density through the system, the intensity of the light source, and the temperature of the solution. Figure 54 is a photomicrograph of a needle compared to a silicon bar. Figure 55 is a photograph of the apparatus used to fabricate the needles.



Fig. 54. Photograph of a Silicon Needle and a Silicon Bar (width of bar is 20 mils).

Fig. 55.   Photograph of Apparatus used to Fabricate Silicon Needles.

Diodes have been fabricated on the apexes of needles made by the procedure described above using both the mesa and planar processes.   The following discussion covers both processes, taking the mesa process first.

Following the etching operation, the needle was cleaned and placed in an ordinary diffusion furnace where a p-type dopant was diffused into the needle surface to a desired depth thereby forming a p-n junction between the diffused layer and the bulk material.   Following the diffusion operation the needle was plated over its entire surface area with electroless nickel.

In order to reduce the p-n junction area and to get electrical contact to the bulk material, the diffused layer was etched away everywhere except the apex of the needle.   This was done by lowering the needle point into a molten wax solution to the desired depth and was followed by an etch to remove the diffused layer.   The etch did not attack the wax.   After the diffused layer was removed the wax was removed leaving the finished needle.

Figure 56 is a sketch of a needle sensor made by this process.



.020"

1/2"

N-Type Si

Diffused P-Type Silicon

Nickel

1/8"

$\tilde{=}$ 1/32"

1 to 50 μ
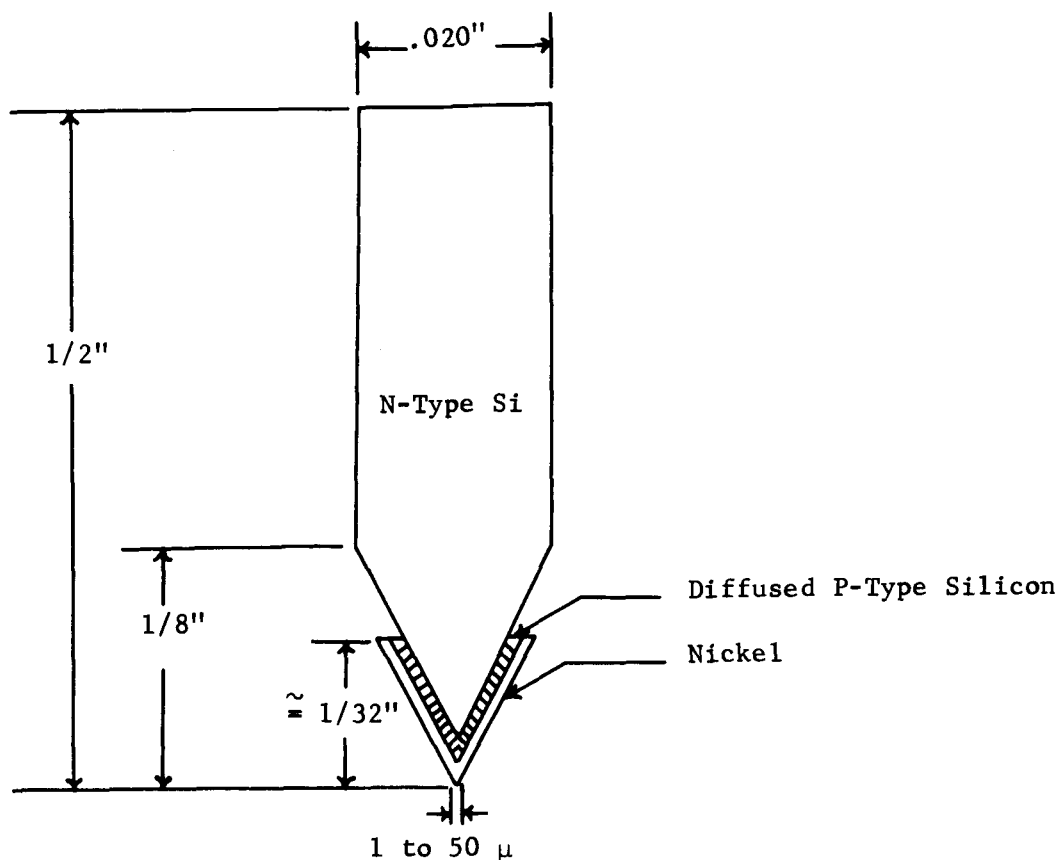
Fig. 56. p-n Junction Stress and Strain Sensor, Mesa Type.

Needle sensors made by the above process were found to be sensitive to applied stress. However, they had two major disadvantages. First, they were very susceptible to mechanical failure at the junction - bulk material interface. Second, this same interface was not protected, leaving the junction open to contamination from the atmosphere. This allowed the electrical characteristics to drift with time.

The planar process for fabricating needle sensors was found to be a much more suitable process. The needle was first placed into a oxidation furnace where an oxide was formed over the entire surface.

The needle was then coated with a photosensitive acid resist (KTFR*) and allowed to dry. This acid resist has the property of remaining intact after development wherever it has been exposed to light.

Next, the apex of the needle was lowered into molten black wax to a depth of a few mils using a mechanical manipulator. The photoresist was then exposed using an intense light source. It is desirable that only a small portion of the tip be submerged into the wax as this later determines the junction area. The photoresist was then developed in TCE which removed the wax and unexposed resist leaving a protective coating over all except the very apex of the needle.

The needle was then submerged into a dilute HF solution which removed the oxide from the unprotected apex exposing the bulk material.

The next step was to place the needle into an ordinary gas diffusion furnace where a p-type dopant was diffused into the unprotected apex. The oxide on the remainder of the needle prevented it from being diffused. An effort was made to form a junction which was shallow in depth and high in surface concentration as this combination was found to be more sensitive to stress.

A layer of aluminum was then evaporated over the entire needle. Next, the apex of the needle was coated with wax for protection, and the aluminum chemically etched away from all except the wax protected portion of the needle. This process left a metallic contact on the diffused or p-region of the junction.

The apex of the needle was once again protected by wax, making sure that the wax extended past the aluminum contact. The unprotected part of the needle was then etched which removed the oxide.

---

* KTFR is an Eastman Kodak trade name.

The needle was then placed into a electroless nickel solution which deposited a metallic electrical contact on the bulk or n-region of the diode. With this step, the needle sensor was completed. Figure 57 is a sketch of a needle sensor made by the planar process and Figure 58 is a photomicrograph of a finished needle.
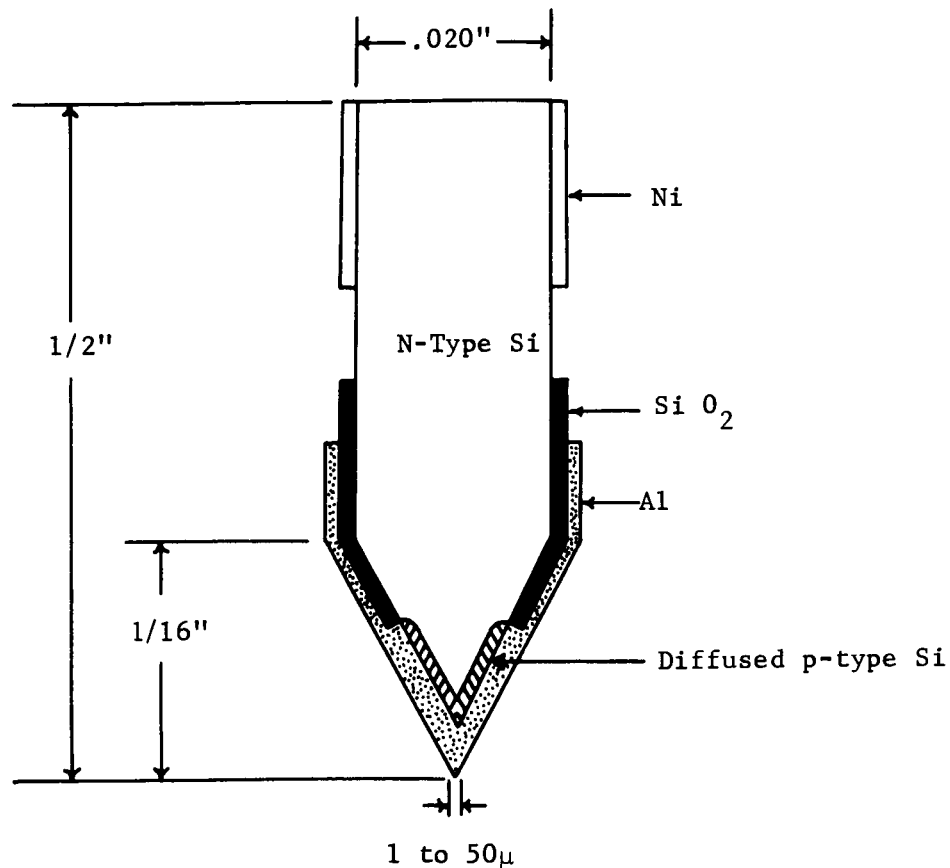


Fig. 57. p-n Junction Stress and Strain Sensor, Planar Type.
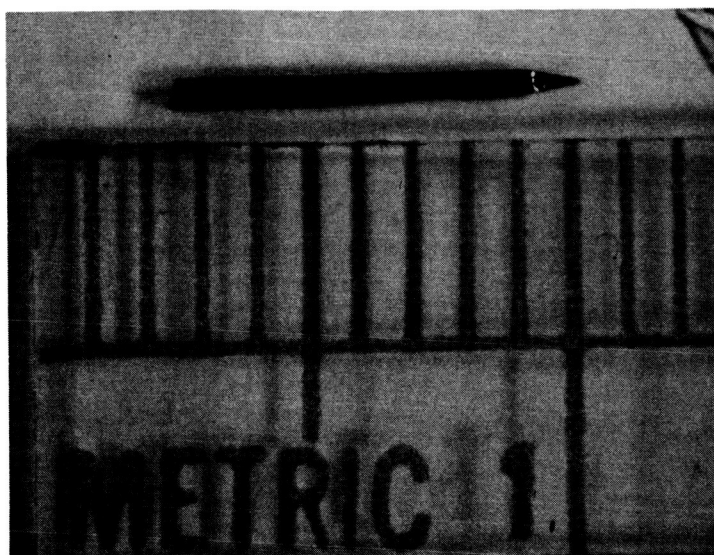
Fig. 58. Photomicrograph of a Finished Needle Sensor (the 1 represents 1 cm).

Needle sensors made by the planar process are more mechanically rigid and electrically stable than sensors made by the mesa process. This is due to the fact that no notch is etched into the needle at the junction interface in the planar process and the junction is inherently passivated by the oxide.

The needle sensor described herein eliminates the critical alignment prevalent in the indentor point method of stress application. It inherently allows smaller areas to be stressed than does other existing methods and, therefore, can be made more sensitive.

The processes described above for fabricating needle sensors are given as typical processes and are not the only processes. The above processes are similar to processes used in the semiconductor industry to fabricate mesa and planar devices. P-n junction or junctions can be formed on the apex of the semiconductor needle by any of the techniques commonly used in industry.

A photograph of the forward I-V characteristics under stress of a silicon needle sensor made by the planar process is shown in Fig. 59. The curve to the far right represents zero stress, with stress increasing for each curve in the direction of the origin. The horizontal scale is 0.2v/cm and the vertical scale is 0.01 ma/cm.
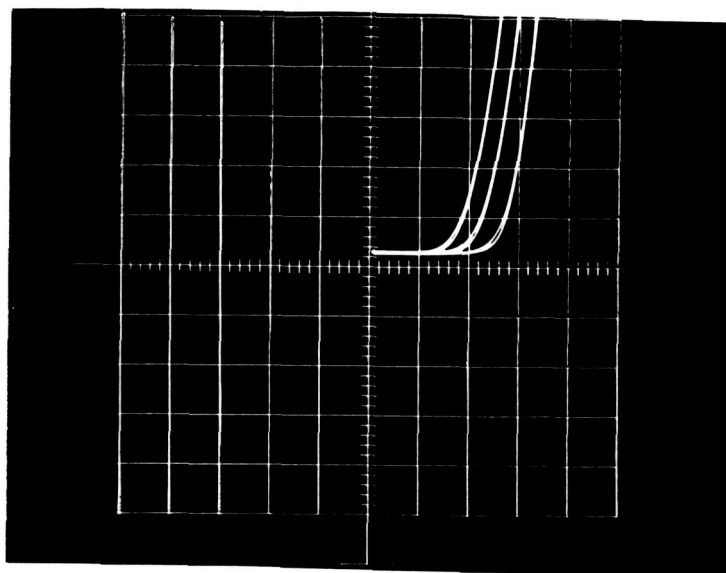


Fig. 59.   Forward I-V Characteristics of a Silicon Needle Sensor Under Stress.

The forward $\ell$nI vs. V characteristics of a silicon needle sensor whose junction depth was $\frac{1}{4}$ micron and apex radius of curvature was 17 microns is shown in Fig. 60.   The values of the force required to produce the noted changes are marked on the respective curves.

Figure 61 shows the effect of stress on the reverse $\ell$nI-V characteristics of the same needle sensor.   Again, the values of stress required to produce the piezojunction effect are listed on the respective curves.

As can be seen from the above stress data, the silicon needle is sensitive to stress.   Based on the results of this work on silicon needles,
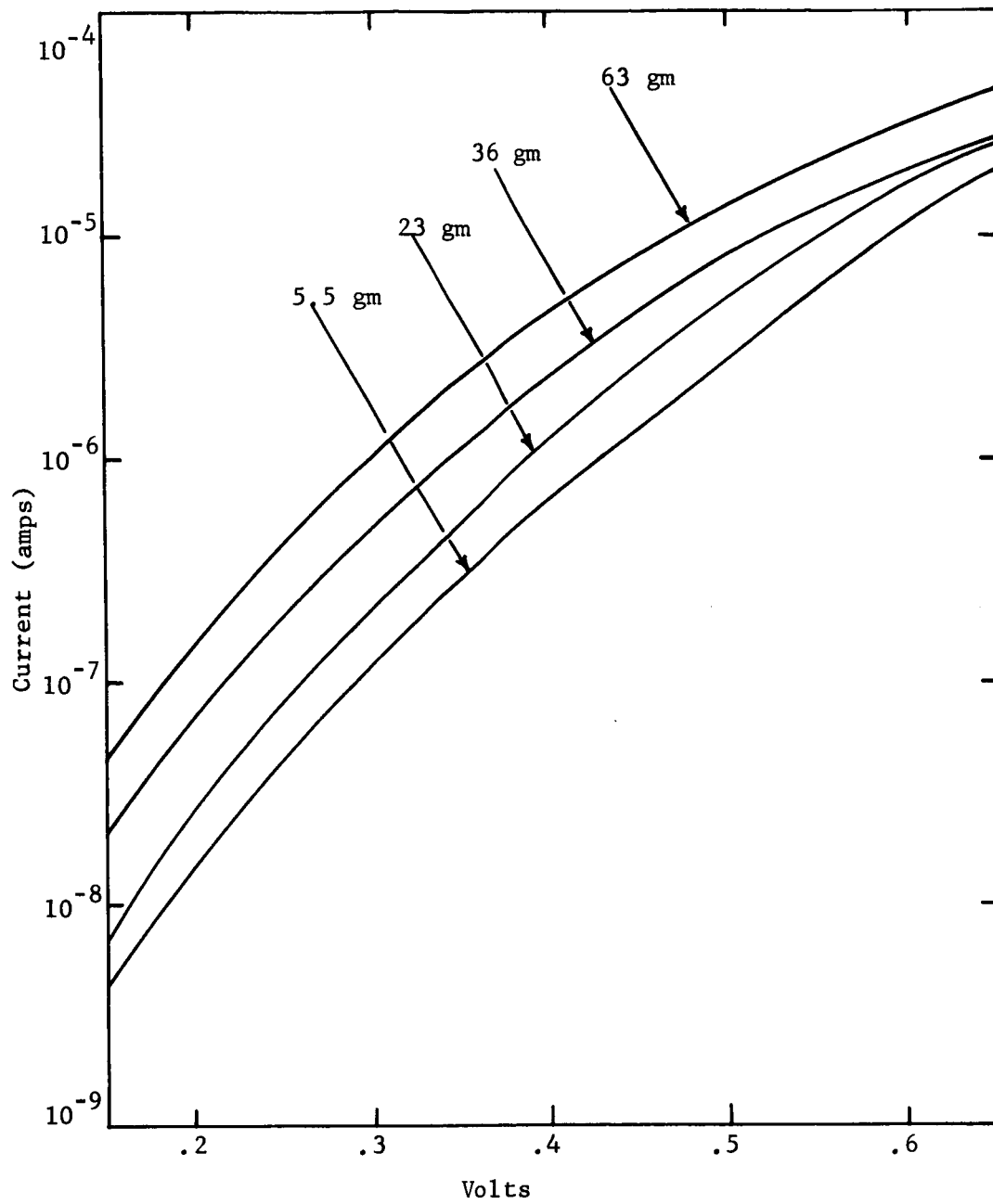
Fig. 60. Forward I-V Characteristics of a Silicon Needle Sensor Under Stress, Planar Type (Junction Depth = 0.25 μ, Diameter of Needle = 17μ).
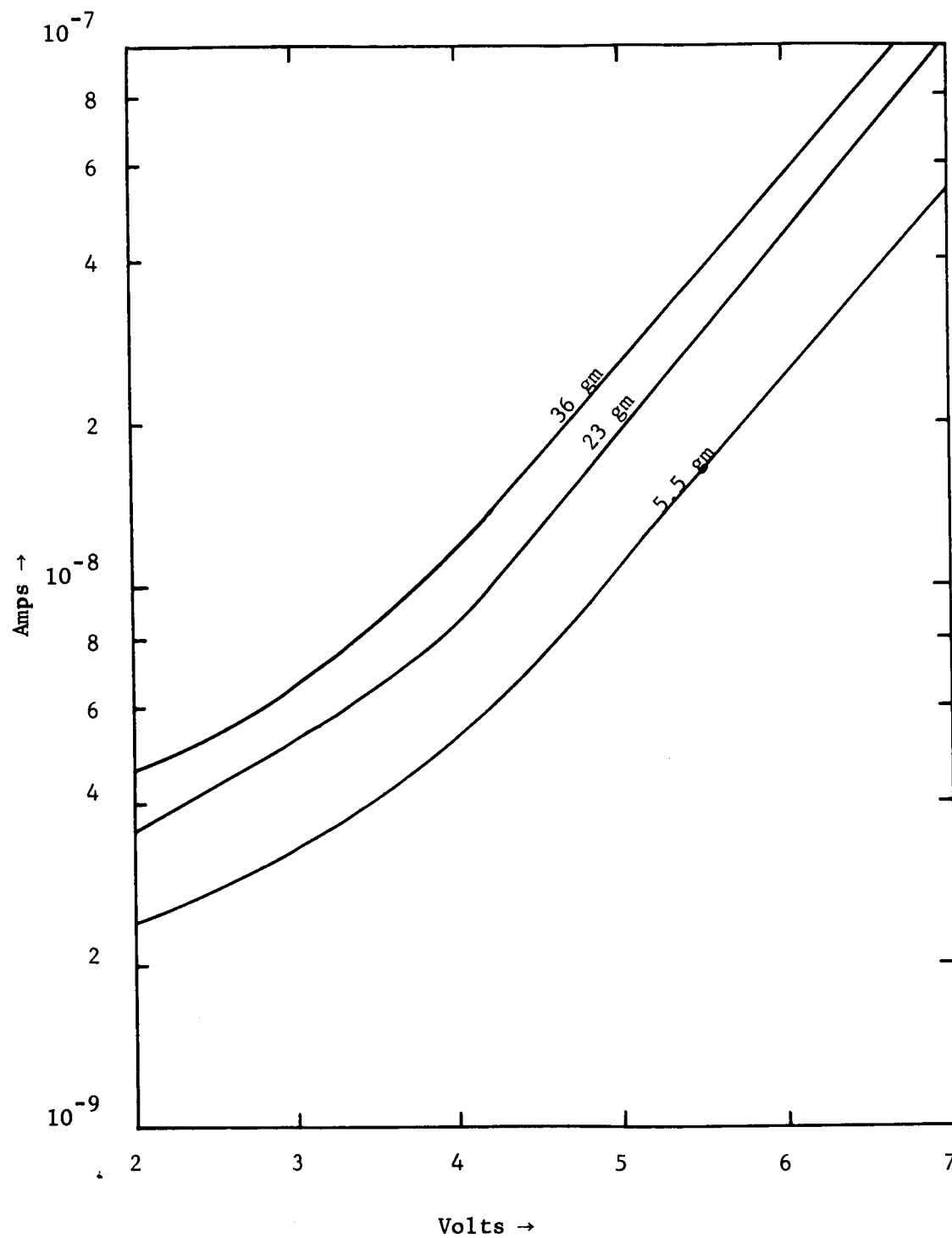
Fig. 61. Reverse I-V Characteristics of a Silicon Needle Sensor Under
Stress, Planar Type (Junction Depth = .25 μ, Diameter of
Needle = 17 μ).

it should be possible to use this type of structure as a transducer for measuring force, displacement, and acceleration.

Although none have yet been successfully fabricated, a 4-layer diode in the form of a needle looks very promising as a stress transducer. Such a device would possess the simplicity and sensitivity of a single junction sensor and the force to frequency conversion capabilities of a 4-layer diode.

Initial attempts to fabricate a four layer diode in needle form used the mesa method as described earlier for single-junction devices. However, the stability problem encountered with the single-junction sensors made by this process was found to be much more critical in the case of the four layer diode. Thus the mesa process was abandoned in favor of the planar process.

The development of a process for fabricating the 4-layer needle sensor has been inherently slow due to a necessity that the first of the three junctions be extremely deep. This diffusion has been accomplished on needles using the two methods described in a previous section (4.6) for such devices on wafer substrates.

As already mentioned, the fabrication of 4-layer diodes on wafer type substrates has been very successful. There is no apparent reason why this same or a similar process could not be used to fabricate the device in needle form. Although it will require extremely tedious masking techniques, the development of a process for making four layer needle sensors is just a matter of time.

Chapter VI

ACCELEROMETER DEVELOPMENT

6.1  Introduction

The silicon needle stress and strain sensor described in the previous
section of this report was incorporated into a working laboratory accelero-
meter.  This accelerometer was developed for the purpose of demonstrating
the applicability of the piezojunction phenomenon to a practical transducer
for measuring acceleration.

It might be pointed out that the manufacturing aspects of such
accelerometers has been kept in mind throughout this work.  Included is a
comparison of this accelerometer with existing accelerometers.

6.2  Accelerometer Design

An accelerometer is an instrument capable of measuring acceleration
or detecting and measuring vibrations.  Accelerometers used in space vehicle
instrumentation systems must be capable of transforming these mechanical
inputs into electrical signals.  An accelerometer usually consists of a
seismic mass on which acceleration can act, a spring to return the mass to
its original position once the acceleration has subsided, and a transducer
element to detect this force of acceleration and convert it to a usable
electrical signal.

(110)

The most critical component of an accelerometer is the sensing element. One of the most difficult problems confronting the design of an accelerometer based on the piezojunction effect is that of applying stress to the junction device. This problem has been solved by use of the semiconductor needle sensor (see Chapter V). Therefore, all accelerometer design efforts discussed herein have incorporated the silicon needle sensor as the transducer element.

The range of operation of an accelerometer based on the piezojunction effect is controlled by many factors. First, the characteristics of the sensor to be used must be known and the range of stresses to which it is sensitive. Then, a seismic mass must be chosen that will apply this range of stresses when subjected to accelerations over the range of interest. Table III was tabulated as an aid to determining the range of operation.

Table III was computed using a seismic mass of 1 gram. It can be used for other seismic masses by multiplying all of the values of stress by $\frac{M_n}{1 \text{ gram}}$. $M_n$ is the new seismic mass. For example, if the use of a 10 gram seismic mass is necessary, all values in each column under $\sigma$ would be multiplied by 10. This manipulation will make the values of the $\sigma_1(1g)$ column equal to the $\sigma_2(10g)$ column.

Example: It is desired that a junction device be chosen for an accelerometer to measure the range of 10 to 100 g's. Silicon needles, such as the units described in Chapter V, are available in diameters of 1 through 10 mils (much smaller diameters are actually available). Tests have shown these type sensors to be sensitive to stress levels in the $10^9$ - $10^{10}$ dynes/$cm^2$ region.

Table III

Sensor - Seismic Mass Selector Chart
(Based on M = 1 gram).

| Diameter (mils) | 1G | 10G | 100G | 1000G |
|---|---|---|---|---|
| | $\sigma_1$ (dynes/cm$^2$) | $\sigma_2$ (dynes/cm$^2$) | $\sigma_3$ (dynes/cm$^2$) | $\sigma_4$ (dynes/cm$^2$) |
| 1 | $2.04 \times 10^8$ | $2.04 \times 10^9$ | $2.04 \times 10^{10}$ | $2.04 \times 10^{11}$ |
| 2 | $5.1 \times 10^7$ | $5.1 \times 10^8$ | $5.1 \times 10^9$ | $5.1 \times 10^{10}$ |
| 3 | $2.27 \times 10^7$ | $2.27 \times 10^8$ | $2.27 \times 10^9$ | $2.27 \times 10^{10}$ |
| 4 | $1.27 \times 10^7$ | $1.27 \times 10^8$ | $1.27 \times 10^9$ | $1.27 \times 10^{10}$ |
| 5 | $8.18 \times 10^6$ | $8.18 \times 10^7$ | $8.18 \times 10^8$ | $8.18 \times 10^9$ |
| 6 | $5.76 \times 10^6$ | $5.76 \times 10^7$ | $5.76 \times 10^8$ | $5.76 \times 10^9$ |
| 7 | $4.16 \times 10^6$ | $4.16 \times 10^7$ | $4.16 \times 10^8$ | $4.16 \times 10^9$ |
| 8 | $3.2 \times 10^6$ | $3.2 \times 10^7$ | $3.2 \times 10^8$ | $3.2 \times 10^9$ |
| 9 | $2.52 \times 10^6$ | $2.52 \times 10^7$ | $2.52 \times 10^8$ | $2.52 \times 10^9$ |
| 10 | $2.04 \times 10^6$ | $2.04 \times 10^7$ | $2.04 \times 10^8$ | $2.04 \times 10^9$ |

It is necessary that the proper seismic mass and sensor diameter combination be chosen to apply stress within the sensitivity range of the device over the acceleration range of 10 to 100 g's. Referring to Table A, a 1 mil diameter sensor and a 1 gram seismic mass will allow $2.04 \times 10^9$ dynes/cm$^2$ to be applied at 10 g's and $2.04 \times 10^{10}$ dynes/cm$^2$ at 100 g's. A ten gram weight and the same 1 mil sensor will provide the same range of sensitivity for an acceleration range of 1 to 10 g's. A 100 to 1000 g device could be theoretically obtained by choosing a 4 mil sensor and a 1 gram seismic mass.

From the example shown above it can be seen that almost any reasonable range can be attained by properly selecting the sensor diameter seismic mass combination. Care must be taken, however, not to allow excessive stress to be applied to the sensor as it will destroy the device. Unfortunately, it is very difficult to predict the sensitivity of a sensing device before its fabrication because of the difficulty in controlling the area of the junction to be stressed and the diode properties. The present state-of-the-art limits selection of the sensor for such applications to empirical methods.

The major parameter to be considered when selecting the spring component is mechanical resonance frequency. It is this frequency (or frequencies) that limits the frequency range of the accelerometer.

In general, all accelerometers of the type discussed herein conform to the mechanical schematic diagram of Fig. 62.

K₁ = Spring constant of spring

K₂ = Spring constant of silicon

M₁ = Mass of spring

M₂ = Seismic mass
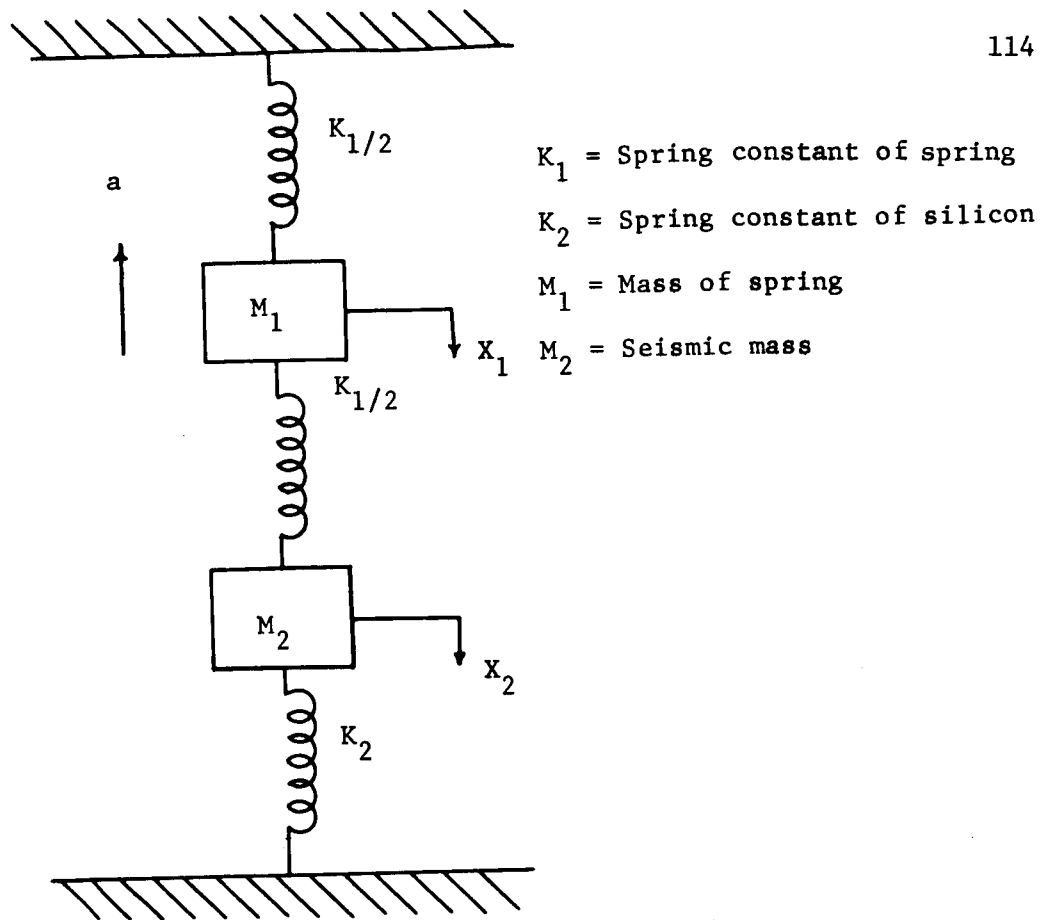
Fig. 62. Mechanical Equivalent of an Accelerometer.

The system shown in Fig. 62 has two degrees of freedom and, thus, requires two equations to describe its behavior [44]. Assuming that friction is negligible, the system is defined by the equations,

$$M_1 \frac{d^2 x_1}{dt^2} + \frac{K_1}{2} X_1 + \frac{K_1}{2}(X_1 - X_2) = 0 \qquad (6.1)$$

$$M_2 \frac{d^2 x_2}{dt^2} + K_2 X_2 - \frac{K_1}{2}(X_1 - X_2) = 0 \qquad (6.2)$$

Assuming solutions of the form

$$X_1 = C_1 \quad \text{Sin}(wt - \alpha) \quad \text{and} \qquad (6.3)$$

$$X_2 = C_2 \quad \text{Sin}(wt - \alpha) \quad , \qquad (6.4)$$

substituting into equation (6.1) and (6.2) gives the following solution for the resonant frequencies of the system:

$$f = \frac{1}{2\pi} \left\{ \frac{1}{2} \left[ \left(\frac{K_2}{M_2} + \frac{K_1}{2M_2} + \frac{K_1}{M_1}\right) \pm \left(\frac{K_2^2}{M_2^2} + \frac{K_1 K_2}{M_2^2} - \frac{2K_1 K_2}{M_1 M_2} + \frac{K_1^2}{M_1 M_2} + \frac{K_1^2}{4M_2^2} + \frac{K_1^2}{M_1^2}\right)^{1/2} \right] \right\}^{1/2}$$

(6.5)

It can be seen from Eq. (6.5) that a spring should be chosen which has a small mass as compared to the seismic mass. Thus, if $M_1 \ll M_2$ and $K_1 \leq K_2$ Eq. (6.5) becomes;

$$f = \frac{1}{2\pi} \left[ \frac{K_2}{M_2} \right]^{1/2}$$

(6.6)

This indicates that, if the mass of the spring is negligible relative to the seismic mass, the natural resonance frequency of the system depends only on the silicon spring constant - seismic mass ratio which is high. Using a Young's Modulus of $1.7 \times 10^{12}$ dynes/cm$^2$ for silicon and assuming that the applied stress is attenuated in 5 microns [45], the spring constant for silicon ($K_2$) is found to be $1.8 \times 10^{10}$ dynes/cm while the deformation is approximately .03 microns for stress levels on the order of $10^{10}$ dynes/cm$^2$. Assuming a 1 gram seismic mass and the above value of $K_2$, the resonance frequency as defined by equation (6.6) is approximately 20 kc.

The spring constant of the spring component is not critical as long as the spring mass remains much smaller than the seismic mass. However, in high g accelerometer applications when it is necessary to reduce the seismic mass, the spring constant of this component could become important. In this case the device has two resonant frequencies as defined by Eq. (6.5). The lower frequency (minus sign of Eq. 6.5) is the frequency of interest.

This frequency is lowered if the two masses and spring constants are on the same order of magnitude.

6.3  Fabrication

One of the major problems of fabricating an accelerometer using the needle type stress sensor has been the mounting of the sensor.  It was necessary to develop a mounting technique which would provide both mechanical support for and electrical contact with the sensor.

An early attempt to provide this mechanical support and electrical contact made use of the eutectic characteristics of silicon and gold. Tantalum and molybdenum strips were gold electroplated and heated in an inert atmosphere above the silicon-gold eutectic temperature (377°C).  The sensor, held in a fixture made for this purpose, was brought into contact with the gold plated strips, creating a eutectic bond at the gold-silicon interface.  Unfortunately, the cross sectional area of the sensor (20×20 mils) was insufficient to provide good mechanical support for the needle sensor.

The needles were successfully mounted by utilizing a metal bracket for mechanical support and conductive. epoxy for electrical contact.  The metal bracket was made from tantalum and a hole was punched in it which firmly held the needle sensor when wedged into the hole.  The tantalum bracket was spot welded onto the desired base leaving the needle pointing perpendicularly away from the base.  A small amount of conductive epoxy was placed between the base of the sensor and the base onto which it was mounted to provide electrical contact.  Although sensors were successfully mounted by this process, it was a difficult task to perform without fracturing the sensor.

The most successful mounting technique was similar to the technique used to mount the silicon bars for the electroetching process (see Section V). A hole was drilled into a brass base to accommodate the sensor. A small chip of solder was dropped into the hole and the brass was heated to the melting temperature of solder. The sensor base was forced into the hole and the assembly allowed to cool. The solder held the sensor in place and provided electrical contact with the nickel on the base of the sensor. The tip of the sensor was left protruding slightly above the surface of the brass base.

Once the needle stress sensor was successfully mounted, the next problem was to incorporate the assembly into a laboratory accelerometer. One of the first attempts to accomplish this used a conventional TO-5 transistor header as the base. A needle stress sensor was mounted on the header using the metal bracket-conductive epoxy method described above. A copper strip was made into an L-shaped tab and placed in contact with the apex of the sensor. The copper tab was soldered to the conductive feed through leads provided on the header. A lead seismic mass of approximately 1.5 grams was placed on the tab directly opposite the point where the sensor came in contact with the tab. A photograph of an accelerometer fabricated by this method is shown in Fig. 63.

The accelerometer fabricated by this process exhibited excessive contact resistance between the sensor and the copper tab. This contact was erratic and could not be properly adjusted. Also, it was very difficult to place the initial stress bias onto the sensor without fracturing and destroying the device.
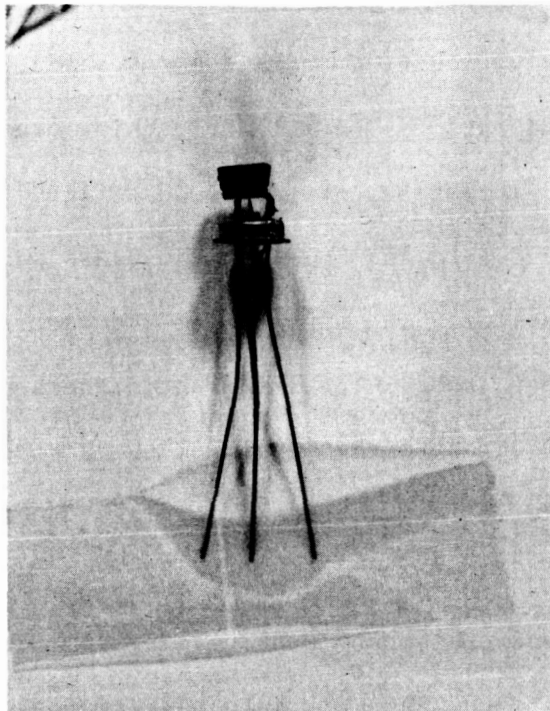
Fig. 63.   Photograph of a Laboratory Accelerometer, RTI No. 1.

From experience with this first accelerometer, it was found that
some mechanical means must be used to apply and adjust the initial stress
bias.   One simply could not assemble a device by this method using the delicate
needle sensors without fracturing them.

A needle sensor was then mounted into the end of a sharpened
brass screw by the soldering technique described herein.   This screw was
placed into a threaded hole in an aluminum base fabricated for this purpose.
A metal tab was insulated on the base so as to remain just over the tip
of the needle sensor.   A seismic mass was placed on the tab in the same
manner as for the accelerometer in Fig. 63.   The initial stress bias was
adjusted by holding up on the tab and turning in the screw mounted sensor
so that contact would be made when the tab was released.

Although the principle of stress biasing was sound, this device had the same high contact resistance characteristics as experienced in the previous device. The tab was gold electroplated in an effort to alleviate this problem. However, the contact resistance was not significantly reduced. This reduced the contact problem to the sensor and it was at this time that aluminum replaced the nickel as the apex contact material on the sensors. A photograph of this accelerometer is shown in Fig. 64.
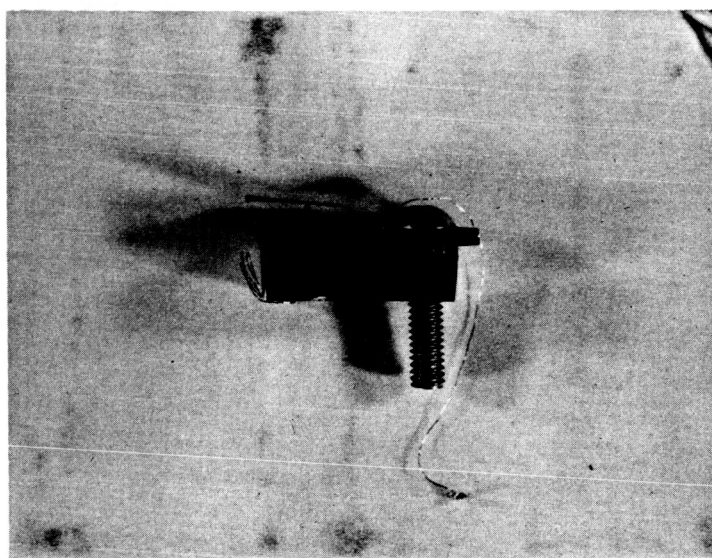


Fig. 64. Photograph of a Laboratory Accelerometer, RTI No. 2.

Another method of applying the initial stress bias used a brass header machined for this purpose. This header was very similar to a conventional transistor header and had a hole drilled into the center to accommodate the needle sensor. The sensor was mounted by the soldering technique. A glass tube which fit exactly over the header was cut so that, when the tube was all the way down on the header, the top rim of the glass was even with the apex of the sensor. Glass was used because it is a good insulator. A gold electroplated metallic diaphram was cut so as to

just cover the top of the pre-cut glass tube. This diaphram was epoxied to the glass cylinder. The assembly was gradually lowered down over the header on which the sensor had been mounted until the diaphram came in contact with the sensor and the desired initial stress bias was applied. Epoxy was placed on the header and allowed to dry with the diaphram in contact with the sensor under the desired initial stress bias. After the epoxy was cured, a seismic mass was placed on the diaphram directly opposite the point where the sensor made contact with the diaphram. An accelerometer (less seismic mass) made by this process is shown in the photograph of Fig. 65.
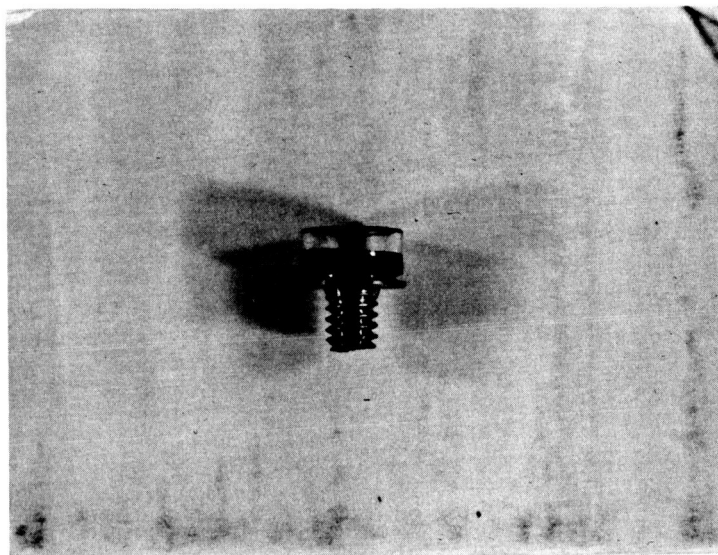


Fig. 65. Photograph of a Laboratory Accelerometer (Less Seismic Mass), RTI No. 3.

This device, although fairly difficult to fabricate, exhibited good electrical contact and could be used as an accelerometer. This was one of the first successful attempts to incorporate the needle stress sensor into a working laboratory accelerometer.

Another method which proved successful used a glass tube cylinder heated and closed on one end leaving only a small hole to accommodate a lead wire. A small steel spring was connected to the end of a brass piston which was machined to fit closely into the glass cylinder. The spring and piston assembly was gold electroplated and placed into the cylinder. One end of the spring protruded through the small hole in the glass tube and served as a lead. A sensor was mounted into a brass plunger also machined to fit into the glass cylinder. A lead was connected to the plunger on the end opposite the needle sensor. The plunger assembly was lowered into the open end of the tube until electrical contact was made with the piston and the proper initial bias was obtained. Epoxy was placed around the plunger to hold it firmly in place. A photograph of an accelerometer made by this process is shown in Fig. 66.
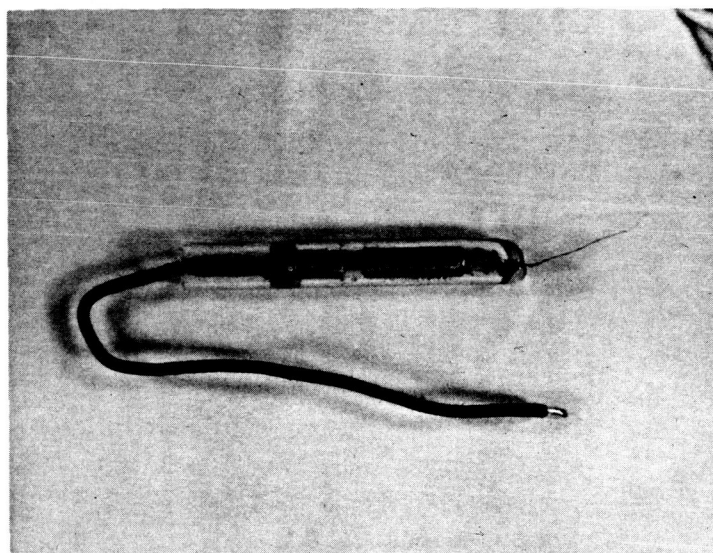


Fig. 66. Photograph of a Laboratory Accelerometer, RTI No. 4.

This process was refined by eliminating the rounded end of the glass tube and by introducing a more flexible initial biasing adjustment.

This final version consisted of a glass tube cylinder with a brass cap
machined to fit into each end of the tube. A spring and plunger assembly
similar to the one described above was connected to one of the end caps.
The other cap was drilled and tapped to accommodate a brass screw. Another
smaller hole was drilled beside the threaded hole for calibration purposes.
A needle sensor was mounted into the end of a brass screw and placed into
the threaded hole. Initial stress bias was adjusted by first inserting a
stiff wire into the calibration hole forcing back the piston, and then
turning in the screw mounted sensor. Once the sensor was in the desired
position, the piston was lowered onto the sensor and the wire removed.
Figure 67 is a photograph of an accelerometer made by this procedure while
Fig. 68 is an identical accelerometer except for size. Typical dimensions
of the smaller accelerometer is 1/2 inch in length and 1/4 inch diameter.
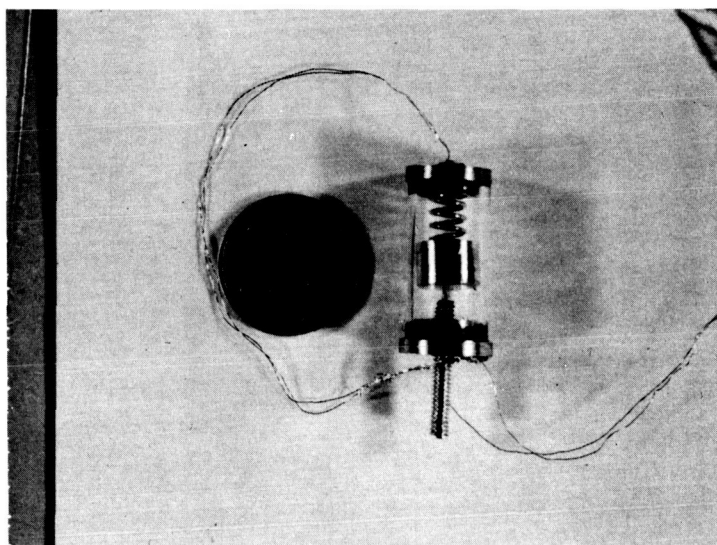


Fig. 67. Photograph of a Laboratory Accelerometer, RTI. No. 5.
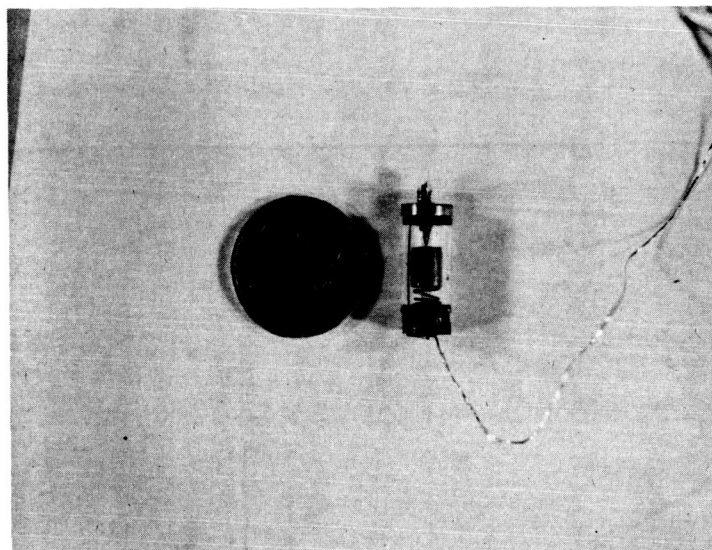
Fig. 68. Photograph of a Laboratory Accelerometer, RTI No. 6.

The accelerometers shown in Figs. 67 and 68 possess the best features of all the previous developments. The contact problem is solved by the gold plated piston and the aluminum coated planar sensor, and stress biasing is accomplished through use of the screw mounting technique. The entire package is neat in appearance, small in size, and rugged in construction relative to the other devices described. The limiting factor on the size of the device presently is the seismic mass. For very high g accelerometers, it is conceivable that the mass of the sensor could serve as the seismic mass, greatly reducing the overall size of the device.

The most sensitive of these accelerometers were calibrated by monitoring their electrical characteristics while rotating them in the vertical plane through a full 360°. This provided a sinusoidal input of acceleration ranging from a minimum of -1g to a maximum of +1g. The output from the device was nearly sinusoidal as can be seen in Fig. 69.

Other less sensitive accelerometers have been tested on an improvised centrifuge which allows the electrical characteristics of the
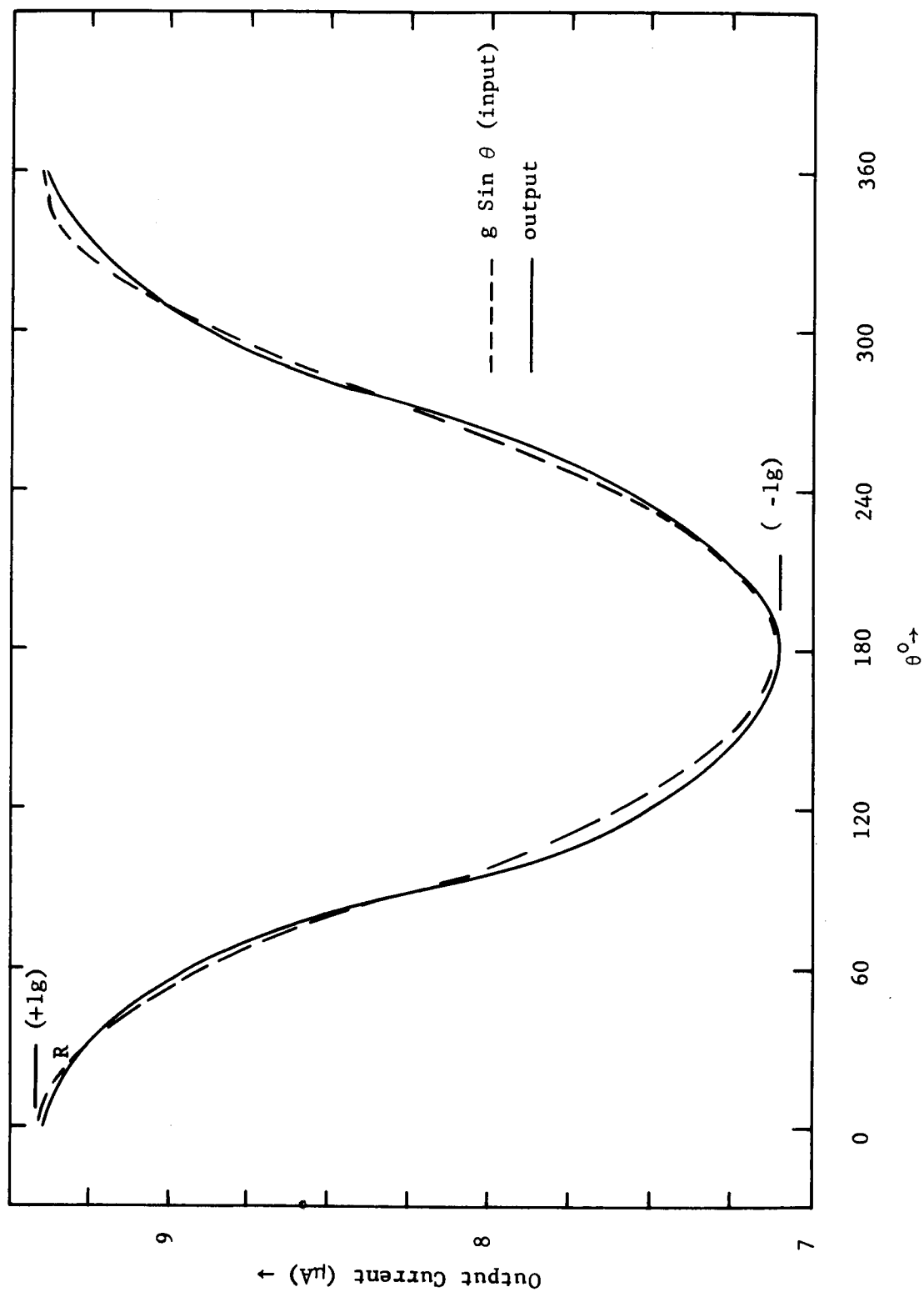
Fig. 69. Accelerometer Calibration Curve, RTI No. 5, ($V_{df} \cong .3v$).

devices to be monitored while subjected to centrifugal force-induced acceleration up to 100 g's.

Figure 70 is a calibration curve of a 100 g laboratory accelerometer biased in the forward direction at various voltages. The 0.5 volt curve, a typical operating voltage, is a straight line. This indicates that the forward current varies exponentially with acceleration as was expected. The change in forward current over the range of acceleration was not as large as desired. This is due, in part, to a small seismic mass ($\simeq$ 0.3 gm) and a relatively insensitive needle. This device could safely be used at higher g levels because of the small seismic mass.

Figure 71 is a calibration curve of the same accelerometer biased in the reverse direction at various voltages. The analysis for these curves is very similar to that given above for the forward direction.

## 6.4 Comparison with Existing Types of Accelerometers

Three of the most important characteristics of an accelerometer based on the piezojunction phenomenon are; (1) its adaptability to measuring any reasonable range of acceleration, (2) its very high frequency response due to the very small displacement needed to produce the effect, and (3) its ability to measure ac and dc accelerations. Another major advantageous characteristic is that, in multijunction form, it can produce a frequency modulated output proportional to acceleration. This characteristic is particularly desirable in space vehicle applications. Other characteristics of such a device are smallness in size and low power consumption. The only major disadvantage is that such devices are sensitive to temperature. However, this disadvantage can be greatly reduced by the proper design of associated circuitry.
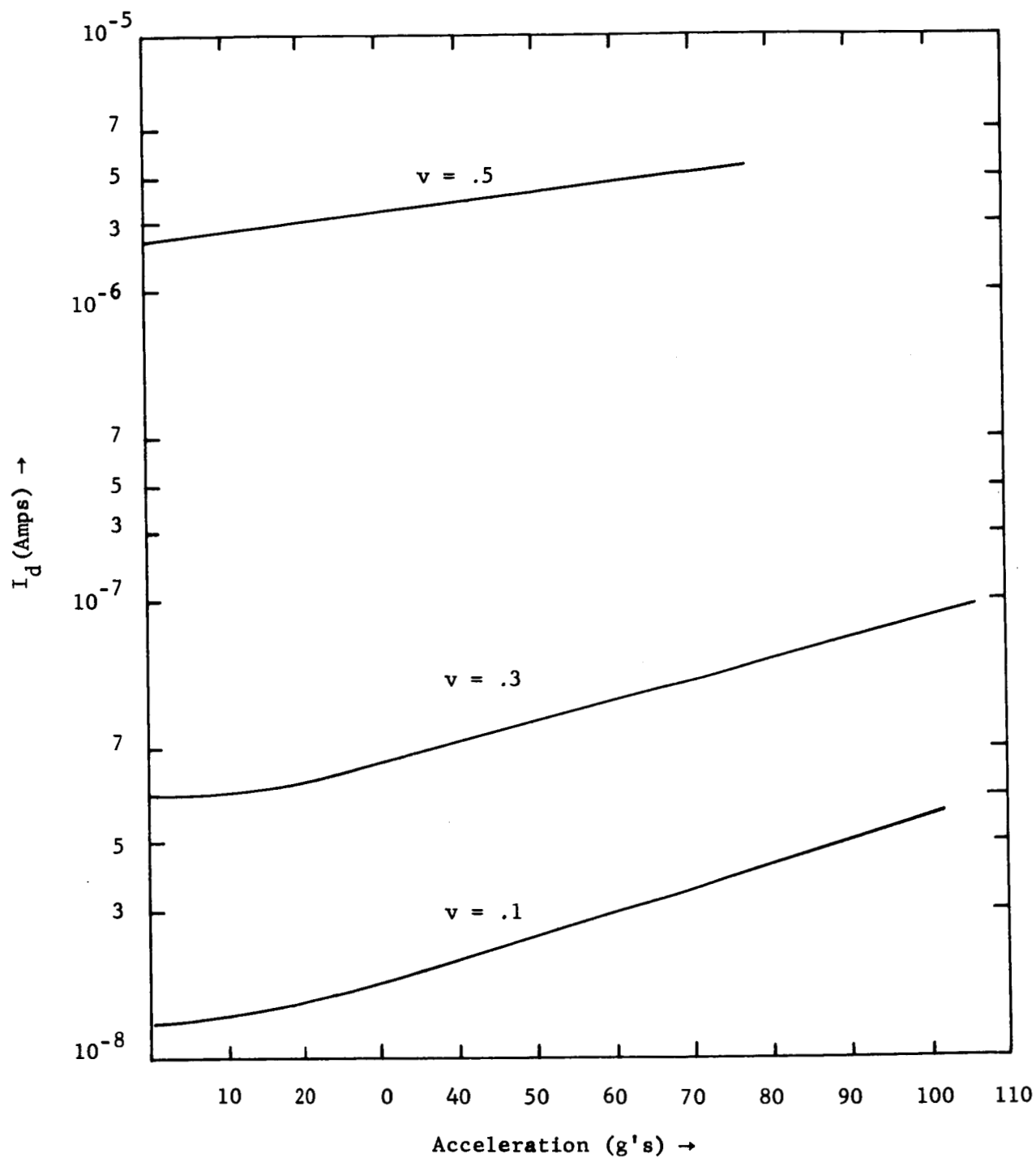
Fig. 70.  Calibration Curve of a Laboratory Accelerometer, Forward Biased, RTI No. 6.
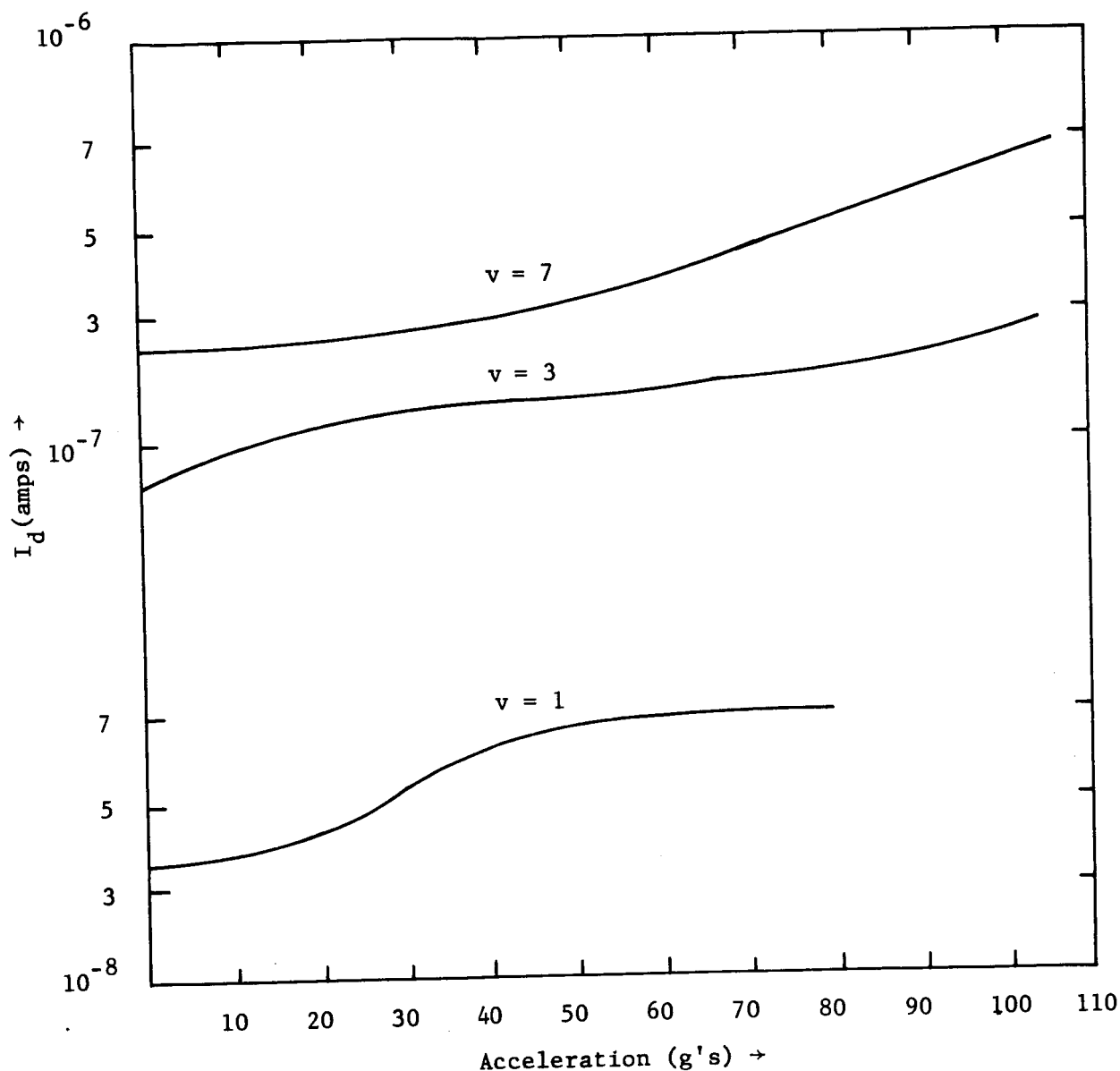
Fig. 71.  Calibration Curve of a Laboratory Accelerometer, Reverse Biased, RTI No. 6.

Table IV is a chart containing most of the desirable and undesirable characteristics of several existing types of accelerometers [46].  Characteristics of an accelerometer based on the piezojunction effect are also included in the chart.  It can be seen from this chart that the overall characteristics of the piezojunction accelerometer surpasses most other types of accelerometers, especially in the area of frequency response.

Table IV

Accelerometer Characteristics Comparison Chart

| Type | Output | Static | Dynamic | Excitation |
|------|--------|--------|---------|------------|
| Capacitance | Low<br>(ac - AM) | Yes | Yes | ac, HF |
| Differential Transformer | High<br>(ac - AM) | Yes | Yes | ac |
| Inductive | High<br>(ac - AM) | Yes | Yes | ac |
| Photoelectric | High<br>(dc or ac AM) | Yes | Yes | dc and Light Source |
| Piezoelectric | High<br>(ac - AM) | No | Yes | None |
| Potentiometric | High<br>(dc or ac - AM) | Yes | Yes | dc or **ac** |
| Strain Gage | Med<br>(dc or ac - AM) | Yes | Yes | dc or ac |
| Vibration | Med<br>(ac - AM) | No | Yes | dc |
| Velocity | High<br>(ac - FM) | No | Yes | None |
| Piezojunction | High<br>(dc or ac - FM) | Yes | Yes | dc |

Table IV

Accelerometer Characteristics Comparison Chart

| Frequency Response | Sensitivity | Range | Displacement | Temperature Sensitivity | Construction Characteristics |
|---|---|---|---|---|---|
| Med | Low | Wide | Small | Low | Large, rugged |
| Low | Low | Limited | Large | Low | Large, rugged |
| Low | Low | High | Large | Low | Large, rugged |
| Low | High | Low | Large | High | Large, fragile, Instable |
| High | Low | Wide | Very Small | High | Small, rugged |
| Low | High | Wide | Large | Low | Relatively small, not rugged, noisy. |
| High | Low | Low | Small | Med | Small, rugged |
| Med | Low | High | Large | Med | Small, rugged |
| Med | High | Limited | Large | High | Rugged |
| Very High | High | Wide | Very Small | High | Small |

# Chapter VII

## CONCLUSIONS

A theory of the effect of a general strain on the electrical characteristics of p-n junctions was developed. The model is based on the deformation potential theory of semiconductors, i.e., the change in the energy band structure with strain. The energy band structure of germanium and silicon was reviewed and the necessary deformation potential theory developed. Energy band changes with strain were incorporated into the current-voltage p-n junction equations. Equations were developed which describe the current-voltage characteristics of diodes and transistors under strain. The diode and transistor model as developed neglected the effects of strain on such junction parameters as effective mass, mobility and carrier lifetime.

Comparing the theoretical model with experimental data shows that there is good agreement. Quantitative comparisons have not been made in cases where the stress was applied by an indentor point. When stress was introduced in the junction by a spherical needle, the calculations for the strain tensor, in which accuracy is needed, was difficult if not impossible. This distributed strain problem was not considered here. As demonstrated by the experimental data, the theory can be used to predict the electrical characteristics of diodes and transistors under strain. As an example, theory predicted that a [100] oriented junction in silicon would

(130)

be more sensitive to strain than a [110] or [111] orientation and a [110] orientation would be more sensitive than a [111] orientation. This was found to be correct experimentally. Theory also predicted that a [111] orientation would be more sensitive in germanium than a [110] or [100] orientation and a [110] more sensitive than a [100] orientation.

The present theory explains many of the facets of the piezojunction phenomenon as observed in silicon and germanium p-n junction devices. This theory and experimental data was used to develop a working laboratory accelerometer. The major problem encountered in this development work was the actual application of stress to the junction device. The introduction and development of a silicon needle stress and strain sensor alleviated this problem. Accelerometers based on the piezojunction effect were shown to possess several advantages over existing acceleration measuring techniques especially in the area of high frequency response.

When observed in multijunction devices such as four-layer diodes, the piezojunction effect was found to have the potential of directly converting mechanical stress into a frequency modulated electrical signal. This feature makes the phenomenon especially applicable to space vehicle instrumentation systems which use pulse code modulated digital data acquisition techniques.

The piezojunction phenomenon is not only applicable to the measurement of acceleration, but to a host of measurements associated with stress, strain, force, pressure, and small displacements. Thus, it is concluded that the piezojunction effect is feasible as a means of measuring acceleration and is a definite state-of-the-art advancement in the field of stress transduction.

## Appendix A

## NOTATION USED TO REPRESENT STRESS AND STRAIN AND
## CALCULATIONS FOR SEVERAL CRYSTAL ORIENTATIONS

In all cases the stress and strain are referred to the crystal axes; x = 1,2,3 refer to the [100], [010] and [001] directions respectively. Tensional stresses and strains are positive and compressional are negative. The mechanical stress, $\sigma$, is represented as follows:

$$\sigma_{\alpha\beta} = \text{conventional stress} \quad ; \quad \alpha,\beta = x,y,z$$

$$\sigma_{ij} = \text{tensor stress} \quad ; \quad i,j = 1,2,3$$

$$\sigma_r = \text{engineering stress} \quad ; \quad r = 1,2,3,4,5,6$$

where $\sigma_{\alpha\beta} = \sigma_{\beta\alpha}$ and $\sigma_{ij} = \sigma_{ji}$. The conventional, tensor and engineering stresses are related as follows:

| Principal | Shear |
|-----------|-------|
| $\sigma_{xx} = \sigma_{11} = \sigma_1$ | $\sigma_{xy} = \sigma_{12} = \sigma_6$ |
| $\sigma_{yy} = \sigma_{22} = \sigma_2$ | $\sigma_{xz} = \sigma_{13} = \sigma_5$ |
| $\sigma_{zz} = \sigma_{33} = \sigma_3$ | $\sigma_{yz} = \sigma_{23} = \sigma_4$ |

The hydrostatic stress, P, is defined in terms of the principal stresses as

$$P = (\sigma_1 + \sigma_2 + \sigma_3)/3$$

The mechanical strain is represented as

$e_{\alpha\beta}$ = conventional strain  ;  $\alpha, \beta$ = z,y,z

$\epsilon_{ij}$ = tensor strain  ;  $i,j$ = 1,2,3

$e_r$ = engineering strain  ;  $r$ = 1,2,3,4,5,6

where $e_{\alpha\beta} = e_{\beta\alpha}$ and $\epsilon_{ij} = \epsilon_{ji}$. The conventional, tensor and engineering strains are related to each other in the following manner:

|  | Principal |  | Shear |
|---|---|---|---|
|  | $e_{xx} = \epsilon_{11} = e_1$ |  | $e_{xy} = 2\epsilon_{12} = e_6$ |
|  | $e_{yy} = \epsilon_{22} = e_2$ |  | $e_{xz} = 2\epsilon_{13} = e_5$ |
|  | $e_{zz} = \epsilon_{33} = e_3$ |  | $e_{yz} = 2\epsilon_{23} = e_4$ |

The hydrostatic strain, e, is defined as

$$e = e_1 + e_2 + e_3$$

For the case of cubic symmetry, the engineering stress is related to strain by Hook's generalized law

$$\begin{bmatrix} \sigma_1 \\ \sigma_2 \\ \sigma_3 \\ \sigma_4 \\ \sigma_5 \\ \sigma_6 \end{bmatrix} = \begin{bmatrix} c_{11} & c_{12} & c_{12} & 0 & 0 & 0 \\ c_{12} & c_{11} & c_{12} & 0 & 0 & 0 \\ c_{12} & c_{12} & c_{11} & 0 & 0 & 0 \\ 0 & 0 & 0 & c_{44} & 0 & 0 \\ 0 & 0 & 0 & 0 & c_{44} & 0 \\ 0 & 0 & 0 & 0 & 0 & c_{44} \end{bmatrix} \times \begin{bmatrix} e_1 \\ e_2 \\ e_3 \\ e_4 \\ e_5 \\ e_6 \end{bmatrix} ,$$

and

$$
\begin{bmatrix} e_1 \\ e_2 \\ e_3 \\ e_4 \\ e_5 \\ e_6 \end{bmatrix} = \begin{bmatrix} s_{11} & s_{12} & s_{12} & 0 & 0 & 0 \\ s_{12} & s_{11} & s_{12} & 0 & 0 & 0 \\ s_{12} & s_{12} & s_{11} & 0 & 0 & 0 \\ 0 & 0 & 0 & s_{44} & 0 & 0 \\ 0 & 0 & 0 & 0 & s_{44} & 0 \\ 0 & 0 & 0 & 0 & 0 & s_{44} \end{bmatrix} \times \begin{bmatrix} \sigma_1 \\ \sigma_2 \\ \sigma_3 \\ \sigma_4 \\ \sigma_5 \\ \sigma_6 \end{bmatrix} ,
$$

where the c's and s's are the stiffness and compliance coefficient for the crystal.

When a general stress is applied to a crystal, it is always possible to choose a rectangular coordinate system (not necessarily the crystal axes) such that there is zero shear stress and three principal stresses. Let the principal stress system have the coordinates $x'$, $y'$, $z'$, the shear stresses are then $\sigma_{x'y'} = \sigma_{x'z'} = \sigma_{y'z'} = 0$. The principal stresses are related to the crystal axes by the following equation.

$$
\begin{aligned}
\sigma_{xx} &= \sigma_{x'x'} \ell_1^2 + \sigma_{y'y'} \ell_2^2 + \sigma_{z'z'} \ell_3^2 \\
\sigma_{yy} &= \sigma_{x'x'} m_1^2 + \sigma_{y'y'} m_2^2 + \sigma_{z'z'} m_3^2 \\
\sigma_{zz} &= \sigma_{x'x'} n_1^2 + \sigma_{y'y'} n_2^2 + \sigma_{z'z'} n_3^2 \\
\sigma_{xy} &= \sigma_{x'x'} \ell_1 m_1 + \sigma_{y'y'} \ell_2 m_2 + \sigma_{z'z'} \ell_3 m_3 \\
\sigma_{xz} &= \sigma_{x'x'} \ell_1 n_1 + \sigma_{y'y'} \ell_2 n_2 + \sigma_{z'z'} \ell_3 n_3 \\
\sigma_{rz} &= \sigma_{x'x'} m_1 n_1 + \sigma_{y'y'} m_2 n_2 + \sigma_{z'z'} m_3 n_3
\end{aligned}
$$

where $\ell, m, n$ are the direction cosines defined by the following transformation.

$$
\begin{bmatrix} x \\ y \\ z \end{bmatrix} = \begin{bmatrix} \ell_1 & m_1 & n_1 \\ \ell_2 & m_2 & n_2 \\ \ell_3 & m_3 & n_3 \end{bmatrix} \times \begin{bmatrix} x' \\ y' \\ z' \end{bmatrix}
$$

It is of practical interest here to determine the strain components for hydrostatic, uniaxial [100], uniaxial [011] and uniaxial [111] stresses. For the hydrostatic case,

$$\sigma_1 = \sigma_2 = \sigma_3 = -P$$

and

$$\sigma_4 = \sigma_5 = \sigma_6 = 0 \ .$$

Solving for the strains yields

$$e_1 = e_2 = e_3 = -(s_{44} + 2s_{12})P \ ,$$
$$e_4 = e_5 = e_6 = 0 \ .$$

Consider a uniaxial compressional stress of magnitude T applied along the [111] direction. In this case $\ell_1 = m_1 = n_1 = 1/\sqrt{3}$ , for which

$$\sigma_1 = \sigma_2 = \sigma_3 = \sigma_4 = \sigma_5 = \sigma_6 = -\ T/3 \ ,$$

and

$$e_1 = e_2 = e_3 = -\ T(s_{11} + 2s_{12})/3 \ ,$$
$$e_4 = e_5 = e_6 = -\ T\ s_{44}/3 \ .$$

Next consider a uniaxial compression stress of magnitude T applied along the [011] direction. In this case $\ell_1 = 0$, $m_1 = 1/\sqrt{2}$ , $n_1 = 1/\sqrt{2}$ for which

$$\sigma_1 = 0 \ , \ \sigma_2 = \sigma_3 = -\ T/2 \ , \ \sigma_4 = -\ T/2 \ , \ \sigma_5 = \sigma_6 = 0 \ ,$$

and

$$e_1 = -s_{12}T \ , \ e_2 = e_3 = -\ T(s_{11} + s_{12})/2 \ ,$$

$$e_4 = - T \, s_{44}/2 \; , \; e_5 = e_6 = 0 \; .$$

Finally consider a uniaxial compression stress of magnitude T applied along the [100] direction. This gives $\ell_1 = 1$ , $m_1 = 0$ , $n_1 = 0$ for which

$$\sigma_1 = - T \; , \; \sigma_2 = \sigma_3 = \sigma_4 = \sigma_5 = \sigma_6 = 0,$$

and

$$e_1 = -s_{11} \, T \; , \; e_2 = e_3 = -s_{12} \, T \; ,$$
$$e_4 = e_5 = e_6 = 0 \; .$$

Appendix B

EFFECT OF STRAIN ON THE EFFECTIVE MASS

B.1  Introduction

There is little experimental information available on the effect of large strains ($e_s > 1\%$) on the effective mass.  Cyclotron resonance measurements of the effective mass have been made on silicon subjected to uniaxial stress in which the strain levels were less than 1% [19,20,37].  In these experiments the effective mass was found to change only a few percent. Hasegawa [38] and Hensel and Hasegawa [19] have derived theoretical expressions for the effective mass of some of the energy levels in silicon as a function of some particular stresses.  By using the results of their work it can be shown that strain in the range of interest here ($e_s < 5\%$) produces a negligible change in the effective mass of silicon when compared to changes in carrier concentration.

B.2  Effective Mass of Holes in Silicon

The shape of the energy bands at the band edge points determines the effective mass, i.e.,

$$m^*_{ij} = \frac{1}{\hbar^2}[\frac{\partial^2 E(k)}{\partial k_i \partial k_j}]^{-1} , \tag{B.1}$$

(138)

where $m_{ij}^*$ is the effective mass tensor and i and j are the $\bar{k}$-directions. In the case of spherical bands, $E \propto [k_x^2 + k_2^2 + k_3^2]/m^*$, the effective mass, $m^*$, is independent of direction. Such is the case for the split-off hole band ($E_{v3}$) in silicon and germanium. The light hole band ($E_{v2}$) can be approximated to within a few percent by a sphere [11]. The heavy hole band ($E_{v1}$) is a warped sphere. It can also be approximated with less accuracy as a sphere with a radius equal to the average radius of the warped sphere [11]

As discussed in Chapter II, when the crystal is mechanically strained the degeneracy of the $\Gamma_{25}'(j = 3/2)$ is removed. Strain causes the warped spheres to transform into ellipsoids similar to that encountered in the conduction bands of Si and Ge [38]. Hasegawa [38] has developed a theoretical expression for the energy of the heavy hole band as a function of $\bar{k}$ and the magnitude of a uniaxial compression stress applied along the $\langle 100 \rangle$ axes of the crystal:

$$E_{v1} = (A - \frac{1}{2} BZ)k_{\parallel}^2 + (A + BZ)k_{\perp}^2 , \qquad (B.2)$$

where $k_{\parallel}$ is parallel to the $\langle 100 \rangle$ direction and $k_{\perp}$ is perpendicular to the $\langle 100 \rangle$ direction, A and B are constants which can be determined experimentally and Z is the degree of mixing between the heavy hole band and the split-off band and is given by

$$Z = \frac{1}{2}(1 + \frac{1 - 9x}{(1 - 2x + 9x^2)^{1/2}}) \qquad (B.3)$$

where

$$x = \frac{e_1 D_u}{\delta} , \qquad (B.4)$$

$\delta$ is the separation between the heavy hole band and the split-off band (see Fig. 3).

Solving Eqs. (B.1) and (B.2) for the components of the effective mass tensor gives

$$\frac{\hbar^2}{2m_{\parallel}} = A - \frac{1}{2} BZ \qquad (B.5)$$

and

$$\frac{\hbar^2}{2m_{\perp}} = A + BZ . \qquad (B.6)$$

A "density of states effective mass", $m_c$, can now be defined in the same manner as is done for the conduction band, i.e.

$$(m_c)^{3/2} = \sqrt{m_{\perp}^2 \, m_{\parallel}} . \qquad (B.7)$$

Hensel and Feber [37] have determined experimental values of A, B, and $D_u$ as follows:

$$A = -4.28 \, \hbar^2/2m_o ,$$
$$B = -0.75 \, \hbar^2/2m_o , \qquad (B.8)$$
$$D_u = 2.04 \text{ ev} .$$

Solving the above equations for the density of states effective mass as a function of strain shows that $m_c$ changes less than 1% for stress levels as large as $6 \times 10^{10}$ dyne/cm$^2$. This change is negligible when compared to changes in the carrier concentration for the same stress.

The effective mass can also be obtained from the theory of Hasegawa [38] as a function of other uniaxial stresses ([011] and [111]). Changes in the density of states effective mass for these directions are also found to be very small.

## B.3 Effective Mass of Electrons in Silicon

The Hamiltonian for the conduction electrons has been discussed in Chapter II, Eq. (2.8). Diagonalizing the Hamiltonian gives

$$E(\bar{k}) = \frac{\hbar^2}{2m_{\parallel}} \kappa_x^2 + \frac{1}{2m_{\perp}}(k_y^2 + k_z^2) + [\,]_d \, e + [\,]_u \, e_1$$
$$\pm [\hbar^2 v^2 \kappa_x^2 + ([\,]_u' \, e_4 + N \, k_y \, k_z)^2]^{1/2} \,. \tag{B.9}$$

The band edge point along the [100] axis has already been shown to be located at

$$\hbar^2 (\kappa_x)_{min}^2 = \hbar^2 \kappa_o^2 - \frac{([\,]_u' \, e_4)^2}{v^2} \,, \tag{B.10}$$

$$\hbar^2 k_y^2 = 0 \,,$$

$$\hbar^2 k_z^2 = 0 \,.$$

It can be seen from Eq. (B.9) that constant energy surfaces are not ellipsoids or spheres in k-space when there is an applied strain. If one wants the density of states exactly, it would be necessary to use Eq. (B.9) for $E(\bar{k})$ in the density of states relationship. To do this would require considerable effort which is probably unwarranted. An approximate approach is to expand $E(\bar{k})$ in a Taylor series about the band edge point. Performing this expansion to second order powers in $\bar{k}$ yields;

$$E(\bar{k}) = \delta_e + \frac{\hbar v}{\kappa_o^3}(\kappa_x)_{min}^2 [\kappa_x - (\kappa_x)_{min}]^2 + \hbar^2 (\frac{k_y^2 + k_z^2}{2m}) + \alpha \, e_4 \, k_y \, k_z \,, \tag{B.11}$$

where $\delta_e$ represents the shift of the band edge and

$$\alpha = \frac{2N[\ ]'_u}{-\Delta E} \ . \qquad (B.12)$$

This approach has been taken by Hensel and Hasegawa [19] and they find that $\alpha$ is given approximately by

$$\alpha \approx \frac{2[\ ]'_u}{-\Delta E} \frac{1}{m_o}(\frac{m_o}{m_1} - 1) \qquad (B.13)$$

An analysis of Eq. (B.10) shows that as $e_4 \longrightarrow \Delta E/2[\ ]'_u$, $(\kappa_x)_{min} \longrightarrow 0$.
This means that $E(\bar{k})$ becomes independent of $\kappa_x$ to second order powers in
$\kappa_x$ for the strain level. Therefore one would not expect Eq. (B.11) to hold
near this strain level. For strains below the above critical value Eq. (B.11)
is expected to be a good approximation.

Taking the derivatives of Eq. (B.11) and solving for the components
of the effective mass tensor yields:

$$\frac{1}{m^*_{ij}} = \begin{bmatrix} \frac{1}{m_{||}}[1 - (2[\ ]'_u/\Delta E)^2 e_4^2 & 0 & 0 \\ 0 & \frac{1}{m_{\perp}} & \alpha e_4 \\ 0 & \alpha e_4 & \frac{1}{m_{\perp}} \end{bmatrix} \qquad (B.14)$$

as expected there are terms in the tensor which are non-zero for the off
diagonal elements. This is handled in the usual manner (diagonalizing the
tensor) which yields

$$\frac{1}{m^*_{k1}} = \begin{bmatrix} \dfrac{1}{m_1(e)} & 0 & 0 \\ 0 & \dfrac{1}{m_2(e)} & 0 \\ 0 & 0 & \dfrac{1}{m_3(e)} \end{bmatrix} = \begin{bmatrix} \dfrac{1}{m_{||}}[1 - (\dfrac{2[]'_u}{\Delta E})^2 e^2_4] & 0 & 0 \\ 0 & \dfrac{1}{m_\perp}(1+m_\perp \alpha e_4) & 0 \\ 0 & 0 & \dfrac{1}{m_\perp}(1-m_\perp \alpha e_4) \end{bmatrix} . \text{(B.15)}$$

where k and l are different from i and j and are used to show that the new coordinate system is different from the old x, y, z system.

The inverse density of states effective mass is

$$\left(\frac{1}{m^*_c(e)}\right)^3 = \frac{1}{m_1(e)}\frac{1}{m_2(e)}\frac{1}{m_3(e)} . \tag{B.16}$$

Rewriting Eq. (B.16) in terms of the strain gives

$$\left(\frac{m^*_c(e)}{m^*_c(o)}\right)^3 = \frac{1}{[1 - (2[]'_u/\Delta E)^2 e^2_4][1 - m^2\alpha^2 e^2_4]} , \tag{B.17}$$

where $m^*_c(o)$ is the unstrained effective mass. Using the experimental value [19] $\alpha m_o = 16.4$ and substituting into Eq. (B.17) the values of the other band parameter gives

$$\left(\frac{m^*_c(e)}{m_c(o)}\right)^3 = \frac{1}{(1 - 520\ e^2_4)\ (1 - 268\ e^2_4)} . \tag{B.18}$$

Referring to Eq. (B.17) it is seen that there are two singularities in the effective mass equation. This is not unexpected since the energy was expanded in a Taylor series and accounts only for second order power in $\bar{k}$. It is seen that, in fact, if the shear strain is less than about 2 percent,

there is a negligible effect on the effective mass. In the case of hydro-static pressures the shear is zero and hence the effective mass is independent of strain.

B.4   Summary

The above treatment of the variation of effective mass with strain for silicon is by no means complete. It does however indicate that for strain levels below a few percent, effective mass changes are negligible. Although no treatment has been given for germanium, it is expected that germanium will behave similarly to silicon. More important than the preceding discussion is the fact that experimental measurements made on the electrical parameters of p-n junction devices subjected to mechanical stress indicate that effective mass variations are at least second order when compared to carrier density variations.

## Appendix C

### EFFECT OF STRAIN ON THE MINORITY CARRIER LIFETIME, CARRIER MOBILITIES, DIFFUSION CONSTANTS AND DIFFUSION LENGTHS

C.1 Minority Carrier Lifetime[*]

The minority carrier lifetime of a semiconductor, based on a single trap level located in the forbidden band [33], is given by [39]

$$\tau = \frac{\tau_{po}(n + n_1) + \tau_{no}(p + p_1)}{n + p} \qquad (C.1)$$

where n and p are the respective electron and hole concentrations in the particular semiconductor. $\tau_{po}$ and $\tau_{no}$ are the lifetimes of holes and electrons in highly n- and p-type materials respectively. Both $\tau_{po}$ and $\tau_{no}$ are inversely proportional to the trap density [39]. $n_1$ and $p_1$ in Eq. (C.1) are given by [33].

$$n_1 = n_i \exp[(E_i - E_t)/kT] , \qquad (C.2)$$

$$p_1 = n_i \exp[(E_t - E_i)/kT] , \qquad (C.3)$$

where $E_t$ is the energy of the trap level and $E_i$ is the energy of the intrinsic Fermi level.

---

[*] The present treatment of minority carrier lifetime is closely related to the treatment of generation recombination current given in Appendix E.

(145)

It is seen from Eq. (C.1) that if the material is highly n- or p-type, the lifetime expression reduces to either $\tau_{po}$ or $\tau_{no}$. Any changes in the latter two quantities can be neglected, based on the arguments presented in Sect. 3.3; namely, the density of generation-recombinations centers is not changed by strain. The capture cross section is assumed to remain constant. The lifetimes, $\tau_n$ and $\tau_p$, which appear in the theory of the "ideal" junction current are the lifetimes of electrons at the edge of the depletion region on the p side of the junction and of the holes at the edge of the depletion region on the n side of the junction respectively. It will be assumed for the present purposes that the material at the edges of the depletion regions is doped heavily enough so that the lifetimes are independent of the carrier concentrations n, p, $n_1$ and $p_1$. The effects of strain induced changes in the lifetime of carriers inside the depletion region are accounted for in the theory of generation-recombination currents (see Appendix E and Sect. 3.3).

Matukura [40] has measured the lifetime of minority carriers in stressed and unstressed silicon p-n junctions. He found that the lifetime decreased 10 to 30 percent for the stressed diodes. In his experiments a diamond needle was used to introduce a high stress level over a small region of the p-n junction area. The lifetime was measured by first injecting minority carriers with a large forward biased current pulse. Following the current pulse, the decay time was measured. The unstrained lifetime was found to be 0.3 $\mu$-seconds. Assuming that the change in the decay time with the application of strain is due to a change in the lifetime of carriers in the strained area only, it is found that the lifetime in the strained material is reduced to $10^{-13}$ $\mu$-seconds! Physically, this

value is not acceptable. The results of this experiment can be explained by neglecting changes in lifetime in favor of energy band changes.

## C.2 Mobility

Much work has been done on the piezoresistance properties of germanium and silicon [41,42,43,44,45,46]. This work, however, has been concerned mainly with low strain, i.e., strain levels low compared to the levels of interest here. The piezoresistance effect in many-valley semiconductors (n-type Ge and Si) is explained by the deformation potential theory [41,42]. The major effect has been found to result from the relative population and depopulation of the valleys in the conduction band with strain as discussed in Chapters II and III.

For low strain levels, the relative change in the resistivity of germanium and silicon has been found to be directly proportional to strain. The proportionality constant or elastoresistance coefficient is on the order of 175 for extrinsic silicon and -150 for extrinsic germanium [43] For silicon this gives

$$\frac{\Delta\mu}{\mu} \sim 175 \ S \tag{C.4}$$

where $\mu$ is the mobility of the majority carriers and S is the strain. The relative change in mobility is seen to have a small effect compared to that of minority carrier changes.

It is the minority carrier mobility that is of interest here. It will be assumed that changes in the minority carrier mobility are of the same order of magnitude as that for majority carriers. This is probably

a good assumption since the majority carrier mobility changes mainly due to
relative changes in the density of carriers at the band edge points while
for minority carriers the density of the carriers are small to begin with
and therefore would have less influence on the mobility.

It should also be noted that the relative change in resistance
tends to saturate below the strains of interest here. This comes about
because relatively small changes in the energy levels cause all the majority
carriers to occupy certain valleys while leaving the other valleys empty.
Strains above those required to empty the valleys have little effect on
the mobility.

## C.3 Diffusion Coefficients

The minority carrier diffusion coefficients are directly proportional
to the minority carrier mobilities ($D = \mu kT/q$). As discussed in Sect. C.2
above, the minority carrier mobility is expected to be relatively insensitive
to strain--especially when compared to minority carrier density changes.
Changes in the diffusion coefficients with strain are therefore expected to be
negligible.

## C.4 Diffusion Length

The diffusion lengths $L_p$ and $L_n$ are proportional to the square root
of $\mu_p \tau_p$ and $\mu_n \tau_n$ respectively. Changes with strain of both mobility and
lifetime have been discussed above and it was concluded that the changes
were negligible compared to other parameter changes. Another effect arises
due to the changing energy levels which produce a "quasielectric" field

acting on the minority carrier [47]. This means that an effective diffusion length must be used which includes the drift field effect. The "quasielectric" field will have an effect similar to a built-in electric field. The field is directly proportional to the band gap changes and thus directly proportional to strain. These linear changes will be neglected compared to the exponential changes of the minority carrier density.

## Appendix D

## EFFECT OF LARGE STRAINS ON CONDUCTIVITY

Most of the piezoresistance work which was cited in Appendix C has been concerned with conductivity and resistivity changes as a function of strain. Again this work has been for low strain levels in extrinsic material such that the carrier density was determined by the impurity density and was independent of strain. As pointed out in Chapter III, the minority carrier density in extrinsic material can change by several orders of magnitude for large strain levels. Also in intrinsic material both the hole and electron densities can change with strain.

For the present purposes it will be assumed that mobility is independent of strain. The conductivity is

$$\sigma = nq\mu_n + pq\mu_p .$$

(D.1)

For the case of intrinsic material ($n \simeq p$) the conductivity expression reduces to

$$\sigma = nq(\mu_n + \mu_p) .$$

(D.2)

From Eqs. (3.11) and (3.12)

$$pn = n_{io}^2 \, \gamma_v(e) = n^2 .$$

(D.3)

(150)

The conductivity then reduces to

$$\sigma(e) = n_{io}q \sqrt{\gamma_v(e)} \ , \qquad \qquad (D.4)$$

or

$$\frac{\sigma(e)}{\sigma(o)} = \sqrt{\gamma_v(e)} \ . \qquad \qquad (D.5)$$

Since $\gamma_v(e)$ can change by orders of magnitude with high strain levels, the conductivity of intrinsic material can also change by orders of magnitude.

In the case of extrinsic material, p-type for example, the hole density is approximately equal to $N_A$. Substituting this into Eqs. (D.1) and (D.3) gives

$$\sigma = \frac{n_{io}^2}{N_A} q\mu_n \ \gamma_v(e) + N_A \ q\mu_p \ . \qquad \qquad (D.6)$$

The conductivity is then expected to change with strain in extrinsic material when $n_{io}^2 \ \gamma_v(e)$ approaches the same order of magnitude as $N_A$.

Large changes in the conductivity of near intrinsic germanium have been observed for large strain levels by Graham, Jones and Holland [48]. In their experiments very large strains were set up in the sample by shock waves.

Appendix E

SPACE CHARGE GENERATION-RECOMBINATION
CURRENT IN P-N JUNCTIONS

Space charge generation-recombination current can be important in
p-n junctions (particularly in silicon) [33]. This current adds to the
"ideal" or diffusion current which is predicted by the Shockley theory.
In a p-n junction in which there is a single trap level located in the
forbidden band, the steady state recombination rate U for holes or electrons
is [33].

$$U = \frac{pn - n_i^2}{\tau_{no}(p + p_1) + \tau_{po}(n + n_1)} \quad , \quad \text{(E.1)}$$

where $p_1$ is the density of holes in the valence band when the Fermi level
falls at the trap level, $n_1$ is the density of electrons in the conduction
band when the Fermi level falls at the trap level, $\tau_{no}$ is the lifetime for
electrons injected into highly p-type material, and $\tau_{po}$ is the lifetime for
holes injected into highly n-type material. Hauser [34,49] has treated this
problem and has obtained an approximate solution for the generation-
recombination current. The discussion to follow is a review of his work.

The hole and electron currents are given by

$$J_p = q\mu_p pE - qD_p dp/dx \quad . \quad \text{(E.2)}$$

and

$$J_n = q\mu_n nE + qD_n dn/dx \ , \tag{E.3}$$

where E is the electric field at x. The continuity equations for steady state are

$$0 = -U - \frac{1}{q}\frac{dJ_p}{dx} \tag{E.4}$$

and

$$0 = -U + \frac{1}{q}\frac{dJ_n}{dx} \tag{E.5}$$

Figure 72 is a sketch of the junction which shows the two regions (n and p) and the space charge region where the width of the space charge region is W. Integrating Eqs. (E.4) and (E.5) over the space charge region gives

$$J_p(W) = J_p(0) - q \int_o^W U \ dx \tag{E.6}$$

and

$$J_n(0) = J_n(W) + q \int_o^W U \ dx \tag{E.7}$$

The total current density is obtained by adding the hole current density and the electron current density at any point x, for example x = 0. This gives

$$J = J_n(0) + J_p(0) = J_n(0) + J_p(W) + q \int_o^W U \ dx \tag{E.8}$$

or

$$J = J_I + J_U \ , \tag{E.9}$$

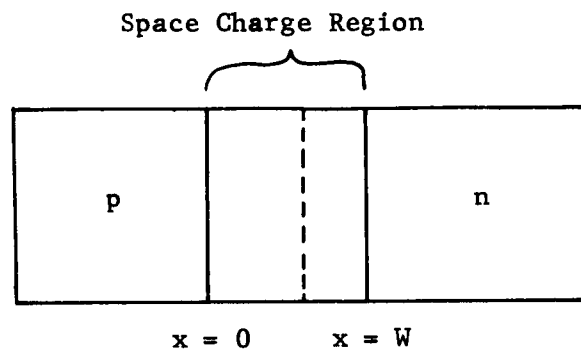Fig. 72. Generation-Recombination Junction Model.

where $J_I$ is the "ideal" or diffusion current density and $J_U$ is the generation-recombination current density given by

$$J_U = q \int_o^W U \, dx \qquad (E.10)$$

In the space charge region $J_p$ and $J_n$ are small compared to the drift and diffusion terms which reduces Eqs. (E.2) and (E.3) to:

$$\mu_p pE \simeq D_p dp/dx \qquad (E.11)$$

and

$$-\mu_n nE \simeq D_n dn/dx \ . \qquad\qquad (E.12)$$

Using Einstein's relation ($D = \mu kT/q$) and solving Eqs. (E.11) and (E.12) for the hole and electron densities gives

$$p \approx C_1 \exp[-qV/kT] \qquad\qquad (E.13)$$

and

$$n \approx C_2 \exp[qV/kt] \ . \qquad\qquad (E.14)$$

It can be shown that [49]

$$pn \approx n_i^2 \exp[qV_a/kT] \ , \qquad\qquad (E.15)$$

where $V_a$ is the applied junction voltage.

Substituting Eqs. (E.1) and (E.15) into Eq. (E.10) gives

$$J_U = q \ n_i^2 [\exp\{qV_a/kT\} - 1] \int_o^W \frac{dx}{\tau_{no}(p + p_1) + \tau_{po}(n + n_1)} \ . \qquad (E.16)$$

An explicit evaluation of the integral is not possible because the hole and electron densities are a function of the applied voltage. Several important cases can be analyzed however. First, consider the case for large reverse bias such that $qV_a/kT \ll 1$. In this case $p \ll p_1$ and $n \ll n_1$. Integrating Eq. (E.16) gives

$$J_U = \frac{-q \ n_i^2 \ W}{\tau_{no} \ p_1 + \tau_{po} \ n_1} \ . \qquad\qquad (E.17)$$

The width of the space charge region W in Eq. (E.17) is a function of the applied voltage $V_a$.

For the case of a step junction

$$W = W_o (1 - V_a/V_o)^{1/2} \ , \tag{E.18}$$

where $W_o$ is the width of the space charge region with zero applied voltage and $V_o$ is the built-in junction potential.

A second case of interest is for large forward bias such that $qV_a/kT \gg 1$, for which

$$p \approx n = n_i \, \exp\{qV_a/2kT\} \ , \tag{E.19}$$

where $p \gg p_1$ and $n \gg n_1$. Under these conditions the generation-recombination current density becomes

$$J_U = \frac{q \, n_i}{\tau_{no} + \tau_{po}} \, W \, \exp\{qV_a/2kT\} \ . \tag{E.20}$$

Again $W$ is a function of the applied voltage.

The third case which can be solved is the small forward bias case such that $p \ll p_1$ and $n \ll n_1$ for which

$$J_U = \frac{q \, n_i^2 \, W}{\tau_{no} \, p_1 + \tau_{po} \, n_1} \, [\exp\{qV_a/kT\} - 1] \ . \tag{E.21}$$

The above three special cases are of particular interest; however, it would be desirable to obtain a solution which is valid for all values of applied voltage. Although Eq. (E.16) cannot be solved in general, limits can be established on the current density. Consider the denominator of the integral term of Eq. (E.16)

$$f(V) = \tau_{no}(p + p_1) + \tau_{po}(n + n_1) \ , \tag{E.22}$$

where

$$p = p_n \exp\{qV/kT\} \qquad \text{(E.23)}$$

and

$$n = n_n \exp\{-qV/kT\} \qquad \text{(E.24)}$$

where p and n are the hole and electron densities in the junction at the point where the voltage is V and $p_n$ and $n_n$ are the densities on the n-side of the junction. The function f(V) has a minimum value for some value of voltage V. The minimum can be found in the usual manner, i.e.

$$\frac{\partial f(V)}{\partial V} = 0 = \tau_{no} \, p_n \, \frac{q}{kT} \exp\{qV/kT\} - \tau_{po} \, n_n \, \frac{q}{kT} \exp\{-qV/kT\} \qquad \text{(E.25)}$$

or

$$\exp\{qV/kT\} = \left(\frac{\tau_{po}}{\tau_{no}} - \frac{n_n}{p_n}\right)^{1/2} . \qquad \text{(E.26)}$$

Therefore

$$f(V) \geq \tau_{no}\left\{\sqrt{n_n p_n} \, \sqrt{\tau_{po}/\tau_{no}} + p_1\right\} + \tau_{po}\left\{\sqrt{n_n p_n} \, \sqrt{\tau_{no}/\tau_{po}} + n_1\right\} \qquad \text{(E.27)}$$

or

$$f(V) \geq (\tau_{no}p_1 + \tau_{po}n_1) + \sqrt{\tau_{po}\tau_{no}} \, n_i \, \exp\{qV_a/2kT\} \qquad \text{(E.28)}$$

Substituting Eq. (E.27) into (E.16) and integrating gives

$$J_U \leq \frac{q \, n_i^2 \, W}{(\tau_{no}p_1 + \tau_{po}n_1)} \frac{[\exp\{qV_a/kT\} - 1]}{1 + \dfrac{\sqrt{\tau_{po}\tau_{no}} \, n_i \, \exp\{qV_a/2kT\}}{(\tau_{no}p_1 + \tau_{po}n_1)}} \qquad \text{(E.29)}$$

An inspection of Eq. (E.29) shows that for large reverse bias the limit is, in fact, equal to the exact value found earlier, Eq. (E.17). For large forward bias Eq. (E.29) becomes

$$J_U \leq \frac{q \, n_i W \exp\{qV_a/2kT\}}{\sqrt{\tau_{po}\tau_{no}}} \; . \tag{E.30}$$

By comparing Eq. (E.29) with the exact value given in Eq. (E.20), it is found that if $\sqrt{\tau_{po}\tau_{no}}$ is replaced by $(\tau_{po} + \tau_{no})$ then the two equations give the same value. As an approximation the recombination-generation current density is equal to the limiting value given in Eq. (E.29) with $\sqrt{\tau_{no}\tau_{po}}$ replaced by $(\tau_{po} + \tau_{no})$,

$$J_U \simeq \frac{q \, n_i^2 \, W[\exp\{qV_a/kT\} - 1]}{(\tau_{no}P_1 + \tau_{po}n_1)\left(1 + \dfrac{(\tau_{no} + \tau_{po}) \, n_i \, \exp\{qV_a/2kT\}}{[\tau_{no}P_1 + \tau_{po}n_1]}\right)} \; . \tag{E.31}$$

Comparing the ratio $(\tau_{po} + \tau_{no})/(\tau_{po}\tau_{no})^{1/2}$ we see that if $\tau_{po} = \tau_{no}$ then the ratio is equal to 2. If however $\tau_{no} = 10\tau_{po}$ the ratio is equal to $11/\sqrt{10} \approx 3$. The error introduced by making the substitution in Eq. (E.30) is then expected to be less than a factor of 2 for $\tau_{po} = \tau_{no}$ and less than 3 for $\tau_{no} = 10\tau_{po}$.

LIST OF REFERENCES

(159)

# LIST OF REFERENCES

[1]  H. Hall, J. Bardeen and G. Pearson, "The Effects of Pressure and Temperature on the Resistance of p-n Junctions in Germanium", Phys. Rev. 84, October 1951, pp. 129-132.

[2]  W. Rindner, "Anisotropic Strain Effects in p-n Junctions", Bull. Am. Phys. Soc. 7, January 1962, pp. 65-66.

[3]  W. Rindner and I. Braun, "Effects of Elastic and Plastic Deformations in p-n Junctions", Bull. Am. Phys. Soc. 7, April 1962, p. 331.

[4]  W. Rindner and I. Braun, "On the Effects of Elastic and Plastic Deformation on p-n Junctions in Semiconductors", Report of the International Conference on the Physics of Semiconductors-Exeter, England, July 1962, The Institute of Physics and the Physical Society, London, 1962, p. 167.

[5]  W. Rindner, "Resistance of Elastically Deformed Shallow p-n Junctions", J. Appl. Phys. 33, August 1962, pp. 2479-2480.

[6]  W. Rindner and I. Braun, "Resistance of Elastically Deformed Shallow p-n Junctions. II.", J. Appl. Phys. 34, July 1963, pp. 1958-1970.

[7]  Y. Matukura, "Some Factors Influencing on the Anisotropic Stress Effect of pn Junctions", Japanese J. Appl. Phys. 3, September 1964, pp. 516-520.

[8]  R. Edwards, "Some Effects of Localized Stress on Silicon Planar Transistors", IEEE Transactions on Electron Devices ED-11, June 1964, pp. 286-294.

[9]  W. G. Pfann, "Improvements of Semiconductor Devices by Elastic Strain", Solid-State Electronics 3, November-December 1961, pp. 261-267.

[10]  M. E. Sikorski, et al., "Transistor Microphone", Rev. Sci. Instr. 33, October 1962, pp. 1130-1131.

[11]  F. Herman, "The Electronic Energy Band Structure of Silicon and Germanium", Proc. IRE 43, December 1955, pp. 1703-1732.

[12]  See reference 1.

[13]  See, for example, L. Mariot, Group Theory and Solid State Physics, Prentice-Hall, Inc., Englewood Cliffs, New Jersey, 1962.

(160)

[14] W. P. Mason and T. B. Bateman, "Ultrasonic Wave Propagation in Doped n-Germanium and p-Silicon", Phys. Rev. 134, June 1964, pp. A1387-A1396.

[15] J. Bardeen and W. Shockley, "Deformation Potentials and Mobilities in Non-Polar Crystals", Phys. Rev. 80, October 1950, pp. 72-80.

[16] C. Herring and E. Vogt, "Transport and Deformation-Potential Theory for Many-Valley Semiconductors with Anisotropic Scattering", Phys. Rev. 101, February 1956, pp. 944-961.

[17] W. H. Kleiner and L. M. Roth, "Deformation Potential in Germanium from Optical Absorption Lines for Exciton Formation", Phys. Rev. Letters 2, April 1959, pp. 334-336.

[18] L. I. Schiff, Quantum Mechanics, McGraw-Hill Book Company, Inc., New York, New York, 1949, p. 144.

[19] J. C. Hensel and H. Hasegawa, "Cyclotron Resonance of Electrons in Uniaxially Stressed Silicon: Energy Bands Near X in the Diamond Structure", (paper presented at the International Conference on the Physics of Semiconductors, Paris, July 1964).

[20] J. C. Hensel, H. Hasegawa and M. Nakayama, "Cyclotron Resonance in Uniaxially Stressed Silicon II: Nature of the Covalent Bond", (to be published).

[21] L. Kleinman, "Deformation Potentials in Silicon. I. Uniaxial Strain", Phys. Rev. 128, December 1962, pp. 2614-2621.

[22] L. Kleinman, "Deformation Potentials in Silicon. II. Hydrostatic Strain and the Electron-Phonon Interaction", Phys. Rev. 130, June 1963, pp. 2283-2289.

[23] I. Goroff and L. Kleinman, "Deformation Potentials in Silicon. III. Effects of a General Strain on Conduction and Valence Levels", Phys. Rev. 132, November 1963, pp. 1080-1084.

[24] W. P. Mason and T. B. Bateman, "Ultrasonic Attenuation and Velocity Changes in Doped n-type Germanium and p-type Silicon and their use in Determining an Intrinsic Electron and Hole Scattering Time", Phys. Rev. Letters 10, March 1963, pp. 151-154.

[25] See reference 14.

[26] P. Csavinsky and N. G. Einspruch, "Effect of Doping on the Elastic Constants of Silicon", Phys. Rev. 132, December 1963, pp. 2434-2440.

[27] J. S. Blakemore, Semiconductor Statistics, Pergamon Press, Inc., New York, New York, 1962, Chaps. 1 and 2.

[28]  W. Paul and D. M. Warschauer, Solids Under Pressure, McGraw-Hill Book
      Company, Inc., New York, New York, 1963, Chap. 8, p. 188.

[29]  J. J. Hall, "Long-Strain Dependence of the Acceptor Binding Energy
      in Germanium", Phys. Rev. 128, October 1962, pp. 68-75.

[30]  W. Kohn, Solid State Physics, Volume 5, F. Seitz and D. Turnbull, eds.,
      Academic Press Inc., New York, New York, 1957.

[31]  See reference 1.

[32]  See, for example, A. Phillips, Transistor Engineering, McGraw-Hill
      Book Company, Inc., New York, New York, 1962, Chap. 3, p. 51.

[33]  C. Sah, R. Noyce and W. Shockley, "Carrier Generation and Recombination
      in P-N Junctions and P-N Junction Characteristics", Proc. IRE 45,
      September 1957, pp. 1228-1243.

[34]  R. F. Tramposch and W. Rindner, "Room Temperature Slip in Ge",
      Appl. Phys. Letters 3, August 1963, pp. 42-43.

[35]  G. L. Pearson and F. L. Vogel, Progress in Semiconductors, Volume 6,
      John Wiley and Sons, Inc., New York, New York, 1962, p. 18.

[36]  J. R. Hauser (private communications).

[37]  Research Triangle Institute, Integrated Silicon Device Technology,
      Vol III----Photoengraving, by J. J. Wortman, Technical Documentary
      Report ASD-TDR-63-316, Vol III, Contract No. AF 33(657)-10340,
      Durham, N. C., January 1964 (U) AD-603 715.

[38]  Research Triangle Institute, Integrated Silicon Device Technology,
      Vol IV----Diffusion, by A. M. Smith, Technical Documentary Report
      No. ASD-TDR-63-316, Vol. IV, Contract No. AF 33(657)-10340, Durham,
      N. C., February 1964 (U) AD-603 716.

[39]  Research Triangle Institute, Integrated Silicon Device Technology,
      Vol VIII----Diodes, by R. M. Burger, Technical Documentary Report
      ASD-TDR-63-316, Vol VIII, Contract No. AF 33(657)-10340, Durham,
      N. C., (to be published).

[40]  W. Rindner, G. Doering, and R. Worson, "Structural and Operational
      Characteristics of Piezotransistors and Applied Devices", Solid
      State Electronics, Pergamon Press, New York, New York, 1965, p. 232.

[41]  W. H. Legat and L. K. Russell, "A Silicon p-n Junction Transducer",
      paper presented at the 1964 Electron Devices Meeting, Washington,
      D. C., October 29, 1964.

[42]. F. G. Allen, "Field Emission from Silicon and Germanium; Field Desorption and Surface Migration", Phys. Chem. Solids 19, April 1961, pp. 87-99.

[43] Harvard University, "Field Emission from Germanium in a Müller Field Emission Microscope", by F. G. Allen, Technical Report No. 237, Cambridge, Massachusetts, December 1955.

[44] I. H. Shames, Engineering Mechanics: Statics and Dynamics, Prentice-Hall Inc., Englewood Cliffs, New Jersey, 1960.

[45] J. J. Wortman and R. A. Evans, "Young's Modulus, Shear Modulus, and Poisson's Ratio in Silicon and Germanium", J. Appl. Phys. 36, January 1965, pp. 153-156.

[46] P. R. Perino, "Sensors and Transducers for Measuring Pressure, Displacement, Force, Acceleration", Machine Design, July 1965, pp. 154-165.

[47] J. C. Hensel and G. Feher, "Cyclotron Resonance Experiments in Uniaxially Stressed Silicon: Valence Band Inverse Mass Parameters and Deformation Potentials", Phys. Rev. 129, February 1963, pp. 1041-1062.

[48] H. Hasegawa, "Theory of Cyclotron Resonance in Strained Silicon Crystals", Phys. Rev. 129, February 1963, pp. 1029-1040.

[49] A. B. Phillips, Transistor Engineering, McGraw-Hill Book Company, Inc., New York, New York, 1962, Chap. 4, p. 83.

[50] Y. Matukura, "Anisotropic Stress Effect of Silicon pn Junctions", Japanese J. Appl. Phys. 3, May 1964, pp. 256-261.

[51] R. W. Keyes, "The Effects of Elastic Deformation on the Electrical Conductivity of Semiconductors", Solid State Physics, Academic Press Inc., New York, New York, 1962, pp. 149-221.

[52] C. Herring and E. Vogt, "Transport and Deformation Potential Theory for Many-Valley Semiconductors with Anisotropic Scattering", Phys. Rev. 101, February 1956, pp. 944-961.

[53] C. S. Smith, "Piezoresistance in Silicon and Germanium", Phys. Rev. 94, April 1964, pp. 42-49.

[54] D. N. Tufte and E. L. Stelzer, "Piezoresistance Properties of Heavily Doped n-Type Silicon," Phys. Rev. 133, March 1964, pp. A1705-A1716.

[55] W. P. Mason and R. N. Thurston, "Use of Piezoresistive Materials in the Measurement of Displacement, Force and Torque", J. Acoust. Soc. An. 29, October 1957, pp. 1096-1101.

[56] M. Pollack, "Piezoresistance in Heavily Doped n-Type Germanium", Phys. Rev. 111, August 1958, pp. 798-802.

[57]  H. Kroemer, "Quasi-Electric and Quasi-Magnetic Fields in Nonuniform
      Semiconductors", RCA Rev. 18, September 1957, pp. 332-342.

[58]  R. A. Graham, O. E. Jones and J. R. Holland, "Electrical Resistivity
      and Stress-Volume Measurements on Shock-Loaded Germanium", (to be
      published).

[59]  J. R. Hauser, "A Study of Interactions in Silicon Multi-Junction
      Devices", Ph.D. Dissertation, Duke University, 1964.